

# Single-Particle Mass Spectrometry and Inertial Imaging with Nanomechanical Systems

Thesis by

Scott Kelber

In Partial Fulfillment of the Requirements

for the degree of

Doctor of Philosophy



CALIFORNIA INSTITUTE OF  
TECHNOLOGY

Pasadena, California

2013

Defended June 12, 2013

© 2013

Scott Kelber

All Rights Reserved

## ACKNOWLEDGEMENTS

The completion of my thesis studies and my training as a research scientist owe much to the teaching and mentorship of a large number of talented and dedicated people. I would first like to thank my thesis advisor, Professor Michael Roukes, whose support and guidance have made possible what I have accomplished. His method of pushing me to achieve and exploring otherwise dark corners of the scientific landscape has proven invaluable not only for my thesis studies, but as a solid foundation for my future research.

I also want to thank Professor Akshay Naik who helped to mold an inexperienced graduate student into a practitioner of the art that is experimental physics. I am honored to count him as a mentor and a friend.

Selim Hanay was my other chief collaborator, teacher, and partner in crime throughout my thesis work. It is a continuing pleasure to work with him on my various projects and I have benefited immensely from his intelligence, patience, and insight.

I also thank Professor John Sader who kindly decided to help an inquiring graduate student learn theoretical physics and technique. I look forward to many future collaborations in which I can continue to learn from his great knowledge and ability.

My thesis work has also involved extensive collaboration with the scientists at CEA/LETI-Minatec in Grenoble, France. All of my experiments used devices made in collaboration with our LETI partners at their foundry-level cleanroom facility. In particular, wish to thank Laurent Duraffourg, Sébastien Hentz, Eric Colinet and Eric Sage for their help, expertise, and critical analysis that helped push our collaboration to successful frontiers. I also wish to thank Hughes Metras who worked behind the scenes to maintain the collaboration and who also taught me how to connect with the industrial and commercial world in which our technology will ultimately apply.

I greatly enjoyed the chance to work alongside and exchange ideas with many of the excellent people (past or present) in the Roukes group including: Ed Meyers, Jessica Artlett, Warren Fon, Caryn Bullard, Derrick Chi, Trevor Fowler, Peter Hung, Rassul Karabalin, Matt Matheny, Paula Popescu, Gustavo Rios, Eran Segev, Xinchang Zhang, Guillermo Villaneuva, Blake Axelrod, Jean-Sébastien Moulet, Junho Suh, Philip Fong, and Murali Ghatsekar. I also want to thank the people whose logistic and administrative effort makes possible our continuing research: Su Naing, Loly Ekmekjian, Mary Sikora, Exie-Marie Leagons and Sandra Durkee.

I also acknowledge Mona Shaghoulis for her help with MALDI mass spectrometry. I wish to thank Professor Jack Beauchamp for his suggestion of LIAD as the final piece of the puzzle. I am also indebted to other members of my thesis committee, Professor Rob Philips and Professor Mike Cross for their time and suggestions. I also thank Professor Jeff Kimble and Scott Curtis for their support during my initial research experience at Caltech.

A great debt is also owed to the many excellent teachers I had in high school and college who helped to shape the person I am today. I will be forever thankful to my parents whose love and support in all my endeavors has helped to turn my dreams into reality.

Finally, I wish to thank my wife, Marija, the bright star of my life. She has shared in my joy, comforted me in my sorrow, and continues to inspire me to better myself and the world.

## ABSTRACT

This thesis work describes the development of a new technology for mass spectrometry using nanoelectromechanical systems (NEMS-MS). Mass spectrometry is a technique used to identify molecules through mass measurement. Nanoelectromechanical systems (NEMS) feature low cost, scalable on-chip compatibility, and are highly sensitive to the mass of accreted species. Using NEMS devices, we perform NEMS-MS where the inertial mass of individual molecules is directly measured. This contrasts with traditional MS techniques utilizing electromagnetic fields to measure the average mass-to-charge ratio of many molecules.

Initially, an ultra-high-vacuum apparatus is constructed to perform NEMS-MS using laser desorption techniques for molecule delivery. An existing technique, matrix assisted laser desorption ionization (MALDI), is implemented without the usual ion optics system in order to permit detection of neutral and ionized particles. This, however, is found to be incompatible with NEMS-MS due to the matrix background.

The MALDI-NEMS-MS system is then used to measure gold nanoparticles that simultaneously act as the matrix and analyte. These experiments are combined with measurements of IgM antibodies using an ESI (electrospray ionization)-NEMS-MS system to demonstrate single-particle nanomechanical mass spectrometry in real time.

Then, the laser desorption-based NEMS-MS system is upgraded to implement laser induced acoustic desorption (LIAD) for particle delivery. LIAD is a matrix-free technique in the mass spectrometry community for desorbing nonvolatile, thermally labile molecules. The LIAD-NEMS-MS system is used for the direct mass measurement of several different types of proteins and protein-complexes with single-protein quantification. Additionally, experimental data is presented that suggests the movement of surface-adsorbed particles along the device surface due to the vibration of the resonant device modes; this remains to be confirmed.

Finally, a new methodology, inertial imaging theory, is presented, which enables measurement of the mass and shape of adsorbed particles on a NEMS device. The shifts induced by particle adsorption in the modal frequencies of a resonant device are used to calculate the spatial moments of mass distribution of individual adsorbates, one-by-one, as they adsorb. It is shown that the ultimate resolution in particle size of this technique is limited only by fundamental noise processes in the device and not wavelength-dependent diffraction effects. Indeed, atomic resolution is possible using existing NEMS devices.

## TABLE OF CONTENTS

Acknowledgements .....	iii
Abstract.....	v
Table of Contents .....	vii
List of Figures.....	x
Nomenclature .....	xiii
<u>Chapter 1: Introduction</u> .....	1
1.1 Mass spectrometry .....	1
1.2 Principles of NEMS mass spectrometry .....	4
1.3 Role of NEMS-MS in the field of mass spectrometry .....	6
1.4 Summary of work.....	11
1.5 Bibliography .....	13
<u>Chapter 2: LD-NEMS-MS System Construction</u> .....	16
2.1 Introduction.....	16
2.2 Vacuum requirements.....	18
2.3 Substrate sample surface density .....	25
2.4 Backside desorption.....	32
2.5 Traditional MALDI unsuitable for LD-NEMS-MS .....	35
2.6 Gold nanoparticles as matrix.....	41
2.7 Conclusion .....	44
2.8 Bibliography .....	46
<u>Chapter 3: Single-Protein Nanomechanical Mass Spectrometry in Real Time</u> .....	48
3.1 Introduction.....	48

3.2 Motivation.....	49
3.3 Experimental Technique .....	52
3.4 Results: gold nanoparticles.....	60
3.5 Results: human IgM antibody measurements.....	67
3.6 Conclusion .....	70
3.7 Bibliography .....	71
<u>Chapter 4: LIAD-NEMS-MS.....</u>	<u>74</u>
4.1 Introduction.....	74
4.2 Motivation for LIAD .....	77
4.3 LIAD theory .....	79
4.4 Engineering the substrate .....	81
4.5 Experimental setup .....	86
4.6 Protein deposition.....	88
4.7 Results: protein desorption.....	90
4.8 Results: protein mass spectrometry.....	92
4.9 Discussion: protein mass spectra .....	107
4.10 Results: protein particle position analysis.....	110
4.11 Conclusion .....	118
4.12 Bibliography .....	121
<u>Chapter 5: Inertial Imaging with Nanomechanical Systems.....</u>	<u>123</u>
5.1 Introduction.....	123
5.2 Superpositions of resonator modes .....	124
5.3 Residual error and adaptive fitting.....	131
5.4 Minimum number of modes.....	139
5.5 Theory validation with experimental data and FEM simulations .....	143

5.6 Ultimate resolution .....	147
5.7 Conclusion .....	149
5.8 Bibliography .....	150
<u>Concluding Remarks</u> .....	151
Appendix: Derivation of Moments for Doubly-Clamped Beam .....	157

## LIST OF FIGURES AND TABLES

<i>Number</i>	<i>Page</i>
1. Chamber assembly .....	19
2. NEMS chip on PCB mount .....	21
3. Frequency fluctuations in different pressure regimes .....	23
4. Image of the MALDI plume .....	27
5. Initial mass depositions on NEMS device.....	28
6. Backside desorption setup .....	31
7. Mass deposition from organic acid matrix plus protein.....	34
8. Position spectra from organic acid matrix plus protein .....	36
9. Position spectra from simulated GNPs.....	38
10. Position spectrum measured from 10nm GNPs .....	41
11. Attempted detection of IgM and Lambda Phage Virus. ....	43
12. Multimode NEMS-based mass detection in real time. ....	53
13. PLL circuit diagram .....	54
14. ESI setup .....	55
15. Diagram of the MALDI experimental system .....	56
16. Joint probability distributions for analyte mass and position-of-adsorption.....	59
17. The evolution of a NEMS-MS spectrum in real time .....	61
18. Error fitting contours for 10nm GNP data .....	62
19. Peak identification.....	63
20. TEM images of 5nm GNPs .....	64
21. The nanomechanical mass spectra for human IgM.....	66

22. Comparison of IgM and 10-nm GNP mass spectra .....	69
23. Composite substrate stack for maximizing a laser-acoustic pulse .....	82
24. UHV compatible LIAD substrate.....	84
25. GNP desorption on engineered LIAD substrate .....	85
26. LIAD-NEMS experimental setup.....	87
27. Electrospray deposition setup .....	89
28. Initial LIAD protein results.....	91
29. Mass spectra of protein complexes with one sub-unit .....	93
30. IgM analysis .....	94
31. Thyroglobulin analysis .....	96
32. Mass spectra of protein complexes with multiple sub-units.....	99
33. Proteasome complex .....	100
Table 1: Peak identification of the proteasome complex.....	101
34. Ribosomes from <i>E. Coli</i> , purified 70s and 50s .....	103
35. Mass spectrum of the RAG complex .....	105
36. Mode square displacements with noise cutoffs.....	108
37. Protein position spectra.....	109
38. Mode superpositions .....	114
39. IgM position spectra from LIAD- and ESI-NEMS setups .....	115
40. Apoferritin position spectra as parameters are varied.....	117
41. Superpositions of fundamental mode shapes .....	127
42. Four-mode superposition functions to calculate the first three moments.....	131
43. Adaptive fitting for enhanced resolution and accuracy .....	135
44. Locating a particle in or out of the measurement zone .....	136
45. Simulated results of a highly skewed particle.....	138

46. Inertial imaging using experimental data .....	143
47. Variance of gold bead density distribution as a function of position .....	145
48. FEM demonstration of inertial imaging .....	146
Table 2: Imaging resolution for typical micro- and nanomechanical resonators.....	148

## NOMENCLATURE

**NEMS.** Nanoelectromechanical system.

**Dalton.** The unified atomic mass unit,  $1/12^{\text{th}}$  the mass of a carbon-12 atom. One Dalton equals  $1.66 \times 10^{-24}$  grams.

**ESI.** Electrospray Ionization.

**MALDI.** Matrix assisted laser desorption ionization.

**LIAD.** Laser induced acoustic desorption.

**LD.** Laser desorption.

**GNPs.** Gold nanoparticles. A.k.a. Gold colloids.

# *Chapter 1*

## INTRODUCTION

This thesis is the development of a new technological platform in the field of mass spectrometry. Mass spectrometry is based on particle identification through mass measurement and is common technique in a variety of fields including structural biology, disease research, clinical pathology, pharmaceutical studies, geology, environmental analysis, and chemical detection, amongst others. I continue the ongoing efforts in the Roukes group to perform mass spectrometry using nanoelectromechanical systems (NEMS). NEMS devices are small mechanical objects where the motion is actuated and detected via transduction between mechanical and electrical signals. These devices operate on the nanometer scale, which means at least one of the device dimensions is less than a micrometer. Manufactured at the chip scale using the technology developed by the semiconductor industry for integrated circuits, NEMS devices are a powerful scientific tool due to their high sensitivity to external perturbations (e.g., mass, force, EM radiation, etc.) and that ability to be manufactured relatively cheaply *en masse*. NEMS-based mass spectrometry (NEMS-MS) has a number of important features especially for proteomic mass spectrometry that motivate our research.

### **1.1 Mass spectrometry**

Mass spectrometry a technique used across a variety of fields to measure the molecular weight of small particles for identification and analysis. Over the last two decades, mass spectrometry has assumed a dominant role in the field of proteomics [1]. While the genomics revolution has

enabled a precise recording of the genes of a biological system, this only predicts the possible proteins the system could produce. The full physiological description of a biological system requires an analysis of the actual proteins themselves. This includes information about proteins that cannot be captured from genomic information such as relative expression levels, post-translational modifications, and dynamic protein-protein interactions and responses to environmental triggers [2, 3]. With the quantitative power of mass spectrometry, proteins can be measured across a huge range of biological systems differing in size and complexity, from single cells to large human populations [4].

The principle of conventional mass spectrometry relies on using electromagnetic fields to separate molecules according to their mass-to-charge ( $m/z$ ) ratios. The molecules are then sent to a charge detector which counts the ions as they arrive. The detector signal is converted into a spectrum of  $m/z$  ratios consisting of various peaks. The centroid of each peak feature in the spectrum corresponds to an average measurement over an ensemble of ions; single-particle measurement is not possible with conventional techniques. Additionally, molecules produce not one peak but multiple peaks representing the different charge states of the species. Deducing the mass value from the several  $m/z$  peak values requires sufficient system resolution to distinguish the different charge states. There are a great many different varieties and permutations of methods for  $m/z$  separation and detection; a complete listing is not given here. Some of the most common techniques for  $m/z$  separation include:

**Time of flight (TOF)** – ions are collected and focused into a beam using a system of ion optics. The beam enters a drift tube where the time of arrival at the charge detector is dependent on the  $m/z$  ratio of the ion.

**Quadrupole (Q-MS)** – the ion beam enters a chamber with four metallic rods to which are applied high-power RF electric fields. These fields trap the ions and can be tuned to selectively eject molecules with a particular  $m/z$  ratio to the detector.

**Fourier Transform Ion Cyclotron Resonance Mass Spectrometry (FTICR-MS)** – the ions circulate between two conducting plates using a constant magnetic field. The orbital radius and frequency of the ions is dependent on their  $m/z$  ratio. Taking the Fourier transform of the voltage signal induced on the plates produces a spectrum with peak features corresponding to the separate  $m/z$  values of the different ions.

**Orbitrap** – is similar to FTICR except the ions orbit without a magnetic field in a hollow cavity defined by two elliptically shaped electrodes, an inner and outer electrode. The frequency of the axial (as opposed to radial) rotation about the inner electrode is dependent the molecular  $m/z$  value. The image current on the outer electrode is then decomposed, as in FTICR, to create a spectrum.

These methods of  $m/z$  separation can be used independently or sometimes in tandem, often in combination with collisional cells where ion collisions with the background gas induce fragmentation. In such systems, large molecules can be measured and then selectively broken down in the collisional cell into their constituent parts that are in turn measured in a later stage of the system. Most of the systems operate in vacuum ( $\sim 10^{-6}$  Torr) conditions. These methods for  $m/z$  separation must be then paired with some form of analyte injection and ionization.

Two of the most common methods for sample injection are mentioned above, ESI and MALDI. In ESI [5], the sample in liquid solution is pumped through a small needle that is charged to a high voltage. The needle expels charged droplets of the solution that enter the vacuum system via a small capillary. The large voltage difference causes the droplets to undergo cycles of evaporation and Coulombic fission until individual particle ions are injected in the gas phase into the  $m/z$  separator.

In contrast with ESI, MALDI operates by preparing a dried sample or probe that is directly inserted into the vacuum apparatus [6], and not injected via a capillary. The MALDI sample consists of a compound, the matrix, that is mixed with the analyte and dried onto a sample plate. There exist a great many varieties of sample preparation techniques and matrix compounds, though usually organic acids or metallic nanoparticles [7] are used. After insertion, the MALDI sample is exposed to laser radiation that is efficiently absorbed by the matrix. The matrix then explodes from the surface, both ionizing the analyte particles and promoting them to the gas phase. This plume of matrix and analyte ions is then collected by a system of ion optics and sent for  $m/z$  separation.

Related to MALDI is a technique, LIAD, that is the basis of the results in chapter four. In LIAD, the purified analytes are deposited onto the sample plate without a matrix. In place of matrix absorption of laser light, the LIAD substrate plate itself absorbs the optical energy and generates an acoustic pulse that ejects the analytes into the gas phase. Without a matrix, ionization is usually achieved using a secondary ionization process, although ambient charging from solution is sufficient in some applications. Since NEMS-MS is an inertial detection method, the ionization pathways are not a focus of this work.

## **1.2 Principles of NEMS mass spectrometry**

The basis for NEMS-MS is the use of small nanomechanical devices to measure particle mass. Unlike conventional spectrometry – where the particles are first separated according to their  $m/z$  ratio in one part of the system and then detected in another – in NEMS-MS, the device simultaneously detects the particles and measures their mass. This is possible because the small size of NEMS devices and the high precision with which their frequency can be measured make them powerful tools in a variety of applications. These include studies of quantum behavior [8-10], nonlinear device physics [11-14], and a great variety of sensing applications including gas sensing,

bio-sensing in liquid, and temperature measurement, amongst others [15-27]. In this work, the high sensitivity of NEMS devices is exploited to measure the mass of accreted particles in a high-vacuum environment.

A detailed mathematical description of single-particle mass measurement using multiple, tracked frequency modes of a device is given elsewhere [22, 28, 29]. In brief, the NEMS resonating device has an inverse relationship between the resonance frequency of an eigenmode and the mass of the device. When a particle lands on the device, the total device mass changes and the frequency will shift downward by an amount dependent on the mass of the particle and the place on the device where the particle lands.

In our experiments, the devices are cooled to liquid nitrogen temperatures (77 K) to promote physisorption; other methods such as vacuum-compatible protein functionalization could be used in the future. By continuously tracking the resonance frequencies of the first two displacement modes of a doubly-clamped beam device, the frequency shifts due to particle landing events are recorded in real time and then used to calculate the mass and position of the adsorbates. This formalism is used in chapters two, three, and four for point-like particles (relative to the device size). Chapter five presents a new formalism for particles with finite size (relative to the device), where it is shown that particle shape, in addition to mass and landing position, can be calculated.

NEM-MS is thus an inertial-based sensing technique where, in contrast with conventional mass spectrometry, particle ionization is not required. The ability to measure neutral and ionized particles expands the parameters of possible protein delivery techniques to include those that succeed in transporting analytes to the detector, regardless of the presence or absence of ionization pathways.

An important consideration of our NEMS-MS technique is that accurate results are not obtained if more than one particle lands on the device during a measurement window – the minimum time required to record a change in the resonance frequency. This window is based on the nature of

the methodology used to for frequency tracking. In our work, for example, a phase-locked loop (PLL) is employed that features a measurement window of 100 ms. New, next generation electronic systems in the process of deployment can reduce this to ten microseconds. For most of the presented experiments, multiple landing events was not a problem as the struggle was to get any events landing on the device. However, in general, the device measurement window bounds the maximum particle flux rate for a single device.

### **1.3 Role of NEMS-MS in the field of mass spectrometry**

NEMS-MS features some important advantages for mass spectrometry, the foremost of which is single molecule detection. While charge detectors capable of recording a signal due to a single ion exist, current techniques are unable to provide quantification of all signals at the level of single molecules. Single-molecule mass measurement allows for systems that can provide robust results for small samples and precise quantification across a variety of samples.

Second, as mentioned previously, NEMS-MS is capable of neutral detection. This makes NEMS-MS well-suited for applications in a growing subset of mass spectrometry known as “native” mass spectrometry. Native mass spectrometry seeks to measure large protein complexes in their original or native state, unaltered by charge-induced deformation or fragmentation [30-34]. Currently, native-MS is reliant on conventional mass spectrometry techniques that require some minimal amount of charging for measurements, which is not ideal. In contrast, a NEMS-MS system with an ionization-free sample preparation methodology would thus be well suited for measuring large protein structures in their native configuration, unaltered from their state in solution. The sample preparation method for the LIAD-NEMS-MS system presented in chapter four may alter the native state of proteins due to surface attachment and desorption effects, but this is not inherent to NEMS-MS in general.

Third, NEMS-MS is well-suited for the measurement of high mass species (>200 kDa) compared to conventional techniques (though impressive technological strides are ongoing [35]). The precise mass dynamic range varies with the type of system, but conventional proteomic mass spectrometry can generally measure bio-molecules with masses ranging from tens of Daltons to a few hundred kilo-Daltons. Analytes in the mega-Dalton range or above are generally at or beyond the limit of most conventional systems. This is because, conventionally, the mass resolution (defined as the peak width in the  $m/z$  spectrum) degrades with increasing mass. Larger ions are more difficult to charge (per unit mass), resulting in an increased spread in their kinetic energies and a thus an increased peak width. After a certain point, the system is unable to measure the mass of these molecules, either because they are not transported to the detector or because the resolution is so poor that the various charge states overlap and the mass value cannot be extracted from the  $m/z$  peaks.

The mass resolution of NEMS-MS, however, is independent of the particle mass and is determined by the frequency-noise processes inherent to the device itself. The effective mass resolution our current devices, 50 kDa, is quite poor compared to conventional standards that can achieve sub-Dalton resolution for small particles (less than a kilo-Dalton). However, because the mass resolution of a NEMS device is fixed across the mass range, particles weighing a mega-Dalton or more can be measured with high resolution compared to conventional techniques that either cannot measure the mass of particles in that range or do so with only poor resolution. Indeed, the upper limit to particle size in a NEMS-MS system is roughly 10% of the device mass (this limit is ~30GDa for current devices). Beyond this point, a single particle event will degrade the device performance so as to significantly alter the measurement. This mass dynamic range of current NEMS-MS, 50 kDa to 30 GDa, provides NEMS-MS with a niche role for the measurement of large bio-molecules that are inaccessible with standard techniques. As new NEMS devices are developed with improved

resolution, the lower mass limit can be extended down in to the range of peptides (hundreds of Daltons) or amino acids (tens of Daltons).

Fourth, NEMS-MS are more scalable than conventional mass spectrometers. All the NEMS-MS components used in the present work can be integrated using very large scale integration (VLSI) techniques. This allows for massively parallel systems utilizing present semiconductor manufacturing technology. In this context, chips with thousands of devices could be manufactured relatively cheaply and deployed for high-throughput systems. There remain significant challenges in this regard as we are only now beginning to experiment with modest arrays of up to 100 interconnected devices – far from the chips of hundreds of thousands of devices envisaged in the future. This chip-based architecture (combined with a lack of a need for ion optics) is also advantageous for miniaturized mass spectrometry systems that are ideal for end-use clinical settings, field-deployable operations in security screening, and incorporation into space probes for astrobiology chemical analysis and the search for organic matter, amongst others.

There is indeed a range of applications for which NEMS-MS is ideally suited. In the near term, it may be imagined to use NEMS-MS for such application as highly quantitative proteomics for disease diagnosis or biomarker detection. One could also perform experiments for the structural analysis of large protein complexes. This may include investigation, for example, of viral capsid assembly, or the behavior of cellular machines such as the proteasome whose dynamics are largely determined by their structure. Additionally, bacterial biotyping at the single-cell level could be performed where the proteomic fingerprint of a single cell is measured and compared to a fingerprint library of bacterial species. Biotyping at the single-cell level could also reveal variations within nominally the same species due to random mutations or post-translational modifications.

Farther in the future, as arrays of thousands of devices are deployed with mass resolutions near the single-Dalton level, very ambitious experiments may be initiated, such as the mapping of the

entire proteome of a single cell. The concentration dynamic range of a human cell is  $10^{11}$ ; the most common protein has a concentration  $10^{11}$  times that of the least common protein. A system for measuring all the proteins in a single mammalian cell must therefore be capable of distinguishing a single protein out of  $10^{11}$  other proteins in the sample. A NEMS-MS system featuring 100,000 devices operating in parallel, with each device able to measure a single protein every millisecond, could thus map out the proteome of a single cell in approximately twenty minutes. Such performance benchmarks are feasible in the not-too-distant future, considering NEMS fabrication utilizes similar techniques as are regularly used to manufacture integrated computer circuits with billions of devices per chip operating at sub-microsecond speeds.

Another future application of NEMS-MS is as a tool in imaging mass spectrometry (IMS). IMS is an increasingly popular technique in which mass spectrometry is sequentially performed on a subdivided grid of a two-dimensional tissue section to produce a spatial-chemical map of the sample (through the analysis of thin stacks of a tissue sample, a three-dimensional map can be constructed). This is useful for a variety of applications including cancer research, drug discovery and metabolomics, and monitoring dynamic biological processes [36]. With its large mass dynamic range for measurement and single-molecule sensitivity, NEMS-MS could be a powerful tool for advancing IMS in such areas as sub-cellular imaging below the optical diffraction limit. Also, deploying high density, macroscopic NEMS arrays, one may imagine performing IMS where a single, macroscopic tissue sample is imaged at once (without raster scanning as is currently done) but high spatial resolution (potentially sub-micron) is retained.

The above applications are meant to provide a flavor for the types of biological investigations that will be made possible or enhanced through the use of NEMS-MS. However, there are still important technological challenges to be overcome.

One of the main current limitations of NEMS-MS is the mass resolution. This is a continually improving parameter as new and better device designs are incorporated into the system. Our current devices have a mass resolution of 50 kDa, but carbon nanotube devices have reported mass resolutions at the yoctogram level [25]. These nanotube results demonstrate that there are no fundamental physical barriers to improving mass resolution down to the single Dalton level. However, nanotube devices are not compatible with CMOS electronics and VLSI, both of which are necessary for the operation of NEMS arrays. There are two ways to improve the mass resolution of our devices, minimize the noise processes, and fabricate smaller devices. Both must be done while maintaining CMOS and VLSI compatibility; such is a topic of ongoing research. The estimated mass resolution of our devices due to thermomechanical noise [15] is significantly lower than what is currently measured, indicating that there is some room to improve the mass resolution without shrinking the devices.

Additionally, the ultimate throughput of a NEMS-MS system is, in part, limited by the capture cross-section of the NEMS array. In a NEMS-MS system, the particle plume or beam is sprayed onto a chip, a fraction of which is captured by the devices. This fraction is determined by the sensing area of the chip, relative to the total plume size. Because the devices require clamping structures and electronic signal pathways, there is a limit to the density of NEMS arrays. The filling factor, or ratio of the sensitive area relative to the total area of a pixel, is less than one percent for first generation arrays. Future plans involving three dimensional device integration with CMOS electronics and new device geometries (thin membranes) suggest that a filling factor of up to 10% can be achieved. This number compares favorably with commonly reported estimates for the overall efficiency of ESI and MALDI systems of 5-10% [3]. The theoretical limit of efficiency for an ESI-MS system of 85% has been demonstrated on a specialized system [3]. A filling factor of 10% means

that of the total sample sprayed at the NEMS chip, 10% will be measured. The overall throughput could be further improved in the future, however, through novel device designs and chip stacking.

Finally, NEMS-MS has an operational limitation in that the NEMS devices eventually become mass loaded to a degree where device performance is comprised. Particles are measured sequentially. As long as the device is not degraded, previous particles accumulating on the surface do not affect subsequent measurements. For current devices and proteins of interest, several thousand protein events are required to compromise device performance. Once this occurs, the devices are easily cleaned by heating in vacuum and are quickly restored to their original state. Though not a limitation in current experiments, repeated heating and cooling device cycles may become a limiting factor in future, high-throughput systems.

In summary, NEMS-MS has powerful potential in the field of mass-spectrometry. As either a stand-alone system or in tandem with conventional techniques, we anticipate NEMS-MS will eventually arise as an important tool across the many fields that utilize mass spectrometry.

## **1.4 Summary of work**

My thesis work consists of the construction and operation of a novel system to perform NEMS-based mass spectrometry of single particles and proteins. Additionally, this thesis also presents a new methodology to use NEMS-based systems not only for mass measurement of single particles, but imaging as well. NEMS-MS systems can be divided into two components: a mechanism for delivering the proteins from a sample to a detector, and a detector capable of measuring the mass of the proteins.

The protein delivery techniques utilized in this work, MALDI, ESI, and LIAD, are adaptations of existing methodologies from the field of mass spectrometry. The detector for measuring the mass of the proteins consists of a single NEMS device. Our devices were manufactured

in collaboration with our partners at CEA/LETI-Minatec in Grenoble, France, using their foundry-level cleanroom facility.

My thesis continues the ongoing work in the Roukes group to combine NEMS devices with protein delivery techniques to perform single-particle mass spectrometry. Previous NEMS-MS systems in the Roukes group utilized ESI to deliver proteins to the NEMS detector [22]. The goal of my new system was to improve on current NEMS-MS by: a) increasing the particle detection rate compared to these previous incarnations and, b) removing the need for ion optics to create a system capable of performing neutral mass spectrometry. As is discussed in detail in the following chapters, increasing the particle detection rate is important for further system development, as well as producing prototype systems useful to the wider mass spectrometry community. Additionally, the ability to perform neutral mass spectrometry has important implications for the study of large protein complexes that are discussed below.

Chapter two describes the important steps involved in the construction of the experimental apparatus. This new system combines laser desorption (LD) techniques for proteins with NEMS-MS. The principal LD technique used in chapter two is MALDI, described above. Chapter two is organized around several critical parameters for a LD-NEMS-MS system that are meant not only as a catalogue of my work, but also as a guide to the future construction of similar systems. It was found that though the LD-NEMS-MS system is capable of single-particle detection, a different protein delivery technique besides MALDI is required for protein analysis.

Chapter three presents the initial results of the system described in chapter two to measure gold nanoparticles (GNPs) using MALDI. These results serve to validate multimode theory for mass and position measurement [28] and the LD-NEMS-MS experimental system as a means of measuring single-particles. Chapter three also describes the first demonstration of single-protein nanomechanical mass spectrometry in real-time using the ESI-NEMS-MS system I helped to rebuild

and operate for these successful measurements. This work is based on the experimental work described in [29].

Single-protein mass spectrometry is finally performed in the LD-NEMS-MS system through the use of a different LD technique known as laser induced acoustic desorption ionization (LIAD). These results are the topic of chapter four in which the mass spectra of various proteins and protein complexes obtained using LIAD-NEMS-MS are presented. Chapter four also discusses interesting but as yet inconclusive experimental results, suggesting that the beam motion may alter the measured position (but not the mass) of the particles after adsorption.

Chapter five presents novel theoretical work showing that NEMS devices can be used to simultaneously measure the mass, position, and shape of individual adsorbates. The frequency shifts induced in the multiple modes of a resonator device can be used to calculate the spatial moments of mass distribution of individual adsorbates. This information amounts to an inertial image of the particle. The methodology is validated with a re-analysis of experimental data and finite element modeling (FEM) simulations. The ultimate resolution of this technique – the smallest measurable particles – is not limited by the modal wavelength, but only by the frequency noise processes of the resonator. Using currently available NEMS devices, atomic-scale imaging and mass spectrometry are possible.

Finally, this thesis concludes with a summary of results and an outlook for future experiments.

## 1.5 Bibliography

1. Domon, B. and R. Aebersold, *Review - Mass spectrometry and protein analysis*. Science, 2006. **312**(5771): p. 212-217.
2. El-Aneed, A., A. Cohen, and J. Banoub, *Mass Spectrometry, Review of the Basics: Electrospray, MALDI, and Commonly Used Mass Analyzers*. Applied Spectroscopy Reviews, 2009. **44**(3): p. 210-230.

3. Cole, R.B., *Electrospray and MALDI mass spectrometry: fundamentals, instrumentation, practicalities, and biological applications*. 2011: Wiley.
4. Bantscheff, M., et al., *Quantitative mass spectrometry in proteomics: critical review update from 2007 to the present*. Analytical and bioanalytical chemistry, 2012. **404**(4): p. 939-965.
5. Fenn, J.B., et al., *Electrospray Ionization for Mass-Spectrometry of Large Biomolecules*. Science, 1989. **246**(4926): p. 64-71.
6. Karas, M., D. Bachmann, and F. Hillenkamp, *Influence of the Wavelength in High-Irradiance Ultraviolet-Laser Desorption Mass-Spectrometry of Organic-Molecules*. Analytical Chemistry, 1985. **57**(14): p. 2935-2939.
7. Tanaka, K., *The Origin of Macromolecule Ionization by Laser Irradiation (Nobel Lecture)*. Angewandte Chemie International Edition, 2003. **42**(33): p. 3860-3870.
8. Naik, A., et al., *Cooling a nanomechanical resonator with quantum back-action*. Nature, 2006. **443**(7108): p. 193-6.
9. O'Connell, A.D., et al., *Quantum ground state and single-phonon control of a mechanical resonator*. Nature, 2010. **464**(7289): p. 697-703.
10. Suh, J., et al., *Parametric Amplification and Back-Action Noise Squeezing by a Qubit-Coupled Nanoresonator*. Nano Letters, 2010. **10**(10): p. 3990-3994.
11. Lifshitz, R. and M. Cross, *Nonlinear dynamics of nanomechanical and micromechanical resonators*. Reviews of nonlinear dynamics and complexity, 2008. **1**: p. 1-48.
12. Villanueva, L.G., et al., *A nanoscale parametric feedback oscillator*. Nano Lett, 2011. **11**(11): p. 5054-9.
13. Karabalin, R.B., et al., *Signal amplification by sensitive control of bifurcation topology*. Phys Rev Lett, 2011. **106**(9): p. 094102.
14. Kenig, E., et al., *Optimal operating points of oscillators using nonlinear resonators*. Phys Rev E Stat Nonlin Soft Matter Phys, 2012. **86**(5 Pt 2): p. 056207.
15. Ekin, K.L., X.M.H. Huang, and M.L. Roukes, *Ultrasensitive nanoelectromechanical mass detection*. Applied Physics Letters, 2004. **84**(22): p. 4469-4471.
16. Ilic, B., et al., *Attogram detection using nanoelectromechanical oscillators*. Journal of Applied Physics, 2004. **95**(7): p. 3694-3703.
17. Yang, Y.T., et al., *Zeptogram-scale nanomechanical mass sensing*. Nano Lett, 2006. **6**(4): p. 583-6.
18. Li, M., H.X. Tang, and M.L. Roukes, *Ultra-sensitive NEMS-based cantilevers for sensing, scanned probe and very high-frequency applications*. Nature Nanotechnology, 2007. **2**(2): p. 114-120.
19. Chiu, H.Y., et al., *Atomic-Scale Mass Sensing Using Carbon Nanotube Resonators*. Nano Letters, 2008. **8**(12): p. 4342-4346.
20. Lassagne, B., et al., *Ultrasensitive Mass Sensing with a Nanotube Electromechanical Resonator*. Nano Letters, 2008. **8**(11): p. 3735-3738.
21. Jensen, K., K. Kim, and A. Zettl, *An atomic-resolution nanomechanical mass sensor*. Nat Nanotechnol, 2008. **3**(9): p. 533-7.
22. Naik, A.K., et al., *Towards single-molecule nanomechanical mass spectrometry*. Nature Nanotechnology, 2009. **4**(7): p. 445-450.
23. Gil-Santos, E., et al., *Nanomechanical mass sensing and stiffness spectrometry based on two-dimensional vibrations of resonant nanowires*. Nat Nanotechnol, 2010. **5**(9): p. 641-5.
24. Burg, T.P., et al., *Weighing of biomolecules, single cells and single nanoparticles in fluid*. Nature, 2007. **446**(7139): p. 1066-1069.
25. Chaste, J., et al., *A nanomechanical mass sensor with yoctogram resolution*. Nature Nanotechnology, 2012. **7**(5): p. 300-303.

26. Schmid, S., et al., *Real-time single airborne nanoparticle detection with nanomechanical resonant filter-fiber*. Sci Rep, 2013. **3**: p. 1288.
27. Dohn, S., et al., *Enhanced functionality of cantilever based mass sensors using higher modes*. Applied Physics Letters, 2005. **86**(23).
28. Hanay, M.S., *Towards Single-Molecule Nanomechanical Mass Spectrometry*, in *Physics*. 2011, California Institute of Technology.
29. Hanay, M.S., et al., *Single-protein nanomechanical mass spectrometry in real time*. Nature Nanotechnology, 2012. **7**(9): p. 602-608.
30. Benesch, J.L. and C.V. Robinson, *Mass spectrometry of macromolecular assemblies: preservation and dissociation*. Curr Opin Struct Biol, 2006. **16**(2): p. 245-51.
31. Heck, A.J.R., *Native mass spectrometry: a bridge between interactomics and structural biology*. Nature Methods, 2008. **5**(11): p. 927-933.
32. Kaddis, C.S., et al., *Sizing large proteins and protein complexes by electrospray ionization mass spectrometry and ion mobility*. Journal of the American Society for Mass Spectrometry, 2007. **18**(7): p. 1206-1216.
33. Uetrecht, C., et al., *Ion mobility mass spectrometry of proteins and protein assemblies*. Chem Soc Rev, 2010. **39**(5): p. 1633-55.
34. Uetrecht, C., et al., *Interrogating viral capsid assembly with ion mobility-mass spectrometry*. Nat Chem, 2011. **3**(2): p. 126-32.
35. Rose, R.J., et al., *High-sensitivity Orbitrap mass analysis of intact macromolecular assemblies*. Nat Methods, 2012. **9**(11): p. 1084-6.
36. Rubakhin, S.S. and J.V. Sweedler, *Mass Spectrometry Imaging: Principles and Protocols*. 2010: Humana.

## *Chapter 2*

# CONSTRUCTION OF UHV SYSTEM FOR LD- NEMS-MS

### **2.1 Introduction**

In this chapter I detail the steps involved in constructing an apparatus for NEMS-based mass spectrometry using laser desorption techniques for protein delivery (LD-NEMS-MS). The chapter is organized around several different characteristics for a LD-NEMS-MS system. These are: proper vacuum regime, necessary sample surface density, desorption orientation, and suitability of laser desorption using organic acids or gold nanoparticles. These parameters represent critical aspects of the system design and are meant, in part, to act as a guide for the construction of future systems.

The construction and, later, successful operation of the LD-NEMS-MS system forms the core of my thesis work. The construction phase, and the experimental results presented in chapter three, were overseen by Prof. Akshay Naik (Indian Institute of Science, Bangalore, India), who collaborated in system design and troubleshooting while a research engineer in the Roukes group.

The primary motivation for the construction of a LD-NEMS-MS system, initially, was to increase the overall flux rate on the NEMS device compared to previous implementations of NEMS-MS. In the previous ESI-based NEMS-MS system in the Roukes group, the data event rate was maximized at ~1-2 events/minute [1]. The main flux-limiting factor was the requirement that the protein source, which was an ESI injector, had to be physically removed from the detector to allow

for differential pumping. Therefore, a stream of protein molecules had to be efficiently transported over a great distance ( $\sim 1\text{m}$ ) to a nanometer-scale target. It was believed that a laser desorption-based system – in which a dense protein plume can be placed close to the NEMS detector within the same vacuum chamber – would significantly improve the data collection rate.

In chapter three and four it is shown that the LD-NEMS-MS system attained data event rates of one event/second, validating this belief. Compared to conventional MS systems, however, this is still a relatively low data collection rate. It must be remembered that these first-generation NEMS-MS systems are proof-of-concept systems using only a single NEMS device for detection. An actual NEMS-MS system deployable for mass spectrometry end-users would feature thousands of on-chip devices operating in parallel. Nonetheless, continued advancement of NEMS-MS technology, even at this proof-of-concept level, necessitated an increase in the flux rate and was thus an original motivating factor for the development of a LD-NEMS-MS system. The previous low flux rates hampered continued experimentation and system development. Additionally, enhancing the flux rate is a critical step towards constructing NEMS-MS system of utility to the wider scientific community.

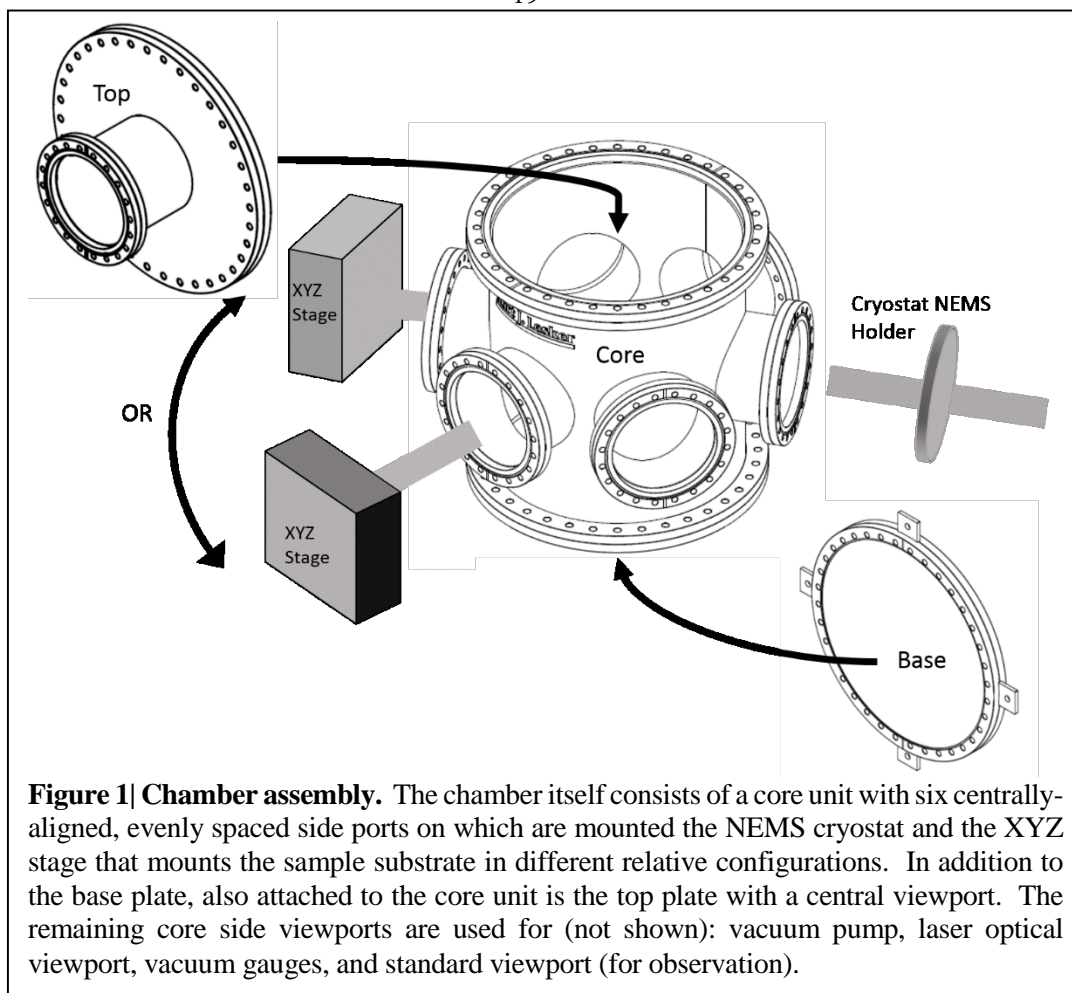
During the course of chamber construction and continual literature review, it was discovered that there is a growing interest in the field of mass spectrometry for so-called “native” mass spectrometry [2, 3], which seeks to minimize the charge state of individual proteins in order to better maintain the original or “native” conformation. Conventionally, LD mass spectrometry techniques, such as MALDI, are used like ESI as a source of analyte particles that are captured by a system of ion optics for delivery to the detector. In ESI the proteins are ionized, but their kinetic energy is determined by the differential pumping and ion optics systems. In MALDI, however, ionization and impartation of kinetic energy to the analytes occur simultaneously at the same source location. This feature of MALDI can be exploited by a neutral detector such as a NEMS device to remove the need for ion optics. ESI-NEMS-MS still requires ion optics for transport.

It should be noted that, regardless of whether ion optics are used, the MALDI process still creates ionized particles. The ionization efficiency, however, is generally less than 10% and usually the ions are only singly charged [4]. Combining MALDI or a similar LD protein delivery technique with NEMS-MS then presents an opportunity to create a system in which neutral particles are the dominant, if not only, type measured.

Thus, an LD-NEMS-MS system allows for two important advantages: an increase in the data collection rate and a system capable of performing neutral mass spectrometry. Before these advantages could be realized, however, the system had to be constructed and particles deposited on the device.

## **2.2 Vacuum requirements**

It is known that NEMS devices become damped in ambient conditions due to collisions with molecules of the surrounding gas [5]. For nanoscale devices, this dissipation becomes negligible in the molecular flow regime (in which the mean free path is much larger than the device area), at pressures usually less than a few mTorr [5]. Most MALDI-MS systems, however, typically operate at lower pressures –  $10^{-5}$  to  $10^{-7}$  Torr – in order to maintain fidelity of the protein ion beam [4]. Thus, it was determined that the LD-NEMS-MS chamber should be capable of at least high vacuum operation ( $10^{-5}$  to  $10^{-9}$  Torr), where the gas molecules collide mainly with the chamber walls and the interior remains relatively free of molecule-molecule interactions. Since this was a novel experimental system, it was further decided that the chamber should be capable of the full vacuum range, including ultra-high vacuum (UHV) ( $<10^{-9}$  Torr). A particular concern was that cooling the



device, which is done to promote physisorption of the analytes, would lead to large mass depositions of ambient gases even in the high vacuum regime<sup>1</sup>.

These two considerations, UHV capability and large interior volume, led to the chamber design displayed in Figure 1. The chamber consists of a core unit with centrally-aligned and evenly-spaced side ports, a bottom plate, and a top plate with a central viewport (Kurt J. Lesker). The core unit (Figure 1) is 20" high with an inner diameter (ID) of 14". The six side flanges are 8" flanges

<sup>1</sup> Additionally, while the goal of the system was to measure proteins directly from the laser-generated plume, it was not known if this would be successful and if ion optics might yet be required. Anticipation of this led to the design of a large experimental system in which the interior volume could well accommodate a system of ion optics or other mechanisms and was easily accessible to the operator. Future LD-NEMS-MS systems could be much more compact than what is presented here.

with 6" ID and are 3" long (from core inner diameter). The bottom plate is a standard 16.5" flange with mounting tabs. The top plate is a nipple reducer from a 16.5" flange to an 8" flange, with a tube ID of 6" and 6.67" of length (from bottom of large flange to top of small flange). All flanges and fittings are standard conflat (CF) flanges designed for use with copper gaskets to allow for UHV compatibility of the entire system.

To provide the capability of moving the sample with respect to the NEMS device, an XYZ stage was installed. Such stages consist of micrometers (one for each Cartesian coordinate), flanges, and bellows that, combined, enable in-vacuum sample movement with external control. The XYZ stage in the present system consists of an XY multibase system (Kurt Lesker) with  $\pm 22$ mm of travel in the X and Y directions. Attached to the system is a linear shift (Kurt Lesker) for Z movement with 150mm of travel. The Z movement is meant to position the substrate sample at a distance from the NEMS detector, while X and Y are dynamically moved during an experiment using motorized controls. For the initial series of experiments, the XYZ stage was not installed. In those experiments, the sample and the NEMS device were held at fixed positions relative to each other and the laser spot was scanned across the substrate sample (described in more detail below).

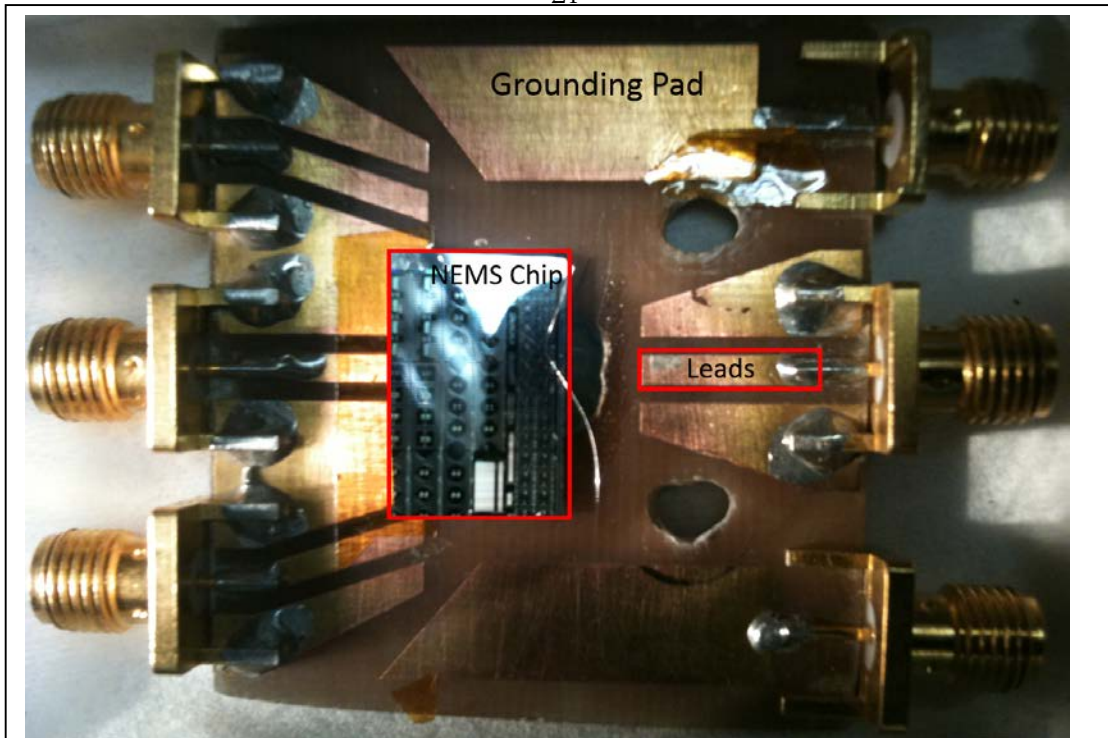


**Figure 2| NEMS chip on PCB mount.** A diced silicon chip on which is fabricated the NEMS device is attached to the PCB chip holder using vacuum-compatible silver paint or copper tape. The on-chip device leads are wirebonded to the lithographically defined PCB leads onto which SMA connectors have been soldered. The PCB leads and grounding pads are copper.

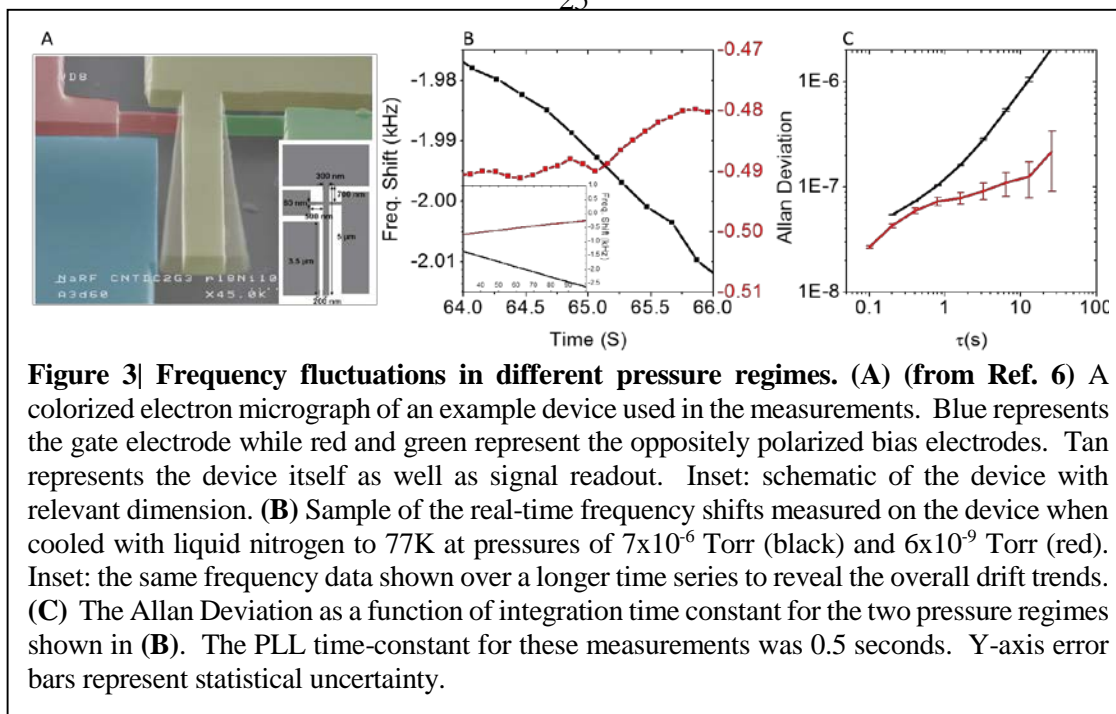
The system was pumped using a roughing scroll pump and a turbomolecular pump (models SH-110 and T-V301, Varian). The roughing pump connected through the turbomolecular pump and was used both initially to pump the chamber from ambient pressure to low vacuum (760 Torr to 50mTorr), and to back out the turbomolecular pump. The turbomolecular pump was activated once a chamber pressure of 50mTorr had been reached and could maintain pressures as low as  $10^{-10}$  Torr. Usual operating pressure during experiments was  $2-7 \times 10^{-9}$  Torr.

The laser beam entered the system through a custom-fabricated optical viewport attached to an 8" CF flange (Kurt Lesker). The glass was HPFS® Fused Silica Standard Grade (Corning) that was AR coated for 337nm. Total transmittance at 337nm was measured to be >98%, consistent with manufacturer specifications.

The holder for the NEMS device consisted of a cryostat (Janis) mounted on an 8" CF flange, with a length of 10" from flange surface to rod end. A custom-machined copper adaptor was mounted at the end of the cryostat rod to allow for the attachment of the printed circuit board (PCB). The PCB was made from standard copper-insulator-copper material. Optical lithography and copper etchant were used on the top side to fabricate the circuit leads. The NEMS chip was positioned at the center of the PCB using either conductive silver paint or copper tape, both vacuum compatible. The circuit leads on the PCB were terminated with soldered SMA heads. After adhering the NEMS chip to the surface, the device was wirebonded to the PCB leads. An example of this arrangement is shown in Figure 2. The SMA heads were attached to semi-rigid stainless steel coaxial cables connected to SMA vacuum electrical feedthroughs mounted on the cryostat flange. These were then connected to the external electronics for running the device. A full description of the circuit and electronic equipment used to operate the devices is given in chapter three.

To determine the appropriate pressure regime for NEMS-MS, cantilever devices manufactured in collaboration with our LETI collaborators were employed, as described in [6]. A colorized electron micrograph of an example device is shown in Figure 3a. The gate electrode (blue) was driven at  $V_{ac}+V_{DC} = -10 \text{ dBm (rms)} + 1 \text{ V (DC)}$ . The two bias electrodes (red, green) were driven at  $\pm 4 \text{ dBm (rms)}$ , respectively. Only the first device mode was actuated for these cantilever devices. The actuation and measurement circuit for these cantilever devices was otherwise the same as one mode of the two-mode actuation and measurement circuit for doubly-clamped beam devices described in chapter three.

The resonance frequency of the first mode of these cantilever devices was monitored in real time using the same phase-locked loop (PLL) architecture described in chapter three. Here, the down-mixed signal offset was 20 kHz and the PLL time constant was 0.5 seconds. Representative temporal frequency data is shown in Figure 3b for the device cooled with liquid nitrogen to 77K. At a chamber



pressure of  $6 \times 10^{-6}$  Torr (Figure 3b, black) the device experiences significant downward frequency drift due to adsorption of ambient gas species (assumed to be primarily water vapor). The average drift rate using the complete data set (Figure 3b, inset) was  $-80$  Hz / second. We characterize the device frequency noise using the Allan Deviation [7], a statistical average (different from the standard deviation) of the frequency fluctuations. The Allan Deviation at this pressure is shown in Figure 3c, and was  $7.4 \times 10^{-8}$  at the PLL time constant of 0.5 seconds. Assuming the source of the drift rate seen in Figure 3b was water vapor adsorption, at the chamber pressure of  $6 \times 10^{-6}$  the drift rate should have been  $-690$  Hz / second based on ideal gas behavior in vacuum, almost an order of magnitude larger than what is measured.

This difference between observed and theoretical values may be possibly due to saturation of available surface sites and/or a surface sticking coefficient much less than unity. Nonetheless, the source of this drift rate was confirmed to be due to background gas adsorption because the negative drift disappeared as the chamber was further pumped down to  $6 \times 10^{-9}$  Torr. The frequency response of the device at this pressure regime is shown in red in Figures 3b and 3c. At this lower pressure,

$6 \times 10^{-9}$  Torr, the expected drift rate due to nitrogen adsorption is  $-0.7$  Hz/s, while the measured drift rate was actually  $+6.8$  Hz/s. This upward drift may have been due to incomplete device thermalization at the time of the measurement. Subsequent measurement of this device after complete thermalization had been attained at this pressure continued to show an absence of the strong negative drift rate seen at the higher pressure regime. Additionally, the Allan Deviation at the PLL time constant improved to  $6 \times 10^{-8}$  (from  $7.4 \times 10^{-8}$ ).

These Allan Deviations,  $\sigma_a$ , correspond to a mass resolution of  $\delta m = 2M_{eff} \sigma_a$  equal to 19 and 15 kDa, respectively, for the high and low pressure regimes ( $M_{eff}$  is the effective mode mass of the device). Thus, considering that the particles to be studied would be greater than 200 kDa, this analysis would suggest that UHV is not required and that a pressure of a few times  $10^{-6}$  Torr would be sufficient for NEMS-MS. Indeed, the ESI-based measurements described in chapter three operated in such a pressure regime. In the future, a LD-NEMS-MS system could also be operated in this regime.

It was decided, however, to operate in the lower pressure regime of a few times  $10^{-9}$  Torr for several reasons. First, device freeze-out (where water vapor solidifies on the device surface and damps the motion) was a concern when cooling the device to 77K while operating at higher pressures. Indeed, this would prove prescient as this limited the operational device temperature in the ESI-IgM experiment (see chapter three) to 140k. Moreover, since it was desirable for the system to be capable of operating at device temperatures down to liquid helium (4K) – in order to try to minimize frequency noise – the low pressure regime was seen as necessary. It should be noted that later operation of the devices at liquid helium temperatures was unsuccessful (even for pressures  $< 10^{-8}$  Torr), for reasons still under investigation.

A second motivation for operating in the UHV regime was due to the method of data analysis. The raw temporal frequency fluctuations were input to a frequency-jump-detection based algorithm

that selected jumps based on the derivative of the temporal frequency signal. Initially, the main difficulty was registering any device response at all due to laser-ablated analytes. In this context, removing the drift was necessary to permit careful data analysis of signals with very small signal-to-noise ratios – even if the difference in Allan Deviations between the two pressure regimes was only ~20%.

Finally, while the analyte-induced frequency jumps may technically be detectable at  $10^{-6}$  Torr, the drift rate was significant enough to alter the measured mass during one PLL cycle. Since one of the goals of the project was to push the sensitivity limit for the devices, eliminating this background experimentally by going to lower chamber pressure was seen as the most desirable course.

Thus, in sum, while operation at  $10^{-6}$  Torr is technically possible for a LD-NEMS-MS system – especially considering next generation electronics that can enable PLL time constants down to  $10\mu\text{s}$  – experimentally eliminating a significant background source enabled easier testing and verification of this first proof-of-concept system, and allowed for minimization of experimental noise. Additionally, in the future the system will be used for a variety of NEMS particle sensing experiments such as mass spectrometry imaging [8-10] or inertial imaging (the latter is a novel methodology discussed in chapter five), that may require even stricter pressure tolerances.

### **2.3 Substrate sample surface density**

Initial experiments to detect mass deposition on the NEMS device in the LD-NEMS-MS system were unsuccessful because the particle flux was too low. A variety of materials and system configurations were tried in order to at least see some frequency change on the device, even if single particles could not be identified. These included sample depositions of thermally evaporated gold and silver nitrate from solution (both absorbers of UV radiation), and applying high voltages to the

conducting sample substrate to increase ion momentum towards the NEMS device. These unsuccessful initial attempts necessitate more careful considerations of the particle plume produced in the MALDI process.

The analyte plume generated following laser adsorption in MALDI has not been heavily studied. In most conventional systems, this plume is a source for ion optics that create and direct a beam of particle ions toward the charge detector. Thus, so long as the process succeeded in providing an initial source of protein ions, only the overall ionization efficiency became a highly studied aspect of the MALDI process [11-14], not the shape or density of the plume itself. One study did, however, image the vapor plume produced during the MALDI process using a secondary fluorescence laser and particle tagging [15]. Results of this study are partially reproduced in Figure 4 as they prove highly instructive for the present endeavor of obtaining sufficient mass flux on the NEMS device. In the following, the expected MALDI plume is modeled and used as a guide for sample preparation and configuration of the experimental system.

As seen in Figure 4, there are two plumes produced when the laser strikes the MALDI sample plate. The first (top row) is a plume of matrix material that expands rapidly in both the axial ( $z$ ) and radial ( $r$ ) directions. The second plume consists of the protein material that is sharply focused and expands in the  $z$ -direction, but experiences relatively little expansion in the  $r$ -direction. According to the authors, this is because the lighter matrix particles experience relatively free expansion, while the heavier protein particles see many matrix-protein collisions resulting in an effective radial pressure on the protein plume. The protein and matrix plumes seen in Figure 4 were imaged separately but both were present during the experiment [15].

These results can be used to estimate surface density and sample-NEMS distance parameters. From [15], the plume density of the light-particle matrix can be given as:

$$\rho(r, z) = e^{\left[ \frac{-1}{\gamma-1} \left( \frac{r^2}{R_1^2} + \frac{z^2}{Z_1^2} \right) \right]} \quad (1)$$

Where  $\gamma = c_p / c_v$  is the heat capacity ratio of the gas-phase particles and R1, Z1 are the plume dimensions at some calibration time. Further, it was found that the ratio of the plume axial expansion (Z (t)) to the radial expansion (R (t)) was a constant (equal to 2.5) after a few microseconds. Comparing the PLL timescale of 500ms to the plume expansion timescale of tens of microseconds, the plume ejection is considered to happen instantaneously, and only the final plume density at the device position is considered.

One can then use the above relations to estimate the minimum surface mass density necessary to deposit on the sample plate in order to record a response on the NEMS device above the minimum detectable mass (45kDa, determined as 3-sigma above the resolution –15kDa – set by frequency noise). For a cantilever device with cross-sectional area as shown above (Figure 2), placed 2 cm away from the desorption spot on the sample plate, the minimum estimated surface density is 0.29

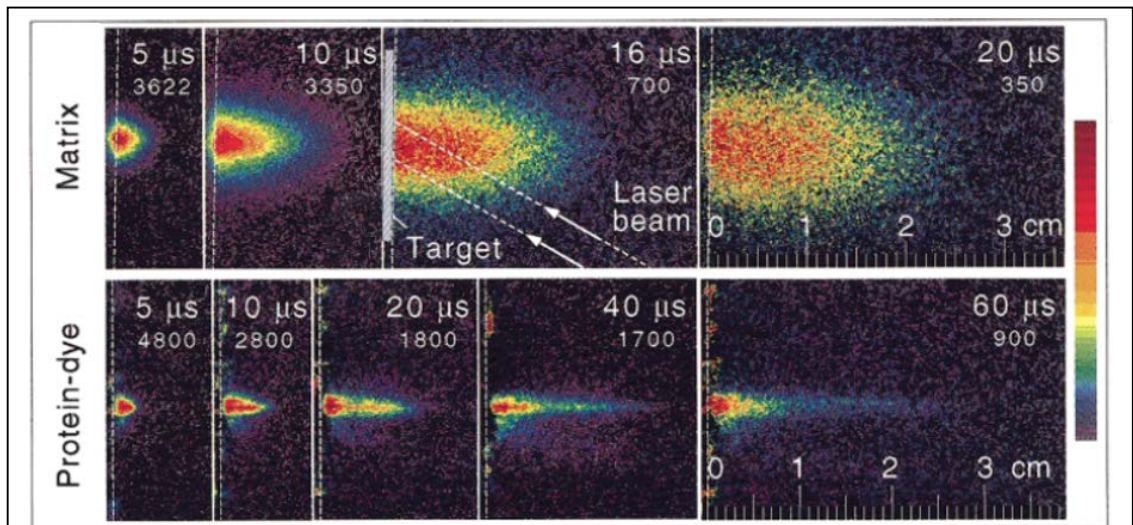
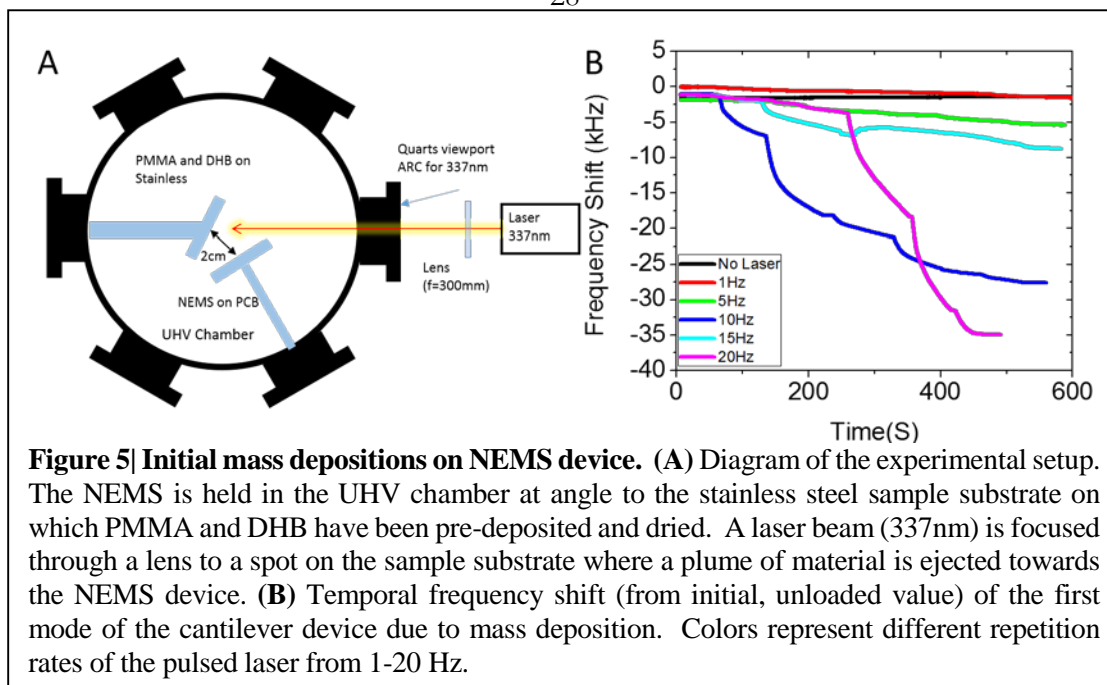


**Figure 4| Image of the MALDI plume (figure reproduced from reference 15).** CCD images of the plume after the designated time since the desorption event. The top row shows the broader plume of the MALDI light-particle matrix while the bottom row reveals a sharpened plume of the heavier protein particles. Details can be found in reference. 15.



mg/cm<sup>2</sup> (assuming a laser spot of 125μm x 125 μm, see below). Further, it is assumed that 700 laser shots are required to fully deplete the desorption spot (this was determined from the experiment described below and is within the commonly reported range of 200-1000 shots [4]).

Initial mass detection results were obtained using 950kDa poly (methyl-methacrylate) (PMMA) as the analyte and 2, 3-Dihydroxybenzoic acid (DHB) as the matrix (both purchased from Sigma Aldrich). The experimental setup (diagrammed in Figure 5a) consisted of the chamber and device as described above with the addition of a pulsed nitrogen laser (model NL100, Stanford Research Systems, 337nm wavelength, 176μJ/pulse, and 3.5ns pulse width) and without the XYZ sample stage. In this case, the laser-focusing lens was placed on a XYZ micrometer and the laser spot was scanned across the sample plate. The laser spot was a rectangular (125 μm)<sup>2</sup> area as determined by burn spots, using a sample with thermally evaporated gold on stainless steel. The laser was designed to have a rectangular beam profile by the manufacturer.

The temporal frequency response of the device is seen in Figure 5b for the first mechanical mode of the device. When the laser was incident on the sample plate, the ejected mass was deposited

on the cooled NEMS device, inducing a negative frequency shift over time. The laser repetition rate was varied from 1-20 Hz and accordingly altered the frequency drift rate of the device. The abrupt shifts in the frequency response, seen most emphatically in the blue and magenta curves in Figure 5b (10 and 20 Hz rep. rates, respectively), reflect the depletion of a sample spot and the manual movement of the laser focus to a new sample on the plate. Approximately 700 laser shots were attained per spot before depletion.

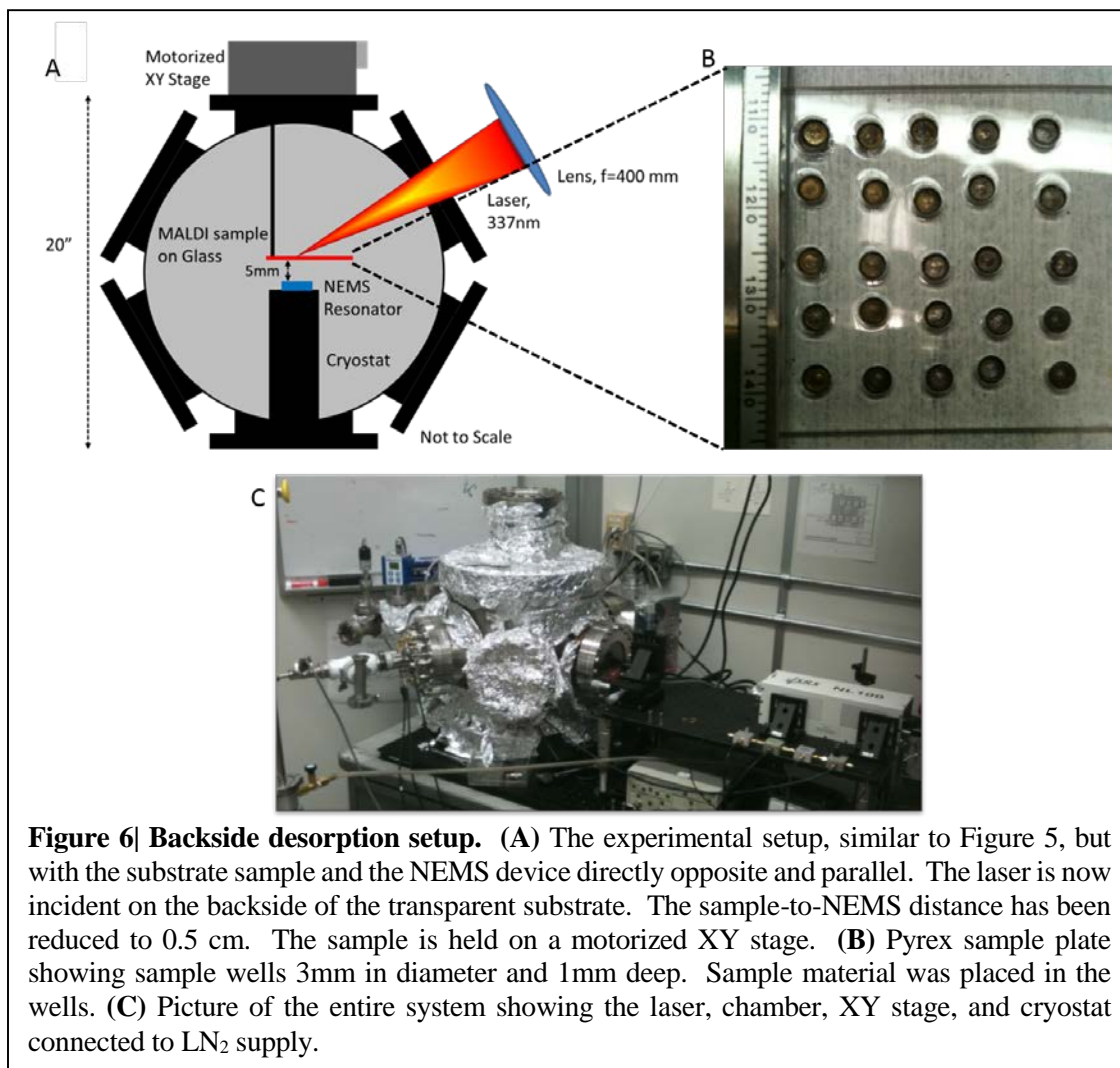
As seen in Figure 5b, as the laser repetition rate is increased, so is the rate of mass deposition on the device. Further, as the sample spot is depleted, the frequency change flattens until the spot is moved to a new region of the sample surface. The lone exception is the curve representing 15 Hz repetition rate, which may have been on an area of the sample surface with much lower mass density. Nonetheless, these results demonstrate mass deposition on the NEMS device in the manner expected. One should note, however, that the frequency shifts are continuous, not discrete jumps, indicating that the mass deposition consisted of many small particles too light to be individually registered by the device. The PMMA mass, 950kDa, is high enough to be registered on the device. The lack of discrete frequency jumps suggests, therefore, that either the PMMA surface density was insufficient to be seen, or the PMMA broke apart during the desorption process.

The sample preparation for this experiment was as follows: PMMA was prepared in a de-ionized (DI) water solution at a concentration of 13 mg/ml. DHB was similarly prepared at a concentration of 15 mg/ml. The solutions were combined at a PMMA:DHB volume ratio of 1:5. The combined solution was then pipetted onto separate spots on a thin, polished, stainless steel sample substrate. The spots were ~2mm in diameter containing 2  $\mu$ l of solution (PMMA+DHB) per spot. The surface density of each spot was then 1.1mg/cm<sup>2</sup>. At surface density values lower than this by a factor of two or more, no signal was registered on the device. This critical surface density (0.55 mg/cm<sup>2</sup>) is within an order of magnitude of the theoretically estimated value (0.29mg/cm<sup>2</sup>).

The plume density calculation is indeed only intended as an order of magnitude estimate. It fails to take into account such details as the angle between the substrate sample and the NEMS device. In order to provide laser access to the substrate sample while simultaneously keeping the substrate sample reasonably close to the device, the substrate sample was turned to an angle approximately 30 degrees from the plane of the device (Figure 5a). This would reduce the plume density seen by the device and increase the required sample surface density. It should be noted that the plume axial direction is determined solely by the direction perpendicular to the substrate surface and is not based on the laser angle of incidence[12]. Moreover, since the laser spot was scanned, the distance between the substrate and the device could change during the experiment (see Figure 5a), which would further reduce the average plume density sampled by the device.

A complete modeling of the MALDI plume in our particular experiment was beyond the scope of this work. The above results demonstrate that initial experimental observations of the LD-NEMS-MS system are in reasonable agreement with theoretical expectations. The critical substrate surface mass density of  $0.55\text{mg}/\text{cm}^2$  with a sample-NEMS distance of 2cm is then a good guide for basic system parameters.

Since the project goal was not simply mass detection but single particle mass measurement, this relatively high surface density was not suitable due to the increased likelihood of sample



bunching effects. It was therefore decided to rearrange the experimental setup to decrease the sample-NEMS distance in order to allow for a reduction in the sample surface density, while maintaining the same particle flux at the device. Additionally, since the protein plume is narrowly focused in the axial direction (Figure 4), proper axial alignment between the NEMS device and the desorption spot was desired. Reducing the sample-NEMS distance, however, made laser access to the sample substrate surface difficult. These considerations motivated the decision to implement a backside desorption process where the laser passes through the back of a transparent sample substrate and is absorbed by the pre-deposited matrix and analyte film.

## 2.4 Backside desorption

Desorption from the backside allows the NEMS device to be placed closer to the substrate sample and to be axially aligned with the particle plume. Together, these will maintain or increase the data event rate at the device without requiring high levels of sample surface density that can lead to complicated bunching effects.

Conventionally, MALDI is usually performed using front side desorption where the particle plume is on the same side of the substrate surface as the laser path. Since the plume is collected by ion optics, there is generally no need for desorption from the backside where the laser path originates from the opposite side of the sample substrate as the ejection plume. Moreover, a conducting substrate enhances the ionization yield in the MALDI process [16], and therefore opaque metal plates are most commonly used.

For LD-NEMS-MS ionization yield is not a concern, though transparent conductors such as indium tin oxide were considered and could be used in the future. Standard microscope glass slides were used (Fisher Scientific) and were found to be adequate for material ejection via the MALDI process. There were no measureable differences in mass ejection efficiency using either glass or stainless steel (the relative ionization efficiency was not measured). Using the transparent glass slides, however, allowed for a reconfiguration of the experimental setup in order to place the NEMS device closer to, and axially aligned with, the analyte plume. This new configuration is shown diagrammatically in Figure 6.

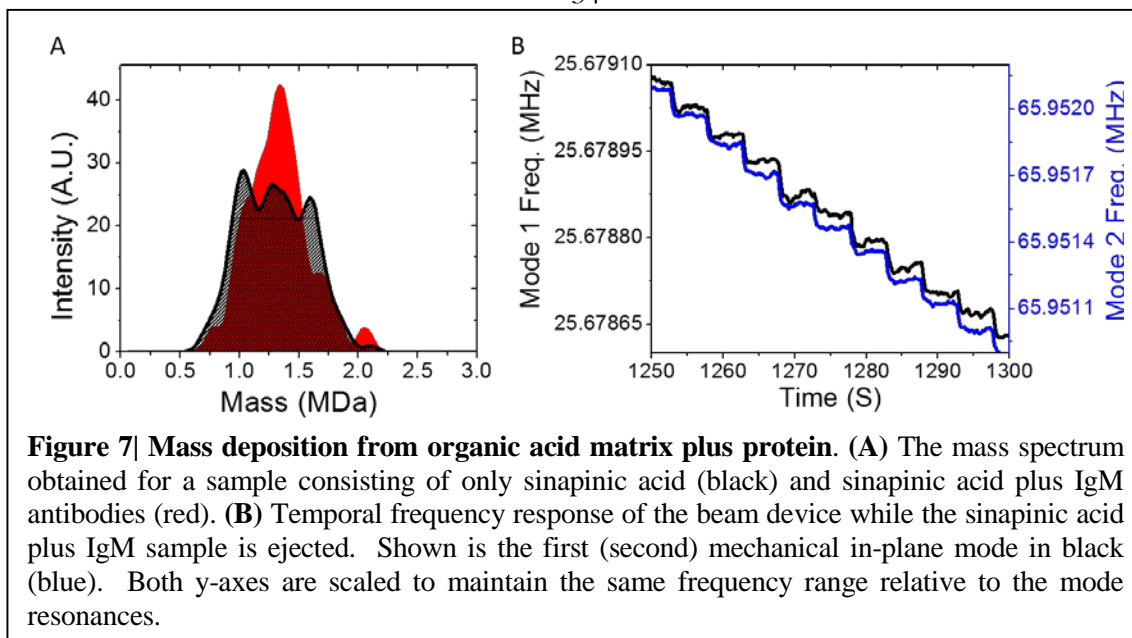
As seen in Figure 6a, the substrate sample is directly opposite and parallel to the NEMS device. This allows for good axial alignment between the NEMS device and the desorption plume, and a decrease in the sample-NEMS distance (now 0.5 mm). The point of closest approach between the sample substrate and the NEMS device is now limited only by the height of the wirebonds on the NEMS device. Future implementations of a LD-NEMS-MS system could alter the NEMS chip

support and connection structure so that the sample-NEMS distance could be further reduced. In an on-chip arrangement, for example, the sample and the NEMS device could be placed arbitrarily close, provided only that there is enough distance for individual particle separation within the plume.

Additionally, the laser spot is now aligned to a spot on the sample substrate directly across from the NEMS device. This was done with an alignment procedure using markings on the PCB and visual observation of the laser spot on the substrate. A more precise procedure could be implemented using, for example, mass deposition from a highly homogenous sample or the frequency shifts induced on the device from direct laser light. During an experiment, the laser then remains fixed and the sample substrate is scanned in X and Y. Given that the estimated diameter of the plume at the device position was 2.1mm (relative to the device size of  $10\mu\text{m} \times 300\text{nm}$ ), the visual alignment procedure proved sufficient.

Another change to the experimental setup was the installation of different NEMS devices. The new devices were doubly-clamped beams also manufactured in collaboration with our partners at CEA/LETI-Minatec. These devices and their control circuitry are fully described in chapter three. The advantage of the new beam devices over the cantilevers used previously is that only two mechanical modes are necessary to deduce the mass of single particles, whereas cantilevers require simultaneous measurement of three mechanical modes [17, 18].

A continuing issue was controlling the sample surface density. Depositing analytes from solution on the glass slides led to significant spreading of the droplets. This made it difficult to attain adequate surface density or maintain consistent sample parameters. The solution was found by engineering wells on the substrate surface in which the liquid solution could be deposited and contained as it dried. In this way, repeated solution deposition and drying steps could be performed to build up large surface density and better control the surface conditions.



In order to maintain use of a transparent substrate, holes were drilled in 2mm thick Pyrex plates. This drilling was done with assistance from Richard Gephart of the Glassblowing Shop maintained by Caltech's Division of Chemistry and Chemical Engineering (who also supplied the Pyrex). The wells were drilled using a flat-end, diamond-tipped drill, 3mm in diameter, to a depth of 1mm. To prevent cracking, the Pyrex plates had to be submerged in water using a custom-built holder supplied by the Glassblowing Shop. An example of the finished Pyrex plate with wells is shown with a scale in Figure 6b. The coloring of the wells seen in Figure 6b is due to residue from previous GNP solutions. After drilling, the well base was flame-polished and laser transmittance experiments verified there was no additional loss of laser intensity seen by the MALDI sample.

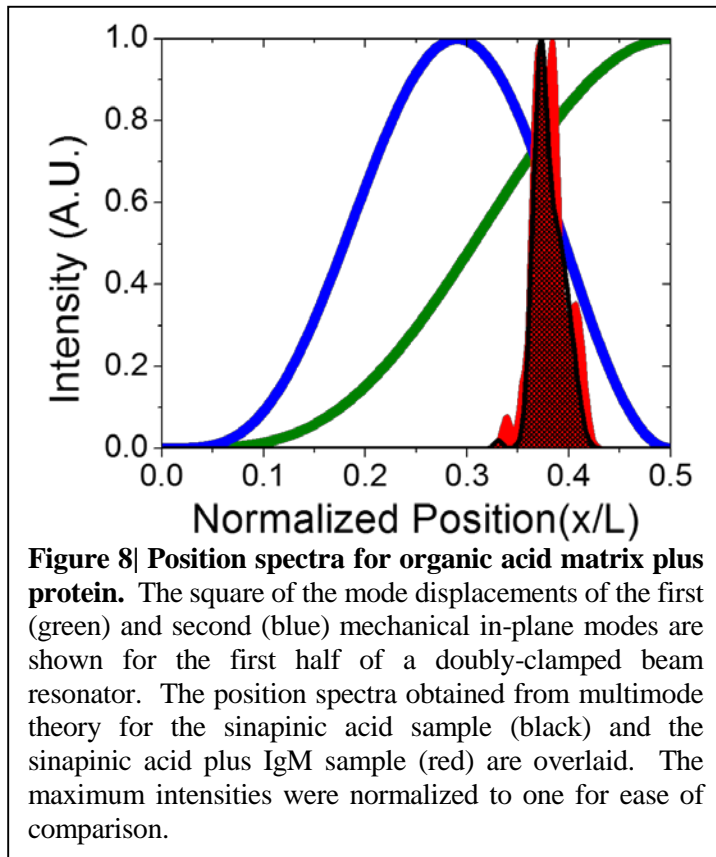
This re-configured, backside desorption system is used in the following experiments and those described in chapter three wherein single GNPs were successfully measured on the NEMS device. A picture of the entire system for backside MALDI-type desorption is shown in Figure 6c.

## 2.5 Traditional MALDI unsuitable for LD-NEMS-MS

Using the backside desorption setup, attempts were made to measure single protein particles. As described in chapter one, traditional MALDI relies on mixing an analyte and matrix together on a sample substrate. The exploding plume consisting of both matrix particles and analytes is then collected by ion optics and the particles are separated according to their mass-to-charge ( $m/z$ ) ratios. Thus, in conventional systems, the matrix particle background does not interfere with the analyte mass spectrum so long as the analytes are of much greater mass than the matrix particles, as is usually the case. There are efforts to overcome or eliminate this light-particle matrix background in order to measure small analytes with MALDI; these are briefly reviewed at the end of this chapter.

In a LD-NEMS-MS system there is no mass-specific particle separation before analyte or matrix arrival at the NEMS detector. Therefore, when using a sample mixture of analyte + matrix, both the matrix particles and the analytes can arrive at the detector within the measurement time (= PLL time constant, 0.5 seconds). This leads to a matrix background that obscures the protein signal. This effect is seen in Figure 7, where sinapinic acid is used as the matrix and IgM antibodies as the analyte protein.

Sinapinic acid (Sigma Aldrich) was mixed in a 50:50 DI water and acetonitrile solution to a concentration of 11 mg/ml. IgM (Sigma Aldrich) was purchased in its lyophilized (powder) form and suspended in DI water. The solution was purified using centrifuge filters (10 kDa), and the final concentration of IgM was 1 mg/ml in DI water with 1% trifluoroacetic acid. Two sample plates were prepared. In the first, the sinapinic acid solution was directly deposited in the Pyrex wells. For the second plate, the sinapinic acid and IgM solutions were mixed at a 1:1 ratio and the combined solution was deposited. For both plates, the solution was deposited in drops of 2.5  $\mu$ l with 10 drops per well and with five minutes of drying time in ambient conditions between drops.



$\sim 7\text{-}10 \times 10^{-8}$  giving a mass resolution of  $\sim 50\text{kDa}$ .

Though the peaks in Figure 7a occur near the expected mass of IgM particles ( $960\text{kDa} \pm 50\text{kDa}$ ), there is little or no difference in the mass spectra between the two samples. It seems, therefore, that the sinapinic acid arrives at the NEMS device as either large mega-Dalton clumps of material or a film spread over some region of the device. If the IgM particles were also arriving at the device, then one should expect a shift to higher mass of the red curve in Figure 7a, relative to the black curve. The shift amount should be nearly equal to the IgM mass ( $960\text{ kDa}$ ) or a multiple thereof. The lack of a shift between the red and black curves of Figure 7a indicates that IgM particles were not landing on the device. This in turn suggests that the IgM was either present in insufficient concentration, or was not efficiently desorbed from the substrate surface. It is possible that the IgM particles experienced fragmentation, but sinapinic acid was chosen in this case because it is a standard

To collect the data, the dried sample plates were installed in the chamber, which was then pumped down to a pressure of  $3 \times 10^{-9}$  Torr. The laser was pulsed at 1Hz and the sample plates manually scanned across the fixed laser spot. The mass spectral results are seen in Figure 7a where the red (matrix + analyte) and the black (matrix alone) overlap almost entirely. The Allan Deviation of the two modes was

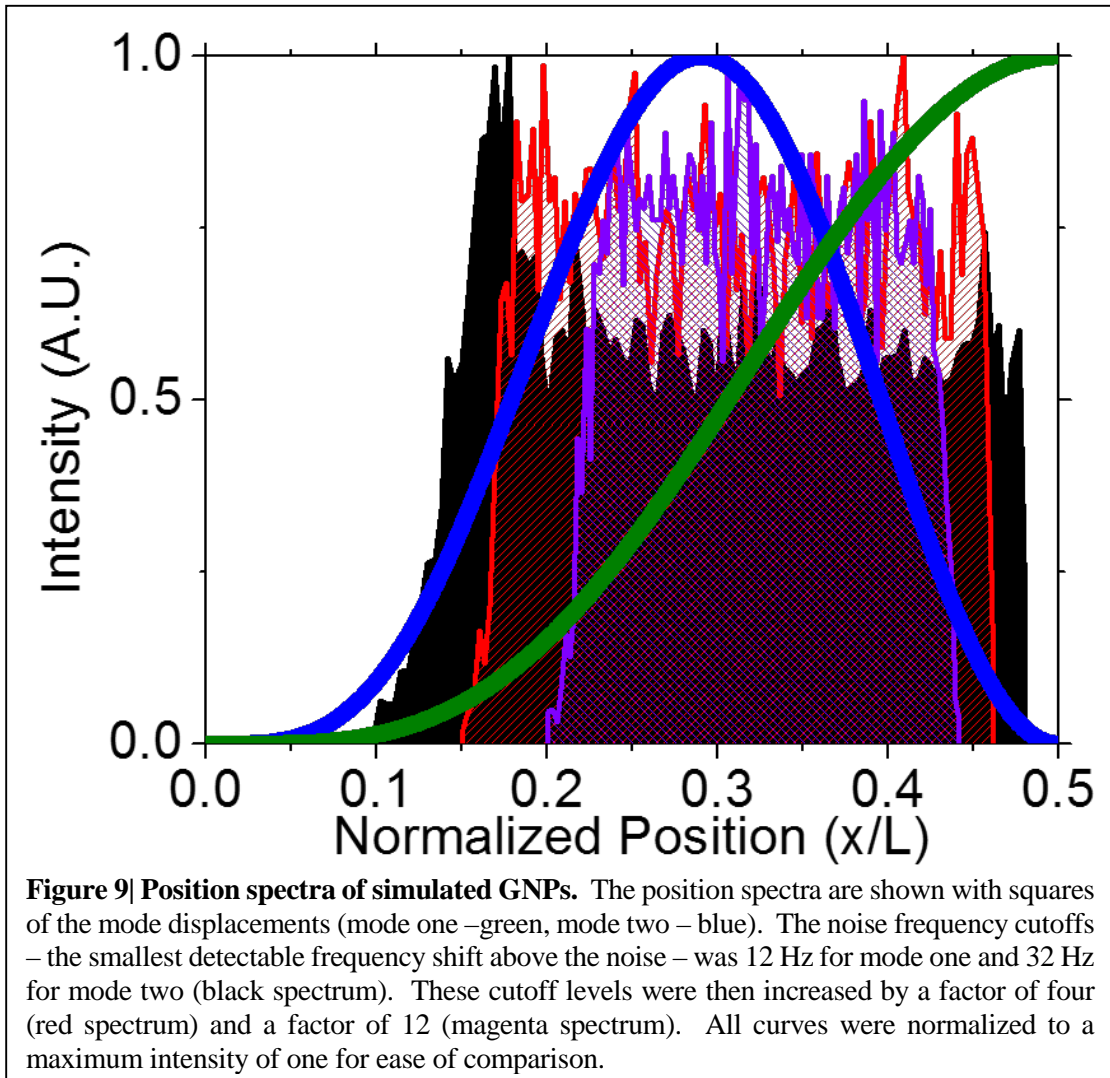
and well-validated matrix compound for MALDI used with a variety of large proteins [14], and no IgM fragmentation was to be expected.

The conclusion that the mass spectra of Figure 7a represent only clumps of matrix material is supported by the temporal frequency data display in Figure 7b. Multimode theory [18] shows that when single particles of the same mass randomly arrive on the device, the frequency shifts are accordingly stochastically sampled according to the landing position. The position dependence of the frequency shift induced by a point particle landing on the device reflects the effect the particle has on the kinetic energy of the beam [1, 17]. The effect on kinetic energy is largest at points of maximal beam displacement (the antinodes of the mode shapes), and is zero at point of no displacement (the nodes of the mode shapes). The temporal frequency response of the device, therefore, should show frequency jumps that are not only of different relative heights in the two modes for the same event, but also of different heights in the same mode from event to event.

If, on the other hand, a film of material is spread out evenly over the device surface, the effect on kinetic energy is integrated across the whole mode shape – the frequency jumps have no position dependence. Thus, deposition of repeated films of the same mass will produce frequency jumps of the same size, in a particular mode. Moreover, the relative frequency response of two modes will also be the same in this case because there is no position-dependency – the mode shape does not matter.

As seen in Figure 7b, the relative frequency jump heights are the same from event to event and are nearly the same in the two modes. This is more consistent with the latter process of repeated film deposition than single-particle landing events.

However, if the operator mistakes the thin films coating the device for single particles and follows multimode theory analysis to calculate the mass and position of a single particle (as done in Figure 7 for the mass), then the position calculated by the theory will have a characteristic shape.



Specifically, the distribution will be narrowly peaked around the point on the beam where the relative frequency shifts of the two modes are equal. Because the frequency shift is proportional to the square of the mode displacement, the distribution peak will occur at the beam position where the squared mode displacements are equal. This is visually represented in Figure 8.

The frequency jump pairs displayed in Figure 7b are assumed to originate from single-particles and are then used to calculate the position distribution of these “particles”. As seen in Figure 8, the position spectra for both samples are highly peaked at the mode crossover point,  $x/L \cong 0.36$ . The fact that both samples are peaked around this position suggest that the events recorded from both

samples consist largely of small particles that arrive as clumps or films on the device. There is likely significant inhomogeneity in the distribution of material on the device from event to event and this accounts for the small spread in the position spectra around the peaked position. Additionally as the spectra from the two samples almost directly overlay, it is very unlikely any IgM particles were detected and that in both cases the signal on the NEMS device is dominated by large clumps of material.

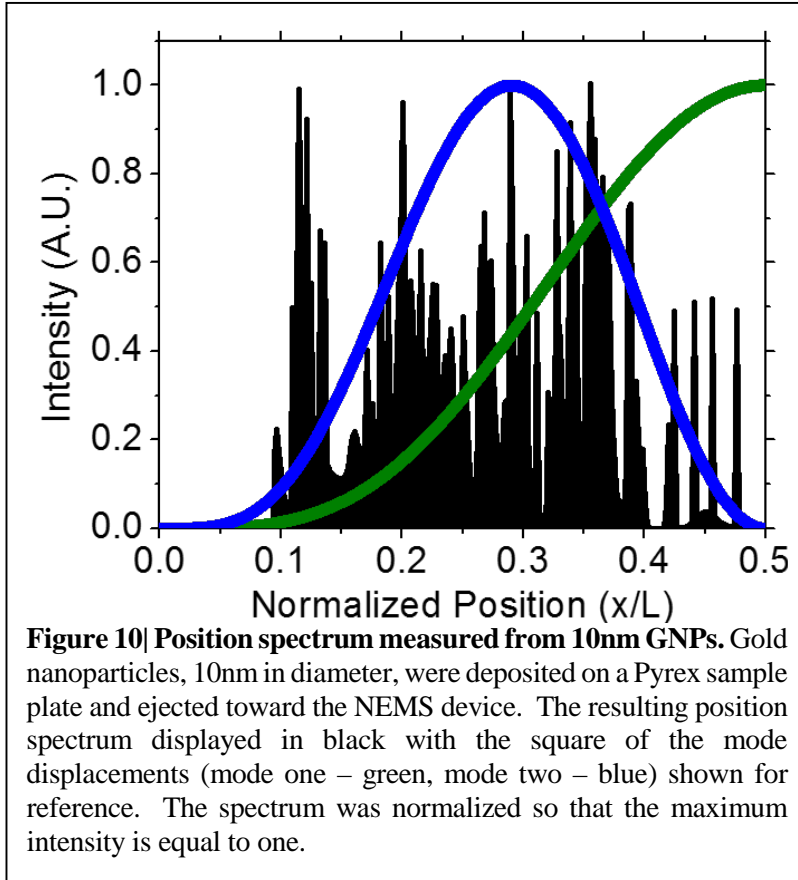
In the true case of single point-sized particle landing events, the position spectrum should appear as a flat distribution across the device with position cutoffs defined by the frequency noise and the relative particle sizes. This situation is visualized using a Monte Carlo simulation of GNPs (5nm diameter) randomly arriving on the device (Figure 9). The frequency noise limits the smallest detectable frequency shift for a particle of a given mass. Considering one mode of the device and fixing particle mass, as the landing position approaches the nodes, the frequency shift is reduced by an amount dictated by the mode shape. As the particle lands progressively closer to a nodal point, the induced-frequency shift will eventually be less than the experimental frequency noise. In that case, the event is not registered. In the position plane, this frequency noise then leads to a position cutoff at some distance from the nodes. Beyond those positions no particles can be registered. For a fixed amount of the frequency noise, then, more massive particles will have a broader range of detectable positions, while lighter particles will have a more narrow range.

In our experiments, the particle measurement is based on detection of two device modes. For the event to be counted, the simultaneous frequency shifts in *each* mode must be greater than the noise level of the respective mode (a 3-sigma threshold level is used in experiments). Thus, the range of measureable positions for randomly arriving particles is limited by the mode that has the larger position cutoff.

For the spectra shown in Figure 9, the noise cutoffs were based on the experimentally measured frequency noise. The black curve represents the simulated spectra of GNPs randomly arriving on the device where the minimum measurable frequency shifts were 12 Hz for mode one and 32 Hz for mode two. As the simulated frequency noise was increased by a factor four, the position spectrum narrowed (Figure 9, red curve). The noise was then further increased by a factor of 12, producing the magenta curve. Thus, as the frequency noise is increased, the range of possible position values is shrunk until the noise is so high that particles of that mass cannot be measured at any position on the beam. If the frequency noise is reduced, the range of possible position values will correspondingly expand. The 5 nm GNPS had a simulated mass of 760kDa, with a standard deviation of 10%. Using more massive particles, with the same level of frequency noise, would then produce position spectra over a wider area of the device.

Indeed, measurements of 10nm gold nanoparticles, which are more fully analyzed in Chapter three, reveal a relatively flat position distribution, shown in Figure 10. These heavy gold nanoparticles have a high level of signal-to-noise (greater than 90) and are thus easily detectable across almost the full range of the device. As seen in Figure 10, the position distribution terminates at points closer to the nodes, compared with the simulations of 5nm GNPS. Comparing Figure 10 to Figure 8, one sees that single-particle measurements are indeed spread evenly over the device within the frequency-noise defined position cutoffs, while measurements of distributed films of light material appear as narrow peaks around the cross-over point. The details of the sample preparation and measurement conditions for these 10nm GNP measurements are given in Chapter three.

This analysis shows that the position spectra can be used as a diagnostic tool when developing a LD-NEMS-MS system. If the temporal frequency response reveals jumps of the same relative heights across many events (as in Figure 7b) and the position spectra are highly peaked around the



cross-over point between the squares of the mode displacements, then it is likely that the results represent bunching of small particles as opposed to single particle measurements.

## 2.6 Gold nanoparticles as matrix

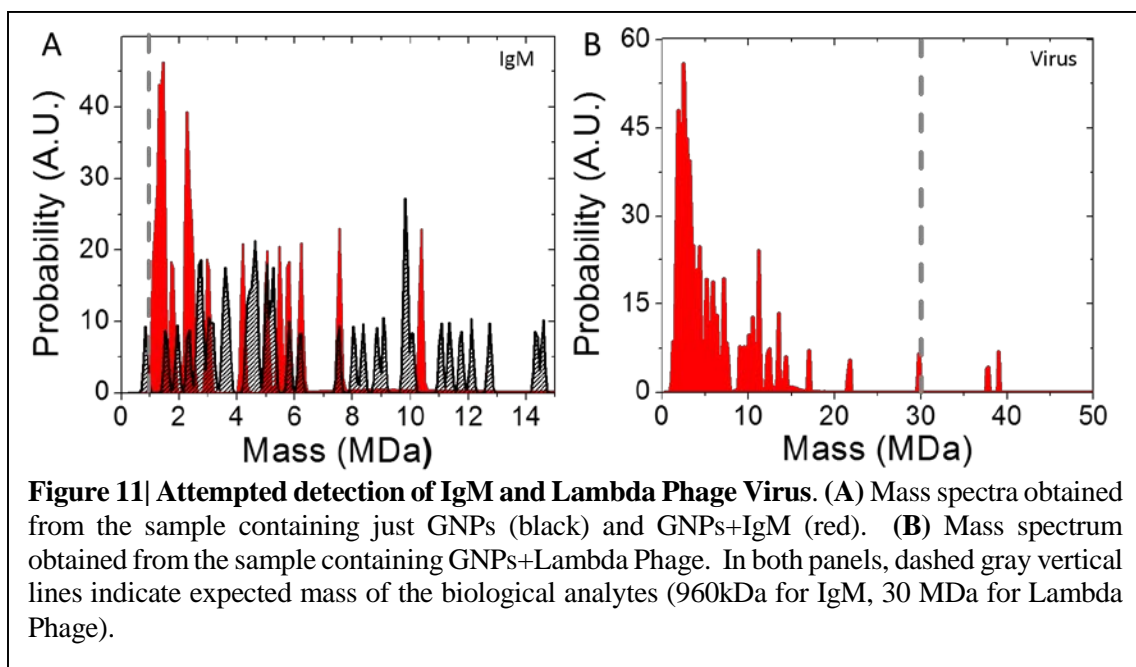
Matrix materials featuring light, organic acids, such as sinapinic acid or DHB, are most common in traditional MALDI applications. Following Tanaka's discovery that micro- or nano-metallic particles can be used for the successful desorption of larger proteins [19, 20], metallic nanoparticles are currently often used to shift the usual matrix background into the high-mass regime and permit the MALDI analysis of low mass analytes that would otherwise be obscured by lighter matrices [21-24].

Because attempts to use light particle organic acids resulted in mega-Dalton level clumping across the NEMS device, it was decided to attempt to use gold nanoparticles as the matrix in order to enable protein detection. Unlike the above-cited studies, the gold nanoparticles are in the same mega-Dalton mass range as the proteins to be measured. However, it was expected that since the LD-NEMS-MS system counts particles one at a time, the GNPs would appear as a regular, well-calibrated peak in the mass spectra, separated from the protein mass peaks.

Colloidal gold nanoparticles (5nm, Sigma-Aldrich) were concentrated and buffer-exchanged in a centrifuge to a final concentration in DI water solution of  $5.5 \times 10^{14}$  particles/ml. For some samples, the nanoparticle solution was mixed with an IgM solution (8mg/ml in DI water and 1% trifluoroacetic acid) at a volume ratio of 1:1. For these IgM+GNP samples, 15 drops with 2.5  $\mu$ l/drop were deposited in each of the Pyrex sample wells. In other samples, the GNP solution was mixed with inactivated lambda phages ( $1 \times 10^8$  particles/ml), also at a 1:1 volume ratio. For these virus+GNP samples, 20 drops with 2.5  $\mu$ l/drop were deposited in each of the Pyrex sample wells. The plates were thoroughly cleaned between experiments by washing in methanol, IPA, and acetone. Sometimes gold etchant was also used to remove dried GNP residue. Thorough washing in purified water before and after application of gold etchant was performed and appropriate safety protocols were observed at all times.

After drying, the samples were inserted into the vacuum chamber, which was then pumped down to the operating pressure of  $2 \times 10^{-9}$  Torr. The laser was incident on the backside of the samples at a repetition rate of 1Hz. The samples were manually scanned in X and Y across the wells while the NEMS device was continually tracked in both modes. The resulting frequency jumps were selected at the 3-sigma level above the noise and the mass and position spectra were calculated. The frequency noise was the same as above for the doubly-clamped devices, giving a mass resolution of 50kDa.

The results of these experiments are displayed in Figure 11. The black curve in Figure 11a shows the spectrum resulting from only GNPs, while the red represents the GNP+IgM sample. It is immediately apparent that the GNPs, instead of appearing as a single peak as expected, have a very broad and randomized mass range. This is due to both the high variance in the particle diameters in the original sample (20%), and the tendency of particles to bunch together either in solution or during drying on the sample plate (or both). The red curve does reveal a relatively higher intensity near the expected IgM mass, indicated by the vertical dashed gray line, but given the spread of GNPs mass over the same range, there is insufficient evidence to conclude that IgM was detected from this



sample. Additionally, the spread of the GNP mass spectrum suggests they are unsuitable as a matrix for mega-Daltons analytes, even if the GNPs are successful in ejecting the analytes intact to the detector.

In order to attempt to measure an analyte with nominal mass (30 MDa) above the GNP range, the viral (lambda phage) sample was prepared and measured, as described above. The mass spectrum resulting from this sample is displayed in Figure 11b. The GNP background is concentrated in the range of a few mega-Daltons. As seen in the figure, there are peaks of relative low intensity at the expected viral mass, indicated by the vertical dashed gray line, but the height is too small relative to other scattered peaks near 20 and 40 MDa to suggest that this is indeed evidence of viral detection.

## 2.7 Conclusion

In summary, I have shown the motivation and the design steps for constructing an apparatus to perform NEMS-MS using laser desorption for analyte delivery to the NEMS detector without ion optics. This has entailed identifying the optimal pressure regime and the combination of sample surface density and distance to the device. It has been shown that a backside desorption technique using a transparent substrate with machined wells works to deliver single gold nanoparticles to the device. This setup has also revealed, however, that the traditional MALDI approach of protein analyte plus light-particle matrix is unsuccessful due to the high background induced by the matrix. Finally, while gold nanoparticles can be individually detected in such a setup, they do not serve as a proper matrix medium for proteins in the hundreds of kilo-Dalton to mega-Dalton mass range.

One can imagine that the method of analyte + organic acid could be made compatible with a NEMS-MS system. In particular, given the results from [15] – where the lighter matrix is a rapidly expanding plume but the heavier proteins are a sharply focused plume – it may be possible to significantly reduce the matrix background effect by, for example, increasing the sample-NEMS

distance and more careful alignment between the desorption spot and the NEMS. Increasing the distance would significantly reduce the data collection rate, however--the optimization of which was one of the key motivations of the project. In the future, utilizing a dense array of many NEMS devices may be compatible with this approach. Additionally, useful mass spectrometry of proteins requires a robust methodology with no background contamination. Thus, in order to avoid the use of ion optics and maintain the neutral detection advantage of NEMS, a background-free protein desorption mechanism is the preferred method.

Of the laser-based protein desorption techniques, there are several interesting options. Surface assisted laser desorption ionization (SALDI) is one wherein the substrate surface is often coated with a material (such as gold nanoparticles). As seen from attempts at using GNPs as a matrix, for such a technique to be compatible with NEMS-MS, the surface coating would have to desorb the proteins without presenting any kind of background at either the low or high mass range. There exist other, more exotic SALDI techniques, such as coating the surface with carbon nanotubes, that may be worthy of further investigation for NEMS-MS [25].

A popular SALDI technique for background-free protein delivery is desorption ionization on silicon (DIOS) [25-27], in which a porous silicon substrate interacts with the laser light to promote biomolecules to the gas phase. However, DIOS has limited desorption ability in the high mass range [26] and may therefore be unsuitable for the large (>200 kDa) proteins that are the current target of NEMS-MS. A successor to DIOS is nanostructure initiator mass spectrometry (NIMS), in which a nanoporous silicon surface is coated with a thin film (such as Teflon) [28, 29]. NIMS, however, experiences similar upper mass limits as DIOS [28] and the initiator surface may also present a neutral background to which the NEMS device is sensitive. The source of the upper mass limit for DIOS and NIMS is not yet fully understood. Nonetheless, these techniques are worthy of investigation for

compatibility with LD-NEMS-MS, especially as the mass sensitivity of NEMS devices continues to improve.

While the detection of gold nanoparticles is an important initial demonstration of the feasibility of an LD-NEMS-MS system and for validation of multimode theory (discussed in Chapter three), it is necessary to implement a background-free technique for proteins that can operate in the high mass range. Such a technique is laser-induced acoustic desorption (LIAD). The successful implementation of LIAD to measure single proteins with a NEMS device is the topic of Chapter four.

## 2.8 Bibliography

1. Naik, A.K., et al., *Towards single-molecule nanomechanical mass spectrometry*. Nat Nanotechnol, 2009. **4**(7): p. 445-50.
2. Heck, A.J.R., *Native mass spectrometry: a bridge between interactomics and structural biology*. Nature Methods, 2008. **5**(11): p. 927-933.
3. Kaddis, C.S., et al., *Sizing large proteins and protein complexes by electrospray ionization mass spectrometry and ion mobility*. Journal of the American Society for Mass Spectrometry, 2007. **18**(7): p. 1206-1216.
4. Cole, R.B., *Electrospray and MALDI mass spectrometry: fundamentals, instrumentation, practicalities, and biological applications*. 2011: Wiley.
5. Ekinci, K.L. and M.L. Roukes, *Nanoelectromechanical systems*. Review of Scientific Instruments, 2005. **76**(6).
6. Mile, E., et al., *In-plane nanoelectromechanical resonators based on silicon nanowire piezoresistive detection*. Nanotechnology, 2010. **21**(16).
7. Allan, D.W., *Statistics of atomic frequency standards*. Proceedings of the IEEE, 1966. **54**(2): p. 221-230.
8. McDonnell, L.A. and R.M. Heeren, *Imaging mass spectrometry*. Mass Spectrom Rev, 2007. **26**(4): p. 606-43.
9. Chaurand, P., et al., *Imaging mass spectrometry: Principles and potentials*. Toxicologic Pathology, 2005. **33**(1): p. 92-101.
10. Chaurand, P., et al., *New developments in profiling and imaging of proteins from tissue sections by MALDI mass spectrometry*. Journal of Proteome Research, 2006. **5**(11): p. 2889-2900.
11. Vertes, A., *Laser Desorption of Large Molecules - Mechanisms and Models*. Methods and Mechanisms for Producing Ions from Large Molecules, 1991. **269**: p. 275-286.
12. Dreisewerd, K., et al., *Influence of the Laser Intensity and Spot Size on the Desorption of Molecules and Ions in Matrix-Assisted Laser-Desorption Ionization with a Uniform Beam Profile*. International Journal of Mass Spectrometry, 1995. **141**(2): p. 127-148.
13. Dreisewerd, K., *The desorption process in MALDI*. Chemical Reviews, 2003. **103**(2): p. 395-425.

14. Karas, M. and R. Kruger, *Ion formation in MALDI: The cluster ionization mechanism*. Chemical Reviews, 2003. **103**(2): p. 427-439.
15. Puzos, A.A., et al., *Imaging of vapor plumes produced by matrix assisted laser desorption: A plume sharpening effect*. Physical Review Letters, 1999. **83**(2): p. 444-447.
16. M. Shaghoul, C.I.O.T., *Private Correspondance*.
17. Hanay, M.S., *Towards Single-Molecule Nanomechanical Mass Spectrometry*, in *Physics*. 2011, California Insitute of Technology.
18. Hanay, M.S., et al., *Single-protein nanomechanical mass spectrometry in real time*. Nature Nanotechnology, 2012. **7**(9): p. 602-608.
19. Tanaka, K., et al., *Protein and polymer analyses up to m/z 100 000 by laser ionization time-of-flight mass spectrometry*. Rapid Communications in Mass Spectrometry, 1988. **2**(8): p. 151-153.
20. Tanaka, K., *The origin of macromolecule ionization by laser irradiation (Nobel lecture)*. Angewandte Chemie International Edition, 2003. **42**(33): p. 3860-3870.
21. Su, C.L. and W.L. Tseng, *Gold nanoparticles as assisted matrix for determining neutral small carbohydrates through laser desorption/ionization time-of-flight mass spectrometry*. Anal Chem, 2007. **79**(4): p. 1626-33.
22. McLean, J.A., K.A. Stumpo, and D.H. Russell, *Size-selected (2-10 nm) gold nanoparticles for matrix assisted laser desorption ionization of peptides*. J Am Chem Soc, 2005. **127**(15): p. 5304-5.
23. Wen, X.J., S. Dagan, and V.H. Wysocki, *Small-molecule analysis with silicon-nanoparticle-assisted laser desorption/ionization mass spectrometry*. Analytical Chemistry, 2007. **79**(2): p. 434-444.
24. Castellana, E.T. and D.H. Russell, *Tailoring nanoparticle surface chemistry to enhance laser desorption ionization of peptides and proteins*. Nano Lett, 2007. **7**(10): p. 3023-5.
25. Law, K.P. and J.R. Larkin, *Recent advances in SALDI-MS techniques and their chemical and bioanalytical applications*. Analytical and Bioanalytical Chemistry, 2011. **399**(8): p. 2597-2622.
26. Lewis, W.G., et al., *Desorption/ionization on silicon (DIOS) mass spectrometry: background and applications*. International Journal of Mass Spectrometry, 2003. **226**(1): p. 107-116.
27. Guo, Z., et al., *Nanomaterials in mass spectrometry ionization and prospects for biological application*. Analytical and Bioanalytical Chemistry, 2006. **384**(3): p. 584-592.
28. Northen, T.R., et al., *Clathrate nanostructures for mass spectrometry*. Nature, 2007. **449**(7165): p. 1033-6.
29. Greving, M.P., G.J. Patti, and G. Siuzdak, *Nanostructure-initiator mass spectrometry metabolite analysis and imaging*. Anal Chem, 2011. **83**(1): p. 2-7.

## *Chapter 3*

# SINGLE-PROTEIN NANOMECHANICAL MASS SPECTROMETRY IN REAL TIME

### **3.1 Introduction**

Nanoelectromechanical systems (NEMS) resonators can detect mass with exceptional sensitivity. NEMS-based mass spectrometry (MS) has been previously demonstrated, with statistical analysis being used to assemble simple mass spectra from only a few hundred molecular adsorption events. In this work is reported the first realization of single-molecule NEMS-based mass spectrometry in real time. As each molecule in the sample is detected, its mass and the position of adsorption are determined by continuously tracking multiple, driven vibrational modes of a NEMS resonator. This demonstrates the potential of NEMS-based mass spectrometry by analyzing IgM antibody complexes and gold nanoparticles (GNPs) in real-time.

The work presented in this chapter was performed in close collaboration with Dr. Selim Hanay of the Roukes group, with whom I share co-first author credit on the publication arising from this work [1]. My contribution in that effort included the construction and operation of a NEMS-MS vacuum apparatus utilizing laser-based desorption for particle measurement. This system was successful in performing single particle mass spectrometry of GNPs (GNPs) using matrix assisted laser desorption ionization (MALDI). These measurements provided an initial test and verification of multimode theory, the analytic technique by which the frequency response of a NEMS resonator

is used to calculate the mass and landing position of particle adsorbates. These GNP measurements were overseen by Prof. Akshay Naik.

Additionally, Dr. Hanay and I together rebuilt a modified version of a pre-existing vacuum apparatus utilizing electrospray ionization (ESI) and in-vacuum ion optics to deliver particles to a NEMS detector for single-molecule mass spectrometry. Together, we operated this chamber to obtain mass spectra of individual IgM proteins, the world's first demonstration of real-time single-protein mass spectrometry. The measurement of biological species was crucial for demonstrating the utility of NEMS -MS for proteomics.

The published work [1] also presents multimode theory. This theory was entirely developed by Dr. Hanay and others in the Roukes prior to my arrival and is not part of my original thesis work. Since this chapter presents a proof-of-concept demonstration and test of this theory, the reader is highly encouraged to review the theoretical explanations in the main article and supplementary information of [1], as a theoretical understanding is advantageous for proper critical review of the experimental results presented herein. More complete details regarding multimode theory can be found in [2].

## **3.2 Motivation**

Mass spectrometry – the identification of species through molecular mass measurements – is an important analytical tool in chemical and biological research. Since its first applications to organic compounds more than a half-century ago [3, 4], it has assumed an increasingly dominant role in the life sciences and medicine. It is now arguably the mainstay of proteomics [5].

Among recent emerging areas of MS is the elucidation of the structure of complex protein assemblies [6-9]. Critical to such measurements are spectrometers that are capable of high resolution in the very large mass range – above several hundred kDa – which is at or beyond the limit of many

conventional MS techniques. Also essential is the development of new, delicate molecular sample handling methods for ionization/injection, enabling so-called “native” MS [6, 10], to permit large molecules or molecular assemblies to be transported, intact, from the fluid phase to the vacuum phase for subsequent analysis. On these new fronts, NEMS-MS offers significant promise [11-18]. NEMS are sensitive to the inertial mass of neutral particles that accrete upon them; this makes them particularly well suited to studies that require minimal ionization to avoid structural changes in the protein [6, 10].

The principles and ultimate practical limits of NEMS-based mass detection are discussed elsewhere [19]; here the salient points are briefly reviewed. Upon adsorption onto a NEMS resonator, an *individual* analyte molecule or particle can precipitously downshift the resonant frequency of each vibrational mode [1]. This is the basis of the measurement. Theoretical limits to inertial mass resolution from frequency-shift detection can apparently be as small as the single-Dalton level [17]; indeed, recent endeavors already report mass resolution near this benchmark [20]. However, central to the present work is that all previous measurements neither measure the mass of *individual molecules* or nanoparticles, nor can do so in *real time*. This is despite the impressive recent improvements in mass resolution and the detection of discrete adsorption events [18]. The reason for this is that the resonant frequency shift induced by analyte adsorption depends upon both the mass of the analyte and its precise location of adsorption upon the NEMS resonator.

A way out of this quandary, and the first construction of NEMS-MS spectra – albeit, not in real time – has previously been achieved by employing the known position-dependent mass response behavior for a doubly-clamped NEMS resonator[18]. In this previous work, analytes were delivered such that they accreted uniformly across the device; this foreknowledge allowed the deduction of the constituents of simple mixtures after collection of only several hundred single-molecule adsorption events. (For comparison, conventional mass spectrometry measurements typically involve

measurement of  $\sim 10^8$  molecules [21].) The analysis involved fitting to the statistical ensemble of measured frequency shifts by a rather complex multidimensional minimization procedure to extract the weights of each constituent, that is, to deduce the mass spectrum [2, 18]. These first results provided a conceptual demonstration of the potential of NEMS-MS, but the complexity of this process precluded its application to arbitrarily complex mixtures.

The multimode approach enables direct determination of the mass of *each* arriving molecule, in *real time*, as it adsorbs upon the NEMS resonator [22, 23]. It is, therefore, directly applicable to arbitrarily complex mixtures, as demonstrated below. This approach involves no assumptions about the sample mixture, and is implemented by simultaneously tracking the resonant frequency of multiple modes of an individual NEMS resonator and then resolving the time-correlated, adsorption-induced frequency jumps in several of these modes. Pairs of these simultaneous jumps herald a single-molecule adsorption event and are used in the analytical framework [1] to deduce the nominal values of the mass and position of adsorption of individual molecules/particles just after adsorption. Multimode theory also includes error analysis; using the complete expression for the mode shapes enables direct determination of the mass and position uncertainty of each arriving molecule or particle [1, 2, 23].

Multimode theory provides both a numerical and a universal graphical approach to calculate the mass and position of the analyte molecule, which arrives randomly in time and position [1]. Other work [22, 23] has explored the sequential (as opposed to real-time) use of multiple vibrational modes to detect the position and mass of micro-scale test particles (as opposed to molecules or nanoparticles) that were placed statically and deterministically (as opposed to randomly) on a MEMS or NEMS device [24-26]. None of these aforementioned approaches are directly applicable to the work reported here.

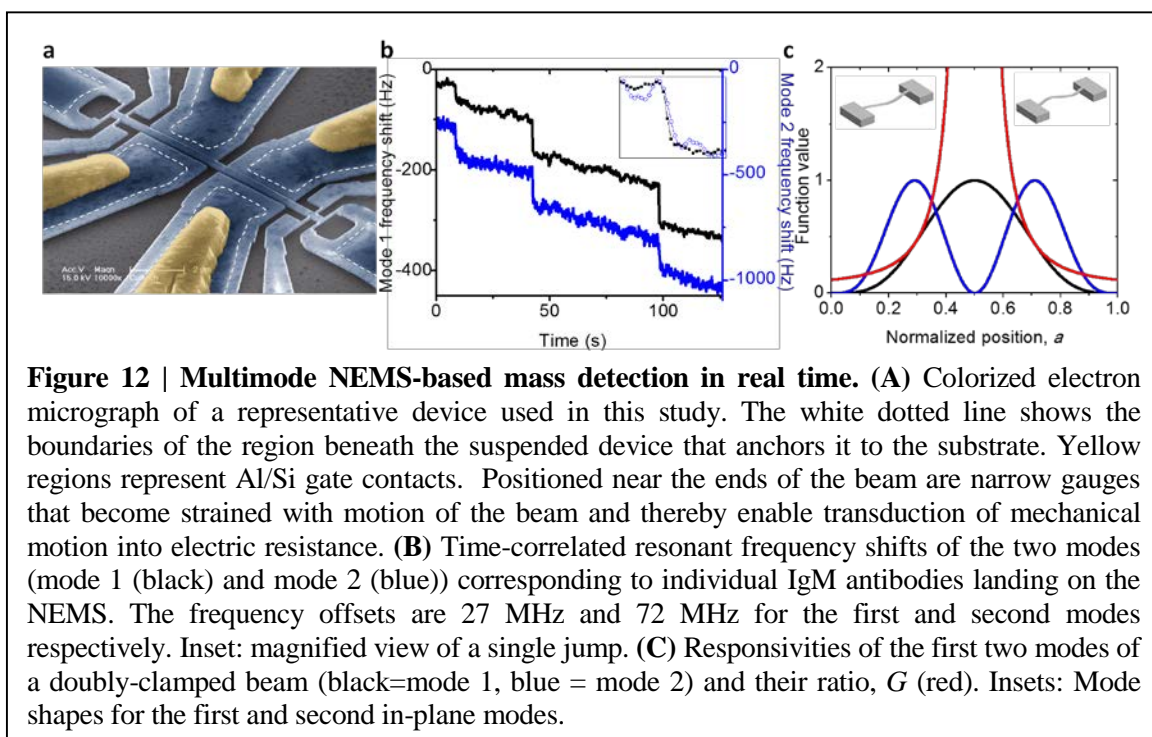
### 3.3 Experimental technique

In this work, the first two modes of the NEMS device are used for mass measurements of individual protein macromolecules (IgM antibody isoforms) and individual GNPs. A colorized scanning electron microscope (SEM) image of one representative device used in the experiments is shown in Figure 12a. The device is fabricated by CMOS-compatible, top-down processes designed for very-large-scale integration of NEMS[1]. Electrostatic actuation is achieved using proximal capacitive gates, and resonator motion is transduced using symmetric semiconducting piezoresistive strain gauges located near both ends of the device.

Each species that physisorbs onto the cooled NEMS device produces a distinct frequency shift in each of the tracked modes (the fundamental and second mode), as shown in Figure 12b. These time-correlated frequency shifts are then used to determine both the mass and position-of-adsorption for *each* of the newly arrived analyte molecules or particles, as well as their corresponding uncertainties.

The mode responsivities are shown in Figure 12,c as well as their ratio function,  $G$ . The ratio function can be used to locate the particle position from which the particle mass can be calculated using the responsivity of either mode. This method produces the centroids of the two-dimensional probability density functions produced by multimode theory [1].

For device control, actuation and detection channels of the two modes were combined using high-frequency electronic components, and a feedback loop [27] was implemented through GPIB protocol. A schematic of the measurement circuit is shown in Figure 13. The NEMS resonators used in both the ESI and MALDI experimental setups were controlled and monitored using multimode readout circuitry schematically depicted in Figure 13. A piezoresistive down-conversion method was employed for the transduction of the mechanical motion [28]. For each mode, one function generator (Rhode and Schwartz model SM03 or Agilent model N5181A) was used to excite the drive electrode at the resonance frequency, and another function generator was used to bias the readout electrodes at a frequency slightly detuned from the resonance. These two signals generate a mix-down signal of mechanical origin at the readout electrode when the drive frequency matches the mechanical resonance frequency. This low-frequency readout signal was amplified and fed into a lock-in amplifier (Stanford Research Systems model SR830), with a matching external reference generated from the two function generators.



For each mode the drive and bias signals were split. On one path, the bias and drive signals were mixed and the output used as the reference for the lock-in amplifier. On the other path, the drive signals for both modes were combined together with a DC source, and the total signal ( $V_1(\omega_{d1}) + V_2(\omega_{d2}) + V_{DC}$ ) was sent to the gate electrode that capacitively actuated the device. Meanwhile, the bias signals for each mode were split in an 180° splitter and the same-polarity signals of both modes were combined and sent to the device. At the device, the bias 1 electrode was charged to  $V_1^+(\omega_{b1}) + V_2^+(\omega_{b2})$ , and the bias 2 electrode to  $V_1^-(\omega_{b1}) + V_2^-(\omega_{b2})$ . The control loop is implemented by reading the lock-in amplifier signal on a computer which performs a corrector calculation and then sends a control signal to the function generators. Details of the corrector calculation are given in [27]. The lock-in amplifiers and the function generators were connected to the computer by a GPIB interface.

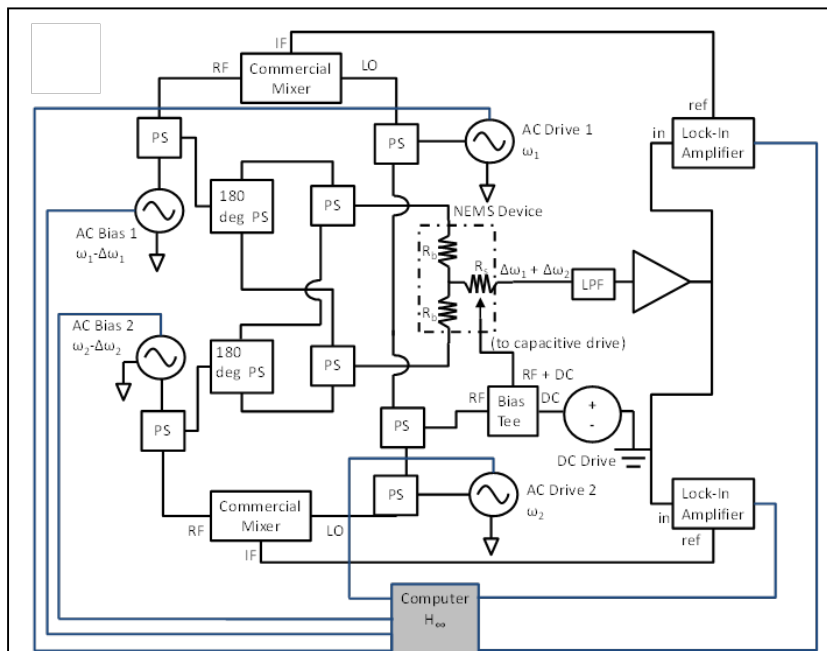
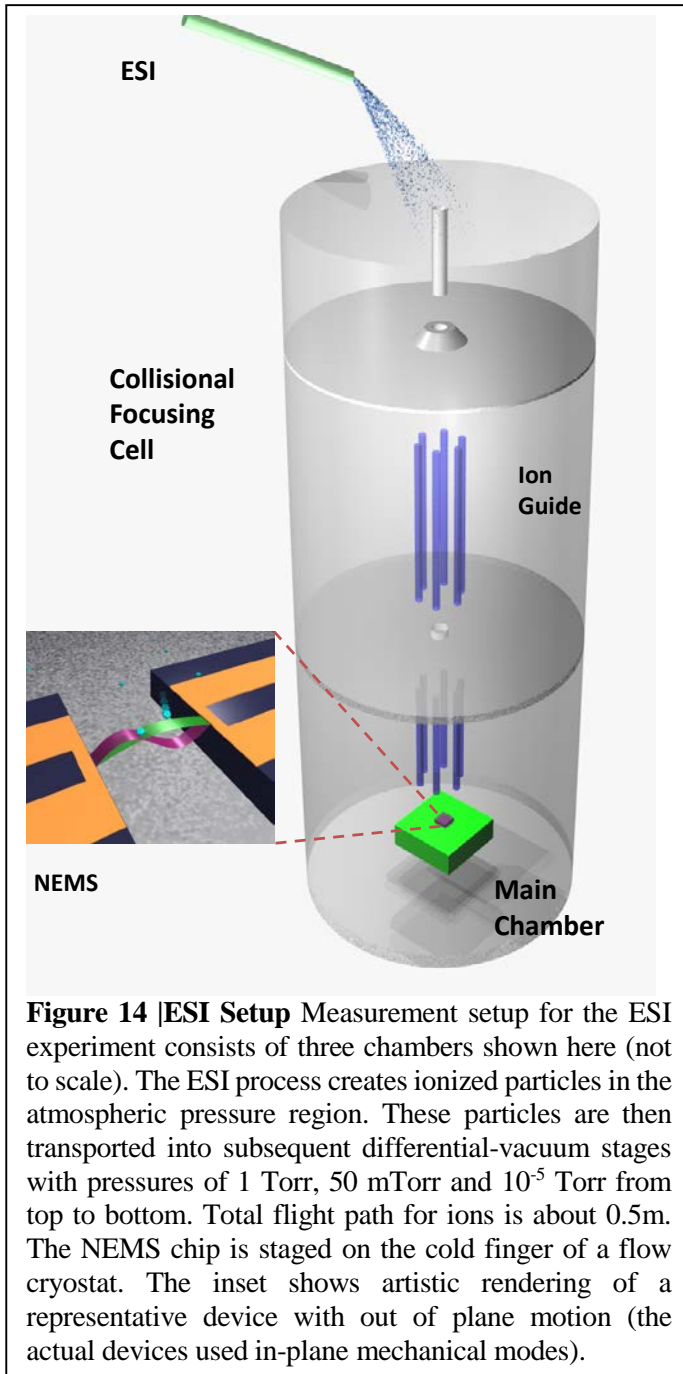


**Figure 13 | PLL Circuit diagram.** The circuit used for the actuation and the readout of the NEMS device. In the diagram, PS = power splitter/combiner, 180 deg. PS = power splitter with 180 degree phase offset, LPF = low pass filter, in = input port to lock-in amplifier, ref= reference port of lock-in amplifier. The bias and drive oscillators are commercial frequency generators. The feedback loop ( $H_\infty$ ) is in blue. The signal from the lock-in amplifiers is read by a computer which, via a corrector calculation, sends a feedback signal to the bias and drive function generators

In this manner, the computer controlled the instruments without being connected to the RF signals that are sent to the device. The GPIB interface, however, did limit the overall loop time to hundreds of milliseconds.

The device employed for these experiments was fabricated at CEA-



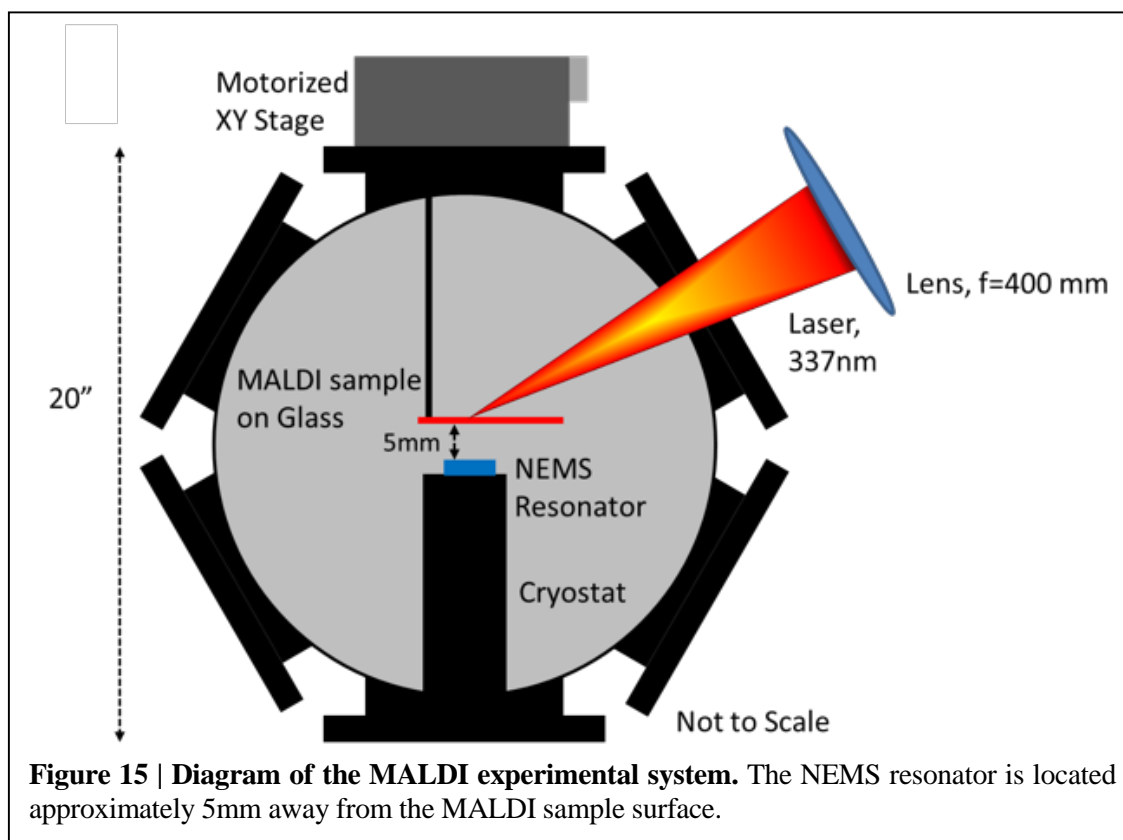
LETI/Minattec in Grenoble, France, using similar procedures as described in [29]. Recent work on large-scale integration of NEMS has been described in [30].

The Allan deviation characterizing the frequency fluctuations of the first NEMS mode was  $\sigma_A^{(1)} \sim 8 \times 10^{-8}$ , and of the second mode was  $\sigma_A^{(2)} \sim 1 \times 10^{-7}$  at the chosen phase-locked loop (PLL) response time of  $\tau_R \sim 500$  milliseconds unless noted otherwise. Current third-generation instrumentation, not yet deployed for NEMS-MS, is capable of sub-millisecond time resolution [31]. The measured noise correlation between the modes was  $\sim 0.3$ . Figure 12b shows a snapshot of two-mode PLL data obtained during electrospray ionization of IgM antibodies. Time-

correlated, quasi-instantaneous frequency jumps of different heights in the two modes clearly demonstrate the ability to resolve discrete adsorption events from individual molecules or nanoparticles accreting onto the NEMS resonator.

The NEMS-MS experiments employing electrospray ionization (ESI) were carried out on a table-top vacuum system equipped with a flow cryostat (shown diagrammatically in Figure 14). The flow cryostat was used to cool down a sample stage within a high vacuum chamber on which the NEMS resonator was mounted. The setup consisted of three differentially-pumped chambers, an electrospray ionization system (ESI) and a hexapole ion guide. The ESI process is a well-established technique to create charged particles from solutions [32, 33].

The ESI experiments with IgM antibodies were carried out by injecting solution into a needle (20  $\mu\text{m}$  diameter, Picotip Emitter, New Objective) that is biased at 4 kV. This large voltage causes the emission of charged microdroplets, which subsequently undergo cycles of evaporation and Coulombic fission, until individual ionized particles emerge in the gas phase. These ions are transported into the first stage of the vacuum system by hydrodynamic flow and electrostatic focusing. Once they have entered into the vacuum system, the particles travel through a long capillary toward



the first stage of the vacuum chamber. At the end of the tube, the incoming gas expands into a low vacuum region where it is supersonically accelerated. The ions are then sampled by a skimmer structure to obtain a collimated molecular/ionic beam. The larger particles in this molecular beam are slowed down in the second chamber (at 50 mTorr) through collisions with the background atoms. This decelerated beam is focused through the use of hexapole ion guides to the third chamber (main chamber) where the NEMS device is placed. These hexapole guides were driven by alternating RF signals with 350-500 kHz frequencies and 300-360V amplitudes.

Human IgM solution was purchased from Sigma-Aldrich and buffer exchanged to 200mM aqueous ammonium acetate, with a final antibody concentration of approximately 1 mg/ml. The NEMS device was kept at the highest vacuum chamber of a three-stage differential pumping setup, with a base pressure of  $10^{-5}$  Torr before cryo-pumping takes place. The NEMS device was cooled to 140K for the Human IgM experiments. Cooling the NEMS device in both the ESI and MALDI setups was done to prevent captured particles from rapidly desorbing from the device surface.

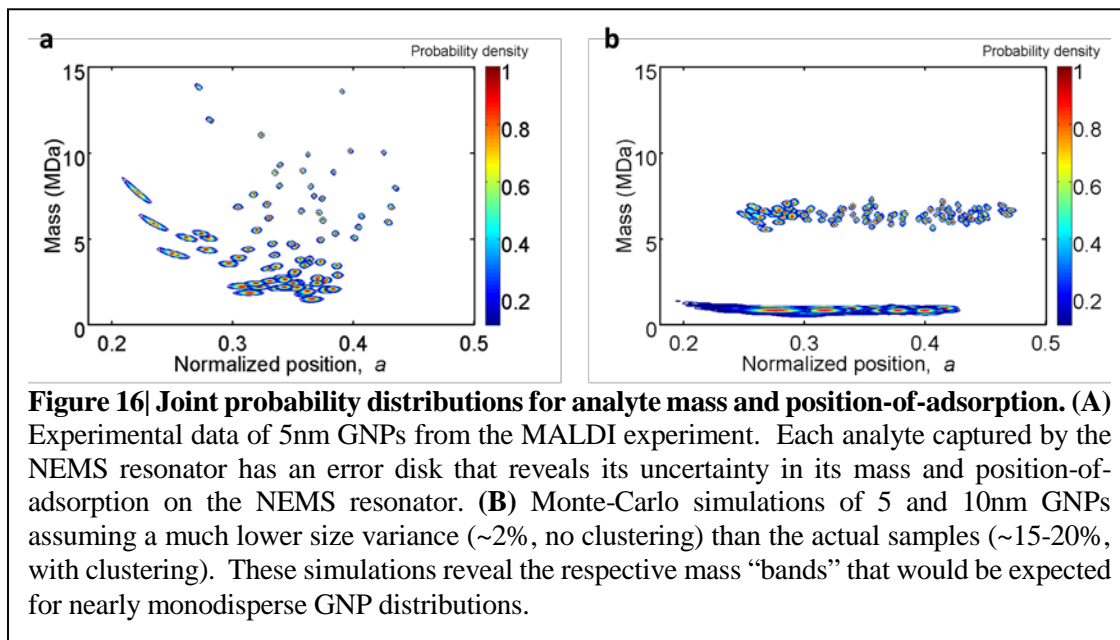
NEMS-MS experiments involving sample introduction by MALDI were carried out within a table-top, UHV capable apparatus depicted in Figure 15. A UHV chamber (Kurt Lesker) was equipped with a flow cryostat (Janis) to cool down with liquid Nitrogen to 80K, a sample stage on which the NEMS resonator was mounted. The NEMS resonator was placed near the chamber center. The MALDI sample plate was positioned approximately 5mm away from the NEMS resonator on a computer controlled x,y-translation stage (Kurt Lesker).

In general, the MALDI process relies on a compound, termed the matrix, which is used to efficiently absorb laser light and become ionized. The matrix is mixed with the analyte so that when the matrix absorbs the laser light and is ionized, it in turn induces ionization in the analyte, bursting into a plume promoting both species into the gas phase [34]. This study examines GNPs (5 and 10nm diameter, Sigma Aldrich), which, by themselves, act as matrix [35].

Colloidal GNPs with nominal diameters of 5-nm (mean diameter = 5.1nm, variance = 19%) and 10-nm (mean diameter = 10.7nm, variance = 10%) were purchased from Sigma-Aldrich. The MALDI sample plates were prepared by washing the stock colloid solutions in water and, using a centrifuge, concentrating the solutions to  $\sim 5 \times 10^{14}$  particles/ml and  $1 \times 10^{14}$  particle/ml for the 5 and 10nm GNP samples, respectively. The glycerol samples were prepared by adding glycerol (Sigma-Aldrich) at 10% concentration to the 5nm GNP solution prior to drying on the Pyrex sample plate. For each sample, 38 $\mu$ l of solution was drip-dried onto 3mm diameter spots on a Pyrex sample plate to maximize particle surface density to obtain maximal flux from the MALDI process.

For an experimental session, the chamber was pumped down to  $\sim 1 \times 10^{-9}$  Torr, and the NEMS device was cooled to  $\sim 80$ K. The MALDI plate was irradiated with laser pulses (337nm, 176 $\mu$ J/pulse, 3.5ns pulse width, Stanford Research Systems model NL100) at a pulse rate of 1Hz. A 400 mm lens (Thorlabs) focused the laser light (Figure 15). The spot on the sample was measured to be  $\sim 50 \times 100$   $\mu\text{m}^2$  by irradiation tracks left upon a separate thermally-evaporated gold sample. The MALDI sample plate was moved relative to the laser spot using the x-y stage. Particles emitted in the MALDI plume then accreted upon the NEMS resonator. No ionization optics were used; the NEMS resonator collected both positive and negative ions, as well as neutrals, from the MALDI plume.

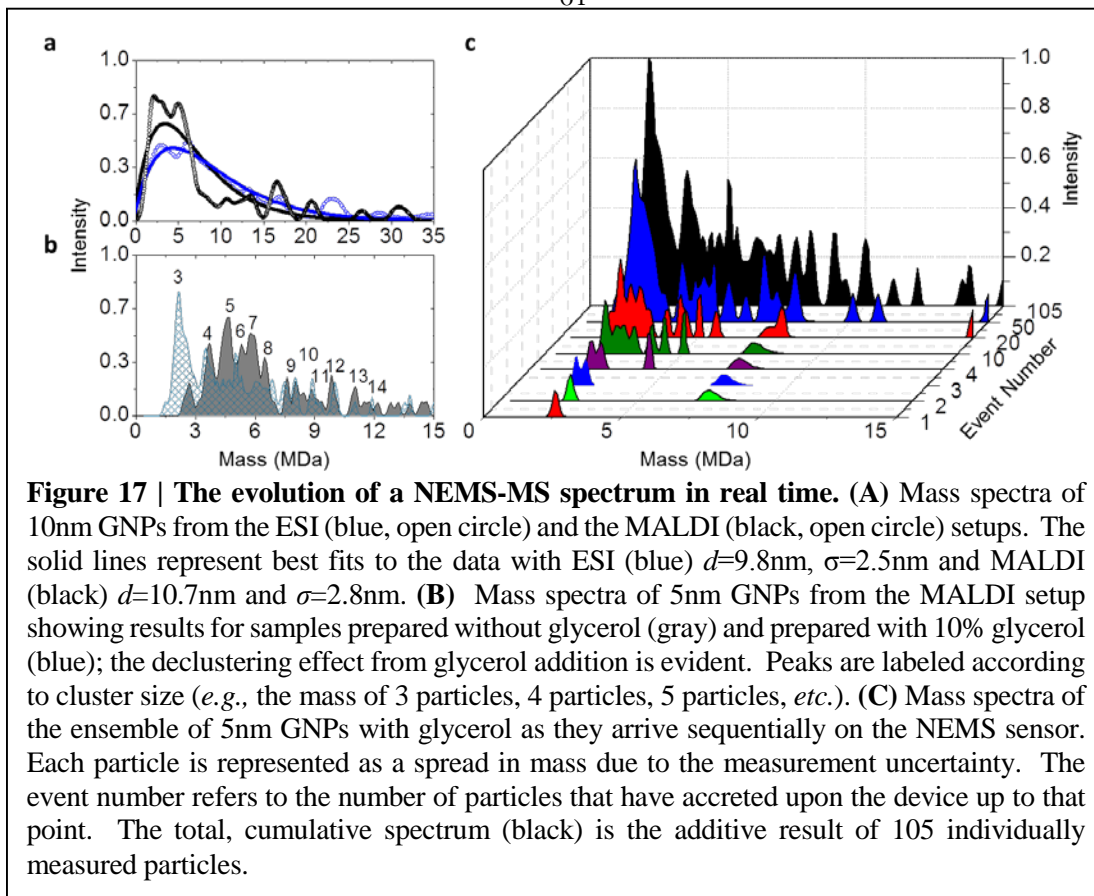
There are important considerations to be taken into account when contrasting an ESI-based versus MALDI-based NEMS-MS system. The basis of ESI consists of converting the analytes in a solvent into ionized species in the gas phase. This is accomplished by introducing the solution into a narrow needle kept at high voltage, so as to induce Taylor instability at the tip of the liquid and form a spray with charged droplets. These charged droplets then experience cycles of rapid evaporation and Coulombic fission until all the solvent is evaporated and ionized analyte species are formed in the gas phase. In contrast, MALDI involves samples in the solid phase, with an external energy source (a laser) that – through absorption by a matrix chemical premixed with the analyte – both promotes the analytes to vapor phase and ionizes them. The largest difference in these two techniques is the ionization state of the analytes. ESI typically forms analyte ions with much higher charge states than does MALDI [36]. For the purposes of NEMS-MS, this difference in charge states is immaterial. The two most important differences regarding NEMS-based MS are: first, in ESI, transport of analytes to the NEMS sensor requires guiding by ion optics. In MALDI, the desorbed analytes have sufficient kinetic energy to reach the nearby sensor without any ion optics. This allows for smaller, simpler experimental systems. Second, NEMS devices suffer larger environmental noise in ESI



Systems. With an ESI injection system, by necessity, there are multiple stages of differential pumping to separate the NEMS device from the analyte solution, which is at atmospheric pressure. Despite these precautions, this still generally leads to higher pressures in the device region that contribute to frequency drift and noise in the NEMS device. This is contrasted with a MALDI-based system where the solid phase analytes are introduced in a vacuum chamber that, after introduction, requires no access to ambient conditions, and thus allows for lower pressure in the device region. Finally, MALDI techniques require extensive sample preparation beforehand, especially to avoid bunching of analytes when they are desorbed by the laser. In comparison, ESI pulls apart analytes leading to, in general, less tendency for bunching or clumping of large species. In traditional mass spectrometry, spectra of the same material with the two different ionization schemes would in general be different due to the different charge states of the molecules produced. However, NEMS based mass spectrometry is sensitive to only the inertial mass of the molecule and thus produces nominally the same mass spectra irrespective of the ionization scheme used, as shown in Figure 17a.

### **3.4 Results: gold nanoparticles**

As mentioned above, when particles land on the NEMS device they produce simultaneous frequency jumps in both of the continuously tracked modes that are subsequently used to determine the mass and position of each molecule/nanoparticle by mapping the  $(\delta f_1/f_1, \delta f_2/f_2)$  pairs onto the  $(dm/M, a)$  plane [1, 2]. Figure 16a shows the mass and position of each adsorbing particle, and their respective uncertainties, for the experiment where 5nm GNPs were delivered onto the NEMS mass sensor via MALDI. The mass spectrum is obtained by integrating the two-dimensional probability density function data along the position coordinate. (Similarly, a position spectrum can be obtained by integrating along the mass coordinate. Chapter four discusses important applications of the position data.) The GNPs, as is usual in typical experimental samples, are known to have a

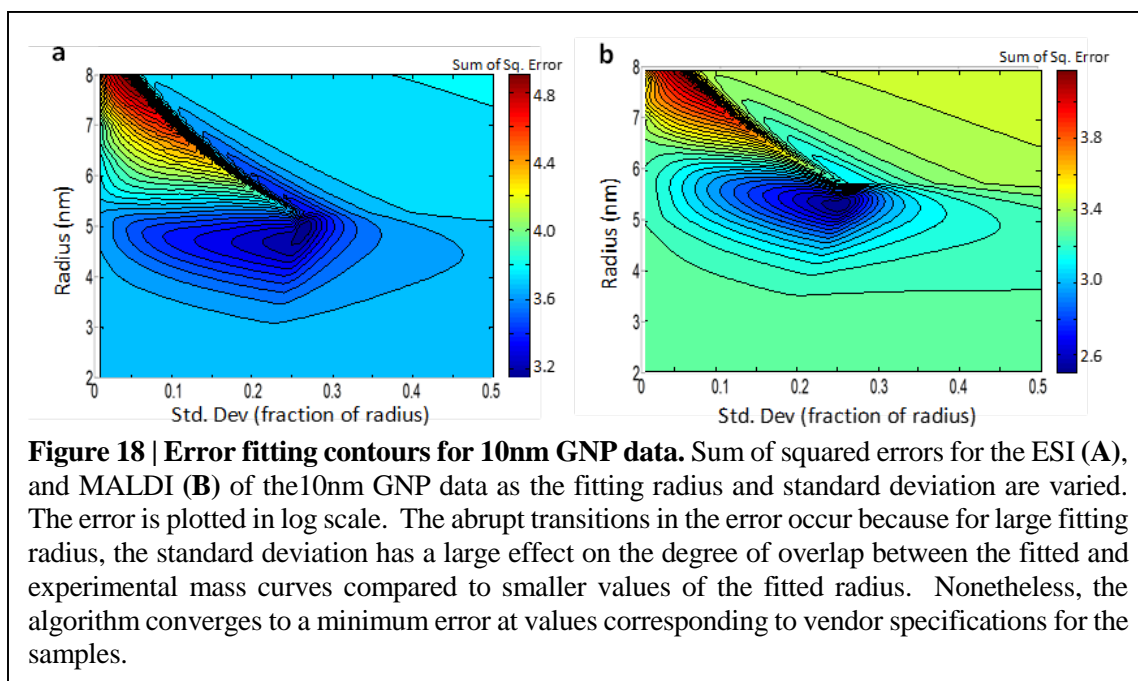


large variance in radius (Sigma Aldrich); this translates into the very large observed mass spread ( $m \sim r^3$ ). If the GNPs were relatively monodisperse, the data would appear as relatively narrow bands along the mass axis. This kind of behavior is well modeled by Monte-Carlo simulations of 5 and 10 nm GNPs –assuming low size variance and no clustering (Figure 16b).

Note that particles (or molecules) with smaller masses will produce smaller relative frequency shifts and, in the presence of a fixed amount of frequency noise, this will appear as a larger position uncertainty. A somewhat counterintuitive feature of these spectra is the evident decrease in the position uncertainty for heavier species while the mass uncertainty remains constant. This originates from the fact that the mass resolution depends on the minimum resolvable frequency shifts – which, again, remain constant due to the frequency noise, regardless of the magnitude of the actual shifts from the arriving analytes. On the other hand, position resolution depends on the minimum

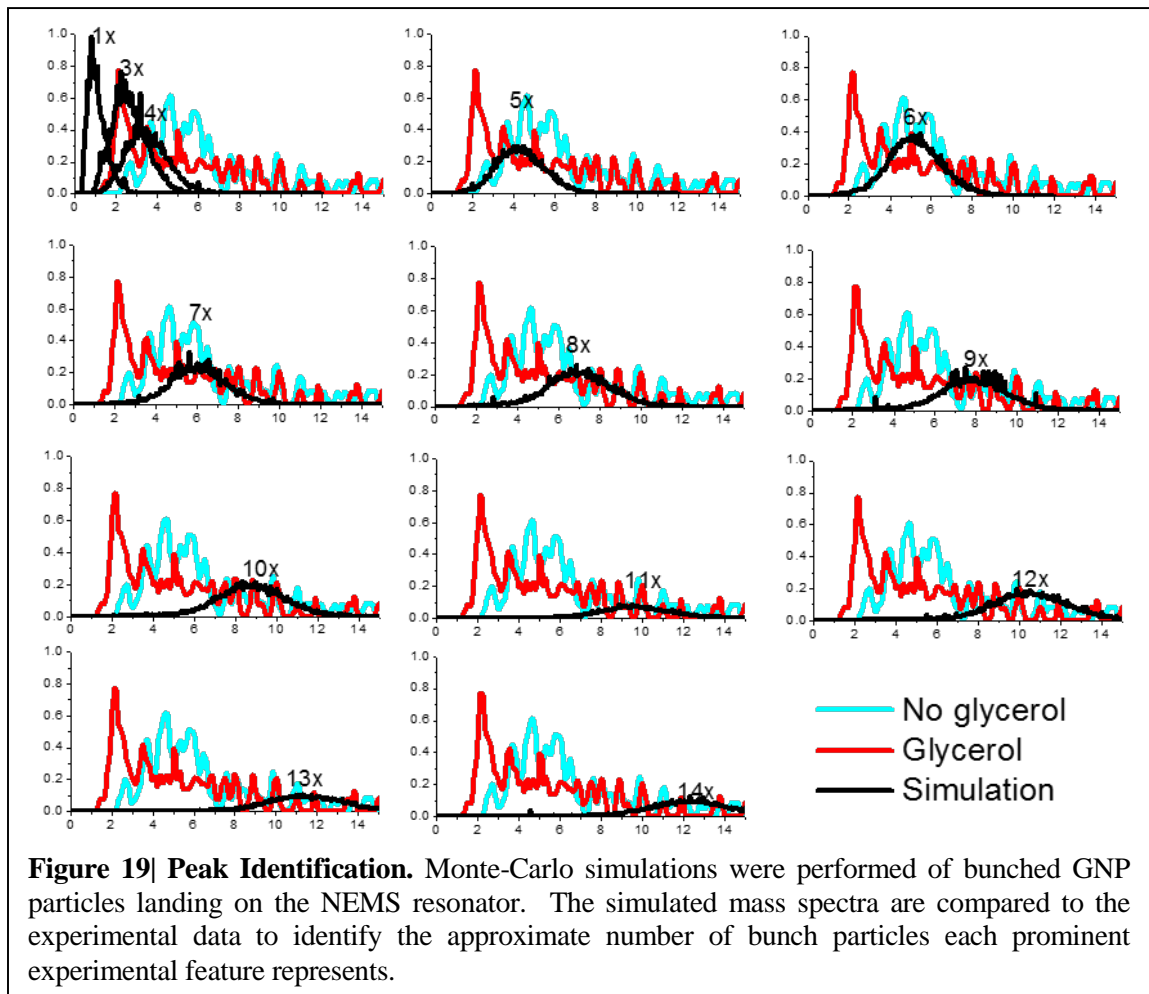
resolvable angle in the  $(\delta f_1/f_1, \delta f_2/f_2)$  plane, and this improves as the magnitude of the frequency shifts become larger. This effect is further described in the supplementary information of [1]. The number of events observed near the center of the beam is reduced because the second mode has a node at the center, and therefore particles landing in this region produce jumps below the noise level.

Measured mass spectra of 10nm GNPs are shown in Figure 17a for the data acquired from the ESI setup (black circles) and from the MALDI setup (blue circles). The GNP data from the ESI setup was acquired exclusively by Dr. Hanay prior to my efforts and is here presented for comparative analysis. This ESI GNP data had a mass resolution of 100kDa (compared to 50kDa for the MALDI data), details the ESI GNP data acquisition are found in [1]. In order to more easily compare with the ESI data, the data for the MALDI curve shown here was analyzed with the same experimental mass resolution that was achieved with the ESI setup for 10nm GNPs. Also shown are the best-fit curves for each data set (ESI, solid black; MALDI, solid blue). For the ESI data, the best fit yielded a diameter of 9.8nm and standard deviation of 2.5nm, while the data using MALDI yielded a diameter



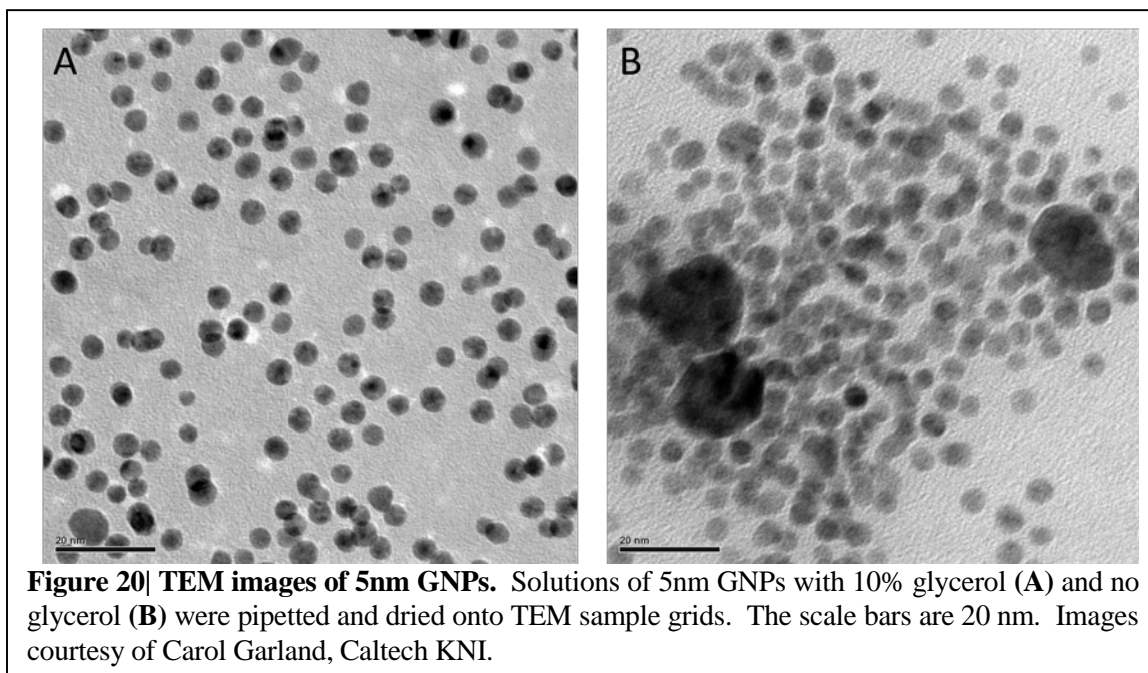
of 10.7nm and a standard deviation of 2.8nm. These values are within the experimental deviation of the vendor specifications for the GNPs.

The least-squares fitting used in Figure 17a was performed between the experimental data and mass histograms of theoretical nanoparticle distributions as the particle radius and standard deviation (assuming Gaussian size distribution) were varied. Figure 18 shows the error contours (log



scale) with the radius in nm and the standard deviation as a fraction of the radius. As seen from the contour graphs, the minimum error is achieved for the ESI (MALDI) setups for radius = 4.90 (5.35) nm and standard deviation = 1.25 (1.4) nm.

These 10nm GNPS measurements are complemented with MALDI-based measurements of 5nm GNPs. In these experiments two types of MALDI plates were prepared; each containing 5nm GNPs, but differing in whether glycerol was added as a separating agent (see section 3.3, above). Previous studies have demonstrated that clustering effects typically exhibited by metallic nanoparticles can be mitigated by the addition of various separating agents [35, 37-39]. Figure 17b shows two distinct mass spectra for the two 5nm GNP samples. A clear reduction in GNP clustering is observed with the use of glycerol. Monte Carlo simulations of 5nm GNPs landing on the NEMS were performed to analyze the clustering effect and enable peak identification in Figure 17b. The simulation-produced frequency jumps were then analyzed in the same way as the experimental data. In the simulations, the bunched particles had a total mass equal to the addition of some integer number of individual 5nm GNPs, each drawn from a size distribution based on the specifications of the vendor (Sigma Aldrich, mean diameter = 5.1nm, variance = 19% of average size). The simulated mass spectra were then compared with the experimental data and the center of the simulated peaks was found to coincide with the position of the various peaks in the data. Figure 19 shows panels of the



same experimental data overlaid with the simulated spectra to show the matching between the peak locations.

The presence of GNP bunching and the utility of glycerol as a separating agent is further confirmed with TEM pictures shown in Figure 20. Figure 20a shows a TEM image of 5nm GNPs pipetted from the 10% glycerol solution, while Figure 20b shows a similar image from a 5nm GNP sample without glycerol in solution. The GNPs in Figure 20a show a much higher degree of particle-particle separation than is apparent in Figure 20b. Moreover, Figure 20b reveals the existence of significantly larger GNP bunches than are evident in Figure 20a. Though other pictures from the other positions of the glycerol sample grid exhibited similarly large structures, a visual inspection revealed a clear preponderance toward GNP bunching for the grid with the no-glycerol sample. The images were taken courtesy of Carol Garland, Caltech KNI technical staff.

The process of constructing the cumulative mass spectra from the individual particle measurements is exhibited in Figure 17c, which shows the accumulated mass spectra, as acquired particle-by-particle, for the 5-nm GNPs (with glycerol). Each event in the current set of measurements provides the mass of the adsorbed analyte. This contrasts with previous measurements [17, 18], wherein each data point was, at best, part of a statistical ensemble – itself one bit of information convolved with the position dependence of single-mode NEMS response. Here, as is graphically displayed in Figures 17c and 21a, spectra can now be built up, particle-by-particle, as each analyte arrives. With this advance it is now possible to weigh individual molecules in real time,

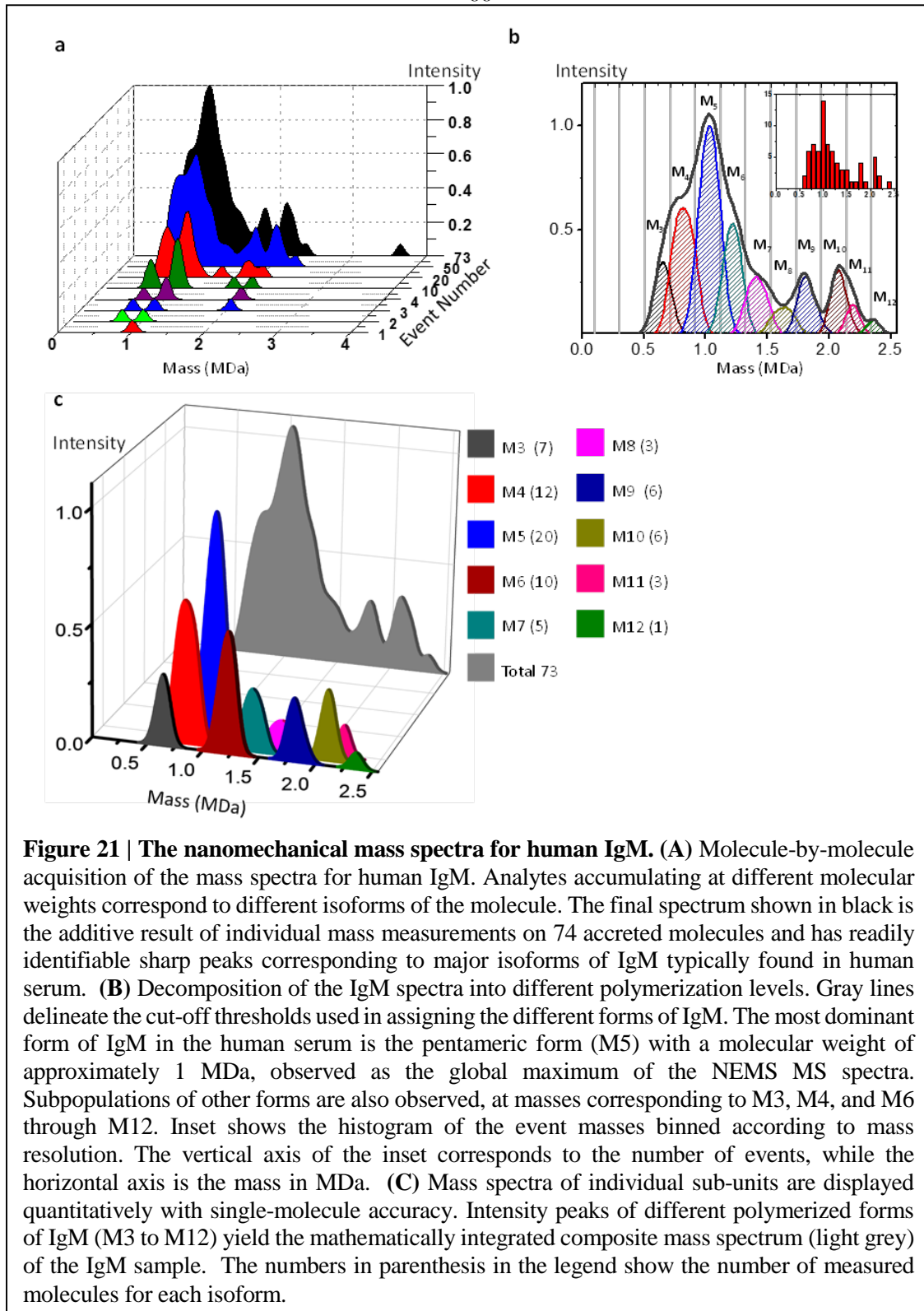


**Figure 21 | The nanomechanical mass spectra for human IgM. (A)** Molecule-by-molecule acquisition of the mass spectra for human IgM. Analytes accumulating at different molecular weights correspond to different isoforms of the molecule. The final spectrum shown in black is the additive result of individual mass measurements on 74 accreted molecules and has readily identifiable sharp peaks corresponding to major isoforms of IgM typically found in human serum. **(B)** Decomposition of the IgM spectra into different polymerization levels. Gray lines delineate the cut-off thresholds used in assigning the different forms of IgM. The most dominant form of IgM in the human serum is the pentameric form (M5) with a molecular weight of approximately 1 MDa, observed as the global maximum of the NEMS MS spectra. Subpopulations of other forms are also observed, at masses corresponding to M3, M4, and M6 through M12. Inset shows the histogram of the event masses binned according to mass resolution. The vertical axis of the inset corresponds to the number of events, while the horizontal axis is the mass in MDa. **(C)** Mass spectra of individual sub-units are displayed quantitatively with single-molecule accuracy. Intensity peaks of different polymerized forms of IgM (M3 to M12) yield the mathematically integrated composite mass spectrum (light grey) of the IgM sample. The numbers in parenthesis in the legend show the number of measured molecules for each isoform.

without the need to first collect an ensemble of identical particles. This enables straightforward

analysis of complex mixtures, as exemplified in Figure 21a, and represents the first time isolated biomolecules have been weighed by a nanomechanical device.

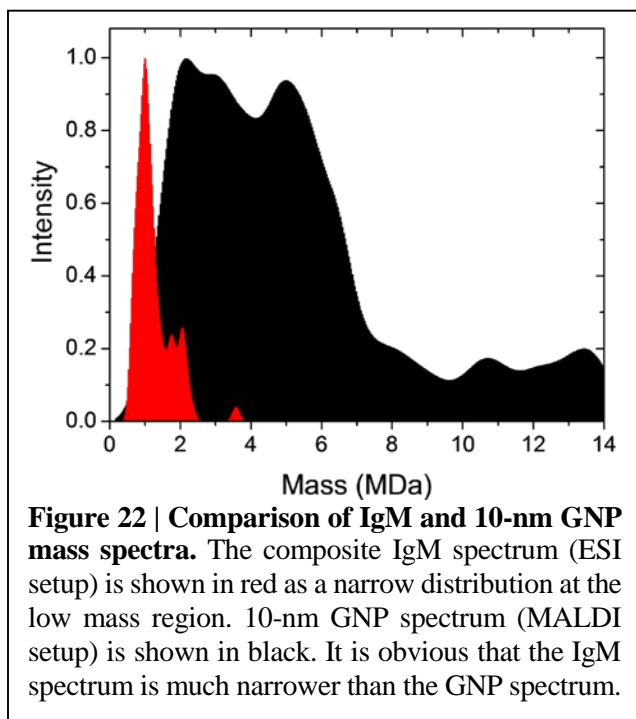
### **3.5 Results: human IgM antibody measurements**

To further demonstrate the utility of NEMS based mass spectrometry for biological species, single-molecule NEMS-MS spectra for human IgM antibodies using ESI injection were obtained. In serum, IgM is typically found in macromolecular complexes that are assembled by the immune system. The presently-known biologically-active isoforms in serum can be tetrameric, pentameric, hexameric, or dipentameric assemblies of identical  $\sim 190$  kDa sub-units [40-43]. For the prevalent pentamer isoform, an additional small protein (the J chain) helps link the assemblage and contributes  $\sim 15$  kDa to the total  $\sim 960$  kDa mass of the complex [44, 45]. The overall mass spectrum, a composite curve accumulated from 74 single particle spectra, is shown in Figure 21a. The individual pentameric IgM complex (the highest intensity peak) is clearly visible at  $1.03 \pm 0.05$  MDa, as is a dimerized pentameric complex (“dipentamer”) at  $2.09 \pm 0.05$  MDa – a ratio very close to two, as expected. These measured values are very close to the anticipated values 0.96 MDa and 1.92 MDa [45], which is remarkable considering the fact that we report mass values without any calibration, other than the nominal dimensions of the mass sensor based on the fabrication mask.

The apparent smoothness of the mass spectra for the individual isoforms of Figure 21 arises from the fact that *each* single-particle/molecule event can be resolved with its own uncertainty level. Specifically, the mass spectra in Figures 17 and 21 represent information acquired from sets of 105 and 74 single-particle/molecule adsorption events, respectively. Each of these events can be represented in the mass-position plane as a continuous probability distribution. Subsequently, mass spectra were obtained for each event by projecting the individual distributions onto the mass plane. For each particle/molecule accreted, this yields a smooth Gaussian-like curve for its mass spectrum,

with a width dependent on the specific mass and position of the particle. The cumulative mass spectra are then Gaussian-like mass distributions averaged by like IgM isoforms, as in the foreground of Figure 21c, or added overall to generate a composite spectrum, as in the background grey curve of Figure 21c. Alternatively, one can report the center of the mass distribution (as done in the inset of Figure 21b), but then one loses the unique position and mass uncertainty information for each particle that is obtained with the uncertainty analysis formalism supplied by multimode theory.

Figures 21b and 21c illustrate the remarkable power of single-molecule NEMS-MS to resolve spectra. Here, the well-resolved, individual single-unit peaks are the experimental data – and the overarching grey curve is the numerical integral of the data. This is a surprising reversal of the traditional situation, and it completely eliminates typical ambiguities in identifying and explaining the origin of spectral features, such as the apparent shoulder at 0.82 MDa in the composite intensity curve. Here, this feature is unambiguously seen to arise from the presence of precisely twelve accreted macromolecular complexes. Each one is a tetramer of IgM, which individually registered on the NEMS mass sensor and was separately measured as part of the ensemble of 74 molecules collected during this experiment. The legend in Figure 21c provides the number of molecules collected for each of the sub-unit peaks. To identify the different IgM isoforms with the single-molecule measurements, equidistant thresholds were used between the expected mass values of adjacent species, shown as gray lines of Figure 21b. Due to mass measurement error (0.05 MDa), there is a small probability for some events to be misidentified when the noise level during that



particular event happens to exceed the  $2\sigma$  noise threshold separating two distinct species. A statistical analysis on the data ensemble [1] suggests that less than 7% of the events, that is, only ~5 of the 74 collected molecules might be misidentified.

This experiment reveals a sequence of IgM isoforms from trimer (N=3) up to dodecamer (N=12) within the mass range investigated; these can

originate from both physiological and experimental factors. Fragmentation and nonspecific reassembly of large macromolecular species is expected to occur in ESI systems [7, 46]. However, it is known that IgM can also be selectively assembled by the lymphatic system into pentamer and hexamer complexes as part of an immunologically-driven response to antigens [40, 41]. NEMS-MS, unlike conventional MS, does not require the charging of analytes to achieve its selectivity. The ability to use *neutral injection* methods that capitalize on the strengths of NEMS-MS will, in the future, allow direct determination for the efficiency of such immunological processes, and allow the monitoring of them in real time and, for example, in response to potential therapies – without the confounding source of isoforms from charge-driven fragmentation.

It is observed that in both the IgM and GNP experiments, the mass spectra are distributed across a larger range than if the species were truly monodisperse. It is nonetheless instructive, however, that the IgM mass spectrum, even with the presence of various isoforms, is much more narrowly concentrated than the GNP mass spectrum. Figure 22 displays these two mass spectra,

recorded separately, overlaid on the same plot. As is apparent from Figure 22, the IgM mass spectrum is much more narrowly concentrated than the 10-nm GNPs, and these two species would be distinguishable if measured from the same sample.

NEMS-MS systems yield very high resolving powers in the large mass range (>500 kDa), since NEMS mass resolution remains constant over the entire mass range. The present experiments provide the first experimental validation of real-time NEMS mass spectrometry, and demonstrate the potential of NEMS mass sensors for performing mass spectrometry on large macromolecules and nanoparticles with masses deep into the MDa range.

### **3.6 Conclusion**

This work demonstrates mass spectrometry using nanomechanical devices wherein the masses of individual protein macromolecules arriving at the device are measured in real time. A MALDI-NEMS-MS vacuum apparatus was constructed and used to obtain the cumulative mass spectra of samples of 5 and 10 nm GNPs built up, particle-by-particle, from the mass spectra of individual GNPs. Additionally, an existing ESI-NEMS-MS vacuum apparatus was modified, rebuilt, and operated to obtain the mass spectra of biomolecules – human IgM antibodies – that were similarly assembled from the individual mass measurements of each protein molecule. These experiments clearly establish the utility of NEMS for mass spectrometry of large biomolecules and, more specifically, for native mass spectrometry. Improving the mass resolution of top-down fabricated nanomechanical devices by only one or two decades – which is attainable in the near term – offers exciting prospects for useful applications in bacterial identification, native mass spectrometry, and structural identification of large macromolecules. Recent work has dramatically improved the mass resolution of bottom-up fabricated NEMS devices [15-17, 20], and now offers realistic potential for ultimately creating NEMS-MS spectrometers with resolution down to a few Daltons. However, much

work remains: bottom-up NEMS devices and approaches have yet to demonstrate mass measurements of individual molecules, and questions remain about their compatibility with large scale integration. Ultimately, however, the ability to use VLSI and CMOS-compatible NEMS with devices providing single Dalton sensitivity will enable the possibility of measuring millions of proteins, in real-time, from a small discrete sample – like a single cell – while retaining single-protein precision over the full range of biological interest.

### 3.7 Bibliography

1. Hanay, M.S., et al., *Single-protein nanomechanical mass spectrometry in real time*. Nature Nanotechnology, 2012. **7**(9): p. 602-608.
2. Hanay, M.S., *Towards Single-Molecule Nanomechanical Mass Spectrometry*, in *Physics*. 2011, California Institute of Technology.
3. Andersson, C.-O., *Mass Spectrometric Studies on Amino Acid and Peptide Derivatives*. Acta Chem. Scand., 1958. **12**(6): p. 1353.
4. Beynon, J.H., *The use of the mass spectrometer for the identification of organic compounds*. Microchim. Acta, 1956. **44**(1-3): p. 437.
5. Domon, B. and R. Aebersold, *Mass spectrometry and protein analysis*. Science, 2006. **312**(5771): p. 212-217.
6. Benesch, J.L.P. and C.V. Robinson, *Mass spectrometry of macromolecular assemblies: preservation and dissociation*. Current Opinion in Structural Biology, 2006. **16**(2): p. 245-251.
7. Robinson, C.V., et al., *Protein complexes in the gas phase: Technology for structural genomics and proteomics*. Chemical Reviews, 2007. **107**(8): p. 3544-3567.
8. Warscheid, B., S. Oeljeklaus, and H.E. Meyer, *New dimensions in the study of protein complexes using quantitative mass spectrometry*. Febs Letters, 2009. **583**(11): p. 1674-1683.
9. Duijn, E.v., et al., *Chaperonin Complexes Monitored by Ion Mobility Mass Spectrometry*. Journal of the American Chemical Society, 2009. **131**(4): p. 1452-1459.
10. Heck, A.J.R., *Native mass spectrometry: a bridge between interactomics and structural biology*. Nature Methods, 2008. **5**(11): p. 927-933.
11. Ekinci, K.L., X.M.H. Huang, and M.L. Roukes, *Ultrasensitive nanoelectromechanical mass detection*. Applied Physics Letters, 2004. **84**(22): p. 4469-4471.
12. Ilic, B., et al., *Attogram detection using nanoelectromechanical oscillators*. Journal of Applied Physics, 2004. **95**(7): p. 3694-3703.
13. Yang, Y.T., et al., *Zeptogram-Scale Nanomechanical Mass Sensing*. Nano Letters, 2006. **6**(4): p. 583-586.
14. Li, M., H.X. Tang, and M.L. Roukes, *Ultra-sensitive NEMS-based cantilevers for sensing, scanned probe and very high-frequency applications*. Nat Nano, 2007. **2**(2): p. 114-120.
15. Chiu, H.-Y., et al., *Atomic-Scale Mass Sensing Using Carbon Nanotube Resonators*. Nano Letters, 2008. **8**(12): p. 4342-4346.

16. Lassagne, B., et al., *Ultrasensitive Mass Sensing with a Nanotube Electromechanical Resonator*. Nano Letters, 2008. **8**(11): p. 3735-3738.
17. Jensen, K., K. Kim, and A. Zettl, *An atomic-resolution nanomechanical mass sensor*. Nature Nanotechnology, 2008. **3**(9): p. 533-537.
18. Naik, A.K., et al., *Towards single-molecule nanomechanical mass spectrometry*. Nature Nanotechnology, 2009. **4**(7): p. 445-450.
19. Ekinici, K.L., Y.T. Yang, and M.L. Roukes, *Ultimate limits to inertial mass sensing based upon nanoelectromechanical systems*. Journal of Applied Physics, 2004. **95**(5): p. 2682-2689.
20. Chaste, J., et al., *A nanomechanical mass sensor with yoctogram resolution*. Nat Nanotechnol, 2012. **7**(5): p. 301-4.
21. Siuzdak, G., *The Expanding Role of Mass Spectrometry in Biotechnology*. 2003, San Diego: MCC Press.
22. Hanay, M.S. and M.L. Roukes, *Multimode Detection Schemes for NEMS-Based Mass Spectrometry*. 2005, Caltech Disclosure, CIT-4423-P.
23. Roukes, M.L., A.K. Naik, and M.S. Hanay, *Single Molecule Mass Spectroscopy Enabled by Nanoelectromechanical Systems*, U.S.P. Office, Editor. 2009, California Institute of Technology: USA.
24. Dohn, S., et al., *Mass and position determination of attached particles on cantilever based mass sensors*. Review of Scientific Instruments, 2007. **78**(10): p. 103303.
25. Gil-Santos, E., et al., *Nanomechanical mass sensing and stiffness spectrometry based on two-dimensional vibrations of resonant nanowires*. Nat Nano, 2010. **5**(9): p. 641-645.
26. Schmid, S., S. Dohn, and A. Boisen, *Real-time particle mass spectrometry based on resonant micro strings*. Sensors (Basel), 2010. **10**(9): p. 8092-100.
27. Kharrat, C., E. Colinet, and A. Voda. *Loop shaping control for PLL-based mechanical resonance tracking in NEMS resonant mass sensors*. in *Sensors, 2008 IEEE*. 2008.
28. Bargatin, I., et al., *Sensitive detection of nanomechanical motion using piezoresistive signal downmixing*. Applied Physics Letters, 2005. **86**(13).
29. Mile, E., et al., *In-plane nanoelectromechanical resonators based on silicon nanowire piezoresistive detection*. Nanotechnology, 2010. **21**(16).
30. Bargatin, I., et al., *Large-Scale Integration of Nanoelectromechanical Systems for Gas Sensing Applications*. Nano Letters, 2012. **12**(3): p. 1269-1274.
31. Colinet, E., et al., (*Unpublished Work*).
32. Dole, M., L.L. Mack, and R.L. Hines, *Molecular Beams of Macroions*. Journal of Chemical Physics, 1968. **49**(5): p. 2240-&.
33. Fenn, J.B., et al., *Electrospray Ionization for Mass-Spectrometry of Large Biomolecules*. Science, 1989. **246**(4926): p. 64-71.
34. Karas, M., D. Bachmann, and F. Hillenkamp, *Influence of the Wavelength in High-Irradiance Ultraviolet-Laser Desorption Mass-Spectrometry of Organic-Molecules*. Analytical Chemistry, 1985. **57**(14): p. 2935-2939.
35. Tanaka, K., *The Origin of Macromolecule Ionization by Laser Irradiation (Nobel Lecture)*. Angewandte Chemie International Edition, 2003. **42**(33): p. 3860-3870.
36. Cole, R.B., *Electrospray and MALDI mass spectrometry: fundamentals, instrumentation, practicalities, and biological applications*. 2011: Wiley.
37. Chiang, C.L., M.B. Hsu, and L.B. Lai, *Control of nucleation and growth of gold nanoparticles in AOT/Span80/isooctane mixed reverse micelles*. Journal of Solid State Chemistry, 2004. **177**(11): p. 3891-3895.

38. Kim, B., et al., *Cluster size analysis of two-dimensional order in colloidal gold nanoparticle arrays*. Langmuir, 2004. **20**(21): p. 9360-9365.
39. Westcott, S.L., et al., *Formation and adsorption of clusters of gold nanoparticles onto functionalized silica nanoparticle surfaces*. Langmuir, 1998. **14**(19): p. 5396-5401.
40. Hughey, C.T., et al., *Production of IgM Hexamers by Normal and Autoimmune B Cells: Implications for the Physiologic Role of Hexameric IgM*. The Journal of Immunology, 1998. **161**(8): p. 4091-4097.
41. Collins, C., F.W.L. Tsui, and M.J. Shulman, *Differential activation of human and guinea pig complement by pentameric and hexameric IgM*. European Journal of Immunology, 2002. **32**(6): p. 1802-1810.
42. Azuma, Y., et al., *Recombinant Human Hexamer-Dominant IgM Monoclonal Antibody to Ganglioside GM3 for Treatment of Melanoma*. Clinical Cancer Research, 2007. **13**(9): p. 2745-2750.
43. Lindhagen-Persson, M., et al., *Amyloid- $\beta$  Oligomer Specificity Mediated by the IgM Isotype – Implications for a Specific Protective Mechanism Exerted by Endogenous Auto-Antibodies*. PLoS ONE, 2010. **5**(11): p. e13928.
44. Davis, A.C. and M.J. Shulman, *IgM - molecular requirements for its assembly and function*. Immunology Today, 1989. **10**(4): p. 118-128.
45. Bacher, G., et al., *Charge-reduced nano electrospray ionization combined with differential mobility analysis of peptides, proteins, glycoproteins, noncovalent protein complexes and viruses*. Journal of Mass Spectrometry, 2001. **36**(9): p. 1038-1052.
46. Loo, J.A., et al., *Electrospray Ionization Mass Spectrometry and Ion Mobility Analysis of the 20S Proteasome Complex*. Journal of the American Society for Mass Spectrometry, 2005. **16**(7): p. 998-1008.

## *Chapter 4*

# LIAD-NEMS-MS

### **4.1 Introduction**

In the preceding chapters, successful attempts to desorb and detect gold nanoparticles and unsuccessful attempts utilizing MALDI for protein delivery were presented. The preceding also presented results of my efforts with Dr. Selim Hanay in the Roukes group to rebuild and operate a pre-existing ESI-based NEMS-MS apparatus to measure individual proteins, IgM antibodies. One of the main goals of my research is the successful measurement of proteins by NEMS-MS using laser desorption. This chapter presents successful results in that effort through the implementation of an existing mass spectrometry technique known as laser induced acoustic desorption (LIAD).

A primary motivation for pursuing a laser-based desorption technique for NEMS is to increase the flux rate of particles on the NEMS device. The cross section of the NEMS devices used in this work is  $10\ \mu\text{m} \times 300\ \text{nm}$ . This is a very difficult target in general, but especially so considering limitations in the precision and accuracy with which molecular trajectories (from source to detector) can be controlled. The ESI-NEMS system, in its final incarnation, achieved a data event rate (one event = one particle landing on the NEMS) of  $\sim 1$  event/30 minutes (see chapter three).

Theoretically, this low event rate per device can be improved by increasing the particle flux rate. A limit to increasing the flux rate, however, is the requirement for ESI that the molecules be introduced into the detector from a liquid-based aerosol spray. Because the NEMS device requires a low operating vacuum pressure ( $\sim 10^{-6}$  Torr), a differential pumping vacuum system is necessary to

connect a NEMS detector to an ESI source. Differential pumping in turn requires space and volume between the initial and final stages. This requirement then necessitates the use of ion optics to efficiently guide ionized particles from the inlet stage to the NEMS detector stage.

It is this combination, differential pumping and ionization, which limits the flux rate of the ESI-NEMS system. First, the ionization of proteins is an inefficient process. The theoretical limit of the ESI process (demonstrated in specialized NanoESI systems) is 85%, but common effective sampling efficiencies (ions that are captured by the ion optics in the vacuum phase) are around 5-10% [1]. MALDI can achieve higher ion capture efficiency since the plume droplets do not have to transition from atmosphere to vacuum, but the ionization efficiency is usually lower, with 5% the reported upper limit[1]. Second, physical separation of the NEMS detector from the particle source inherently reduces the flux rate, since any protein ion transportation system has some inefficiencies.

In a laser-based desorption system, a dried analyte film on a substrate is placed in the vacuum chamber and then proteins are ionized by laser pulses. This removes the requirement for a differential pumping system and allows the NEMS detector to be placed in close proximity to the protein source. Additionally, the laser-desorption process provides forward momentum to the protein particles without ion guides. As such, both ionized and neutral particles are ejected as a plume in the direction of the NEMS device. It is these two features, close proximity and independence of ionization, that allow a laser-desorption based NEMS-MS system to achieve higher flux rates than an ESI-NEMS system. Indeed, the flux rate of nearly one event/second achieved in the laser-based NEMS-MS system is an improvement of over two orders of magnitude.

An additional benefit of this dynamic is the suitability of a laser-based NEMS-MS system for so called “native” mass spectrometry (described in more detail below), which seeks to measure large proteins and protein complexes in their native state unaltered by charge effects. Any process

that charges the particles, even if the charging is not used for detection (such as in MALDI-NEMS-MS), can result in charge-induced alterations to the protein complexes.

However, one drawback of a laser-based NEMS-MS system, compared with an ESI-NEMS system, is that the former requires dried samples to be inserted into a vacuum chamber. This eliminates the possibility of operating the mass spectrometer in a continual-flow manner in which proteins from solution are directly introduced and measured. This can be critical for some biological applications which seek to measure dynamic processes in real-time, where the procedure for sample plate preparation can alter the results. Thus, the laser-based NEMS-MS system herein developed is not meant simply to replace the ESI-NEMS system, but to offer a complementary tool for applications of NEMS-based mass spectrometry.

This chapter presents the theory and results of a NEMS-MS system utilizing LIAD for protein desorption and delivery. Implementation of this system required modifying the laser-based system described in chapters two and three to admit a new, more powerful laser and incorporating custom-engineered substrates that interact with the laser to achieve protein desorption. The results showing various protein spectra demonstrate the success of this LIAD-NEMS MS system in detecting and measuring individual protein events. Further improvements to the sample preparation methods are desirable for this system to achieve wider utility in the mass spectrometry field.

Additionally, this chapter explores an unexpected aspect of the system. This LIAD-NEMS MS system relies on multimode theory to convert time-correlated frequency jump pairs into the mass and landing position of individual particles [2]. While the mass data are of primary interest, during the course of experiments and data analysis an interesting feature of the position data was discovered that merits further analysis. As described below, the position data may indicate that the protein particles are moving along the surface of the NEMS device via a known process referred to as the Chladni effect, in which oscillating beam displacements direct surface particles to nodes or antinodes,

depending on the nature of the surface-particle interactions. This hypothesis presently has insufficient data to be confirmed, and further experiments to do this are discussed. The discussion in this chapter is meant only to propose one possible explanation of the position spectra and does not seek to claim definitive proof of such. Nonetheless, the potential of this observation opens new applications for NEMS mass sensing beyond mass spectrometry to the investigation of surface chemistry and surface structural effects on particle species.

## **4.2 Motivation for LIAD**

LIAD was invented by Golovlev and Chen in 1997 as a means to improve the mass resolution of MALDI-type mass spectrometers by reducing the spread of initial particle kinetic energies [3]. LIAD has now found common use in a variety of mass spectrometry applications that require a matrix-free technique. Beyond mass spectrometry, however, laser induced acoustic pulses are used in applications such as electronic surface cleaning [4, 5], and studies of thin film interfacial strengths [6-8]. LIAD is herein employed as a delivery mechanism of individual proteins to the NEMS detector for mass spectrometry. There are several advantages in employing LIAD over other protein delivery techniques: there is no background effect (such as a matrix), it is a neutral technique with no inherent ionization pathway, it has been successful across a wide mass range --from hundreds of Daltons [9-12] to whole cells (tens of teraDaltons) [13, 14] -- and sample preparation is comparatively easy.

As seen in chapters two and three, though MALDI-NEMS is successful for GNP desorption and detection, efforts to measure proteins fail, in part, because the matrix-induced background overwhelms the protein signal. While one can imagine schemes to reduce this background effect by, for example, reducing the matrix surface density or vastly increasing the sample-NEMS distance, a contaminating background might still be present. LIAD is particularly well-suited to single-particle

mass spectrometry since it relies on the deformation of the substrate to eject the particles [3], and not on the chemical potential energy of an additional surface film (as in MALDI or NIMS).

Additionally, there is growing interest in the mass spectrometry community for measuring the mass and structure of large, intact protein complexes, so-called “native” mass spectrometry [15, 16]. Central to the associated techniques (ESI-MS, ion mobility MS) are efforts to minimize the charge states of the complexes in order to better maintain the original or native structure in the gas phase [16]. Conventional mass spectrometry techniques depend on charging of the protein complexes to enable detection. Thus, much effort has been devoted to detecting large complexes with a charge state as close to unity as possible. This, however, places limits on detection efficiency and resolution which are often improved by imparting higher kinetic energy to the individual analytes which, for large complexes, often requires higher charge states. In short, big particles need to be charged highly enough so that they fly fast enough to be detected. A higher charge state, however, can induce alterations to the protein structure.

Until the development of NEMS-MS, there has not been a technique capable of measuring the mass of these intact complexes without requiring some sort of charging. Liquid chromatography (LC) is not a charge-based technique, and is often used for sample separation prior to injection of an ESI-based system. LC can provide mass spectra, but LC-MS only provides mass information indirectly using extrapolations from the interaction time between the analyte molecules and the column beads. As in other techniques, such as laser-particle sizing, mass measurement requires assumptions about particle shape and density. Additionally, the mass resolution of LC-MS is limited for larger mass proteins (above a few hundred kDa). Thus, the optimum technique for measuring large complexes in their native state would be one that does not charge the molecules and provides a direct mass measurement.

LIAD has no inherent charging mechanism [3]. Conventional systems that feature LIAD rely either on the ambient charging of analytes from solution conditions [10] or feature a secondary charging system after desorption [12]. Combining LIAD with a neutral detection mechanism such as NEMS-MS thereby presents a system optimally suited to measuring the mass of large, intact protein complexes without suffering charge-induced fragmentation or deformation effects.

Other background-free, laser-based techniques exist that could be mated with a NEMS detector in a similar ion-optic free mass spectrometer. Desorption ionization on silicon (DIOS) and its successor, nanostructure initiator mass spectrometry (NIMS), both rely on a porous silicon substrate to transfer laser energy to proteins in order to promote desorption without fragmentation (although for NIMS, a thin film of Teflon is applied to the surface that may create a neutral background in NEMS-MS). Though ionization pathways are present, these techniques are worthy of future investigation as to their compatibility with a NEMS-MS system. The substrate preparation, while straightforward, nonetheless requires a dedicated silicon etching setup and recipe perfection [17]. Additionally, DIOS and NIMS may have an upper mass limit of 30kDa, the origin of which is unclear but might be related to the relative sizes of the surface analytes and the silicon pores [18].

### **4.3 LIAD theory**

LIAD is used within the mass spectrometry community as a means for desorbing nonvolatile, thermally labile molecules to yield ejected species with low internal and kinetic energies (compared to traditional MALDI or ESI) [9]. LIAD is based on the absorption (by a material such as a thin metal foil or silicon wafer) of a fast (nanosecond) laser pulse and rapid thermal expansion to produce a bulk acoustic wave (BAW) that, upon reflection at the opposite surface, desorbs pre-deposited surface analytes [3]. It has been used for the desorption and mass spectrometric analysis of whole mammalian

cells and polystyrene microparticles [13], amino acids, peptides and proteins [12], and hydrocarbon mixtures [11], amongst others.

One can construct a simple model to describe the desorption process. Pre-deposited surface analytes will stick to the surface with a certain binding force,  $F_B$ , that must be overcome. The laser pulse produces a BAW that propagates through the substrate. The reflected surface acoustic wave (SAW) then accelerates the analytes away from the surface. If the substrate material is not ruptured, it experiences a straining force that, at the point of maximum displacement, reverses the direction of the wavefront. Thus, it is the differential velocities between the analyte traveling away from the surface, and the top surface layers returning to normal displacement that provides momentum to the particles in a direction opposite the surface. This differential momentum, divided by the time scale set by the pulse duration, produces the ejection force,  $F_E$ , necessary to overcome  $F_B$ . The requirement for desorption is then:

$$F_B < F_E \quad (2)$$

Without exactly modeling the ejection force based on the original laser pulse and material properties as done elsewhere [6, 19-21], it suffices to conclude from the cited work that the ejection force is dependent on the pulse amplitude and the inverse of the pulse duration,  $\Delta t$ .

$$F_E \propto \text{amplitude}, \frac{1}{\Delta t} \quad (3)$$

This basic formulation leads to several requirements for the properties of the substrate and the laser. For the laser one requires: a short pulse time (nanosecond or better), high intensity (usually  $\sim 10^9$  W/cm<sup>2</sup>, varies with choice of substrate and analyte binding), and wavelength well-matched to the absorption properties of the substrate. For the substrate material, one then requires: optical absorption well matched to laser wavelength, a high coefficient to thermal expansion (to maximize wave amplitude), low thermal conductivity (to concentrate the heat energy and reduce

the acoustic pulse rise time), and a large Young's modulus (stiff materials will increase the BAW velocity leading to both larger SAW amplitude and shorter time.)

#### 4.4 Engineering the substrate

A single material that well-satisfies all these properties is difficult to find. Typically, materials with high thermal expansion also have high thermal conductivity. Shea *et al.* [9] experimented with a variety of thin metal foils and concluded that Ti foil, 12  $\mu\text{m}$  thick, produced optimum results. Others [13] employed high resistivity silicon wafers (500  $\mu\text{m}$  thick). The high resistivity of the silicon was seen as necessary for efficient optical absorption into the lattice without exciting electrons into the conductance band [private correspondence].

Initial experiments in the LIAD-NEMS setups with both Ti foil and Si wafers failed to produce desorption. This included a variety of sample preparation procedures including dried-droplet from a pipette at room temperature, dried droplet on a hotplate (60° C), spin coating, and electrospray deposition. The lasers used in these studies were a nitrogen laser (NL100 from Stanford Research Systems) and a frequency tripled Nd:YAG laser (Marathon from Blue Lion Biotech). With high focusing, estimated spot intensities of  $10^8 \text{ W/cm}^2$  were attained, comparable to the above-cited studies that relied on bare foil or silicon. Using this configuration, no jumps were seen on the NEMS device and visual inspection of the samples under a microscope yielded no evidence of analyte desorption. It is possible that the actual intensity was significantly less than the estimated value due to scattering and attenuation factors in the setup. Because increasing the laser power necessarily increased the heat generated, which could risk damage to the protein, it thus became necessary to further enhance the substrate to maximize  $F_E$ . Efforts were also made to minimize  $F_B$  by varying the drying methods (as mentioned above) and chemically treating the substrate surface to reduce sticking. Ultimately, maximizing the acoustic pulse yielded results.

Experiments by Yuan and Gupta [19-21], which sought to investigate thin film interface strength through laser spallation, necessitated a detailed study of the generation and optimization of laser-induced acoustic waves. In short, their setup consisted of a laser pulse incident on the backside of a substrate, while on the front side were pre-deposited thin films and a laser interferometer to measure surface displacement and pulse time.

Yuan and Gupta conclude that the optimum substrate is not a single material but a composite structure featuring three layers: a confinement layer, an absorbing layer, and substrate or acoustic layer. A diagram is shown in Figure 23. A dedicated absorption layer is chosen to maximally capture the laser energy and yet be made thin enough to minimally attenuate the acoustic pulse. This allows the substrate material to be separately chosen for optimal acoustic transmission and SAW amplitude, without also requiring it be a good optical absorber. The absorption layer thus needs to be of sufficient

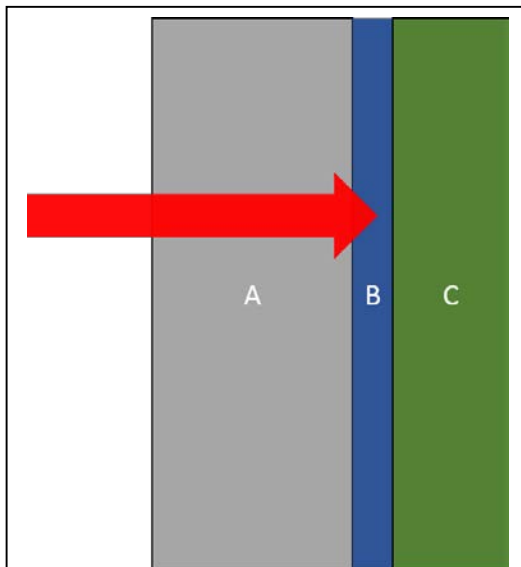


**Figure 23| Composite substrate stack for maximizing a laser-acoustic pulse.** The laser (red arrow) is focused to the absorption layer (B). The expansion of the absorption layer is directed forward by the confinement layer (A), while the acoustic layer (C) transmits the pulse with minimal losses.

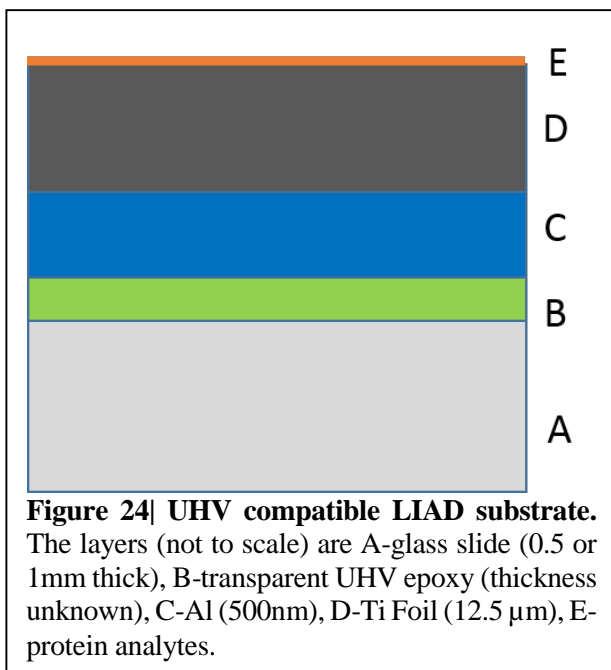
thickness to exceed the penetration depth of the laser wavelength but thin enough to have poor thermal diffusion, which will reduce the pulse rise time and thus increase the force of ejection [21].

The confinement layer, ideally made of a thick, dense medium, is meant to direct the initial expansion pulse in the forward direction. Independent of the laser incidence angle, the absorption layer will expand equally in all directions, absent neighboring materials. Thus, the energy that propagates in the backward direction is then wasted as it does not contribute to the pulse amplitude at the analyte surface. The confinement

layer serves as a high acoustic impedance point, preventing expansion in that direction and forcing all of the energy into a forward propagating pulse [21]. The use of a confinement medium was shown to enhance the pulse amplitude almost by a factor of two [21], indicating near total expansion confinement and redirection. The authors experimented with a variety of confinement mediums including a liquid water cell and a solid based on a material called liquid water glass (LWG). LWG is deposited on the backside of the substrate as a liquid, but when cured, behaves like bulk solid glass. Concern must be taken that the confinement layer minimally reflects or absorbs the laser light. In those studies, liquid water glass was found to be the optimum confinement layer.

Adapting the conclusions of [21] for LIAD-NEMS-MS required, first, consideration of the vacuum compatibility of the different layers used. A liquid cell is obviously impractical. Liquid water glass, though nominally solid, was not found to be vacuum compatible even after extensive curing and drying. Cracking and flaking always resulted after pumping down to even a few mTorr. Thus, standard microscope glass slides were chosen as the confinement layer. Following the results of [9], Ti foil, commercially bought (12.7 $\mu$ m thick, Alfa Aesar), was used as the substrate layer. A thin (500 nm) film of Al was used as the absorption layer, since Al has higher absorbance at the operating laser wavelength (337nm) than Ti. The UHV epoxy was used only to attach the Al-coated Ti foil to the glass and was intended to affect the LIAD process. The final configuration is displayed in Figure 24.

Substrate preparation was as follows: The commercially available Ti foil was cleaned with acetone, IPA, and methanol, and 10 minute exposure to UV ozone to ensure the complete removal of organics and other contaminants. Then, 500nm of Al was sputtered onto the backside of the foil using magnetron sputtering deposition. The Al side of the foil was then coated with UHV compatible epoxy (Stycast 1266 A/B, Emerson and Cuming) and placed on a microscope glass slide (Fisher Scientific) that had also been pre-cleaned with acetone, IPA and methanol. The substrate was cured first in air



as per the epoxy manufacturer specifications (60° C for two hours, then 100° C for two hours). The substrates were further cured overnight inside of a vacuum chamber (~500 mTorr) to ensure complete removal of air pockets. Finally, after curing and cooling to room temperature, the surface was again cleaned with acetone, IPA, methanol and UV ozone. Proteins were then deposited as the last step before insertion into the main

vacuum chamber of the NEMS-MS experiments.

This engineered substrate stack was used in the same system where prior substrates were used without successful desorption. The new substrate stack was successful as evidenced in Figure 25, which shows the desorption spots of a film of GNPS (10nm). The film consisted of GNPS in a methanol solution that was drip-dried onto the substrate surface on a hotplate at 60° C to promote rapid drying. The pictures in Figure 25 were taken under a microscope with a CCD camera after the exposure to the pulsed laser and removal from the vacuum chamber. In this experiment, the Marathon laser (200  $\mu\text{J}$  / pulse, 3.5ns pulse, 335nm) was operated at 1Hz. The laser spot was fixed and the substrate was scanned in X and Y. The scanning was manual using a joystick, thus producing the irregularly-spaced desorption spots. The elliptical shape of the desorption spots is partly explained by the incident angle of the laser beam in the X direction (45°) compared to the normal angle in the Y direction. To maintain vacuum chamber integrity and XY sample motion, the laser beam could not be inserted collinear to the substrate normal but had to enter the chamber through a different viewport,

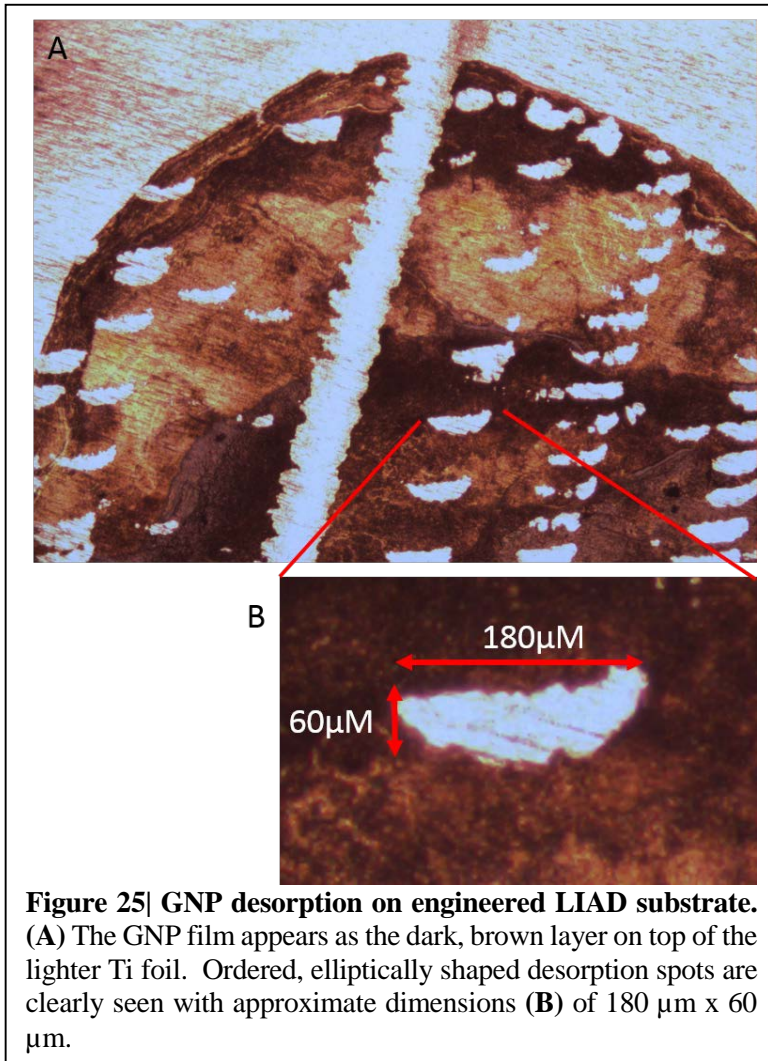


**Figure 25| GNP desorption on engineered LIAD substrate.** (A) The GNP film appears as the dark, brown layer on top of the lighter Ti foil. Ordered, elliptically shaped desorption spots are clearly seen with approximate dimensions (B) of 180 μm x 60 μm.

limiting the x-angle of incidence to 45° (see Figure 26b). The crescent shape is not well understood but may be an artifact of the epoxy curing process resulting in a directional strain in the titanium foil.

As mentioned previously, this same experiment, repeated with other substrates, was unsuccessful in achieving desorption. Additionally, removal of any one of the layers in the engineered

substrate also failed to produce desorption. This indicates that the engineered substrate indeed enhances the acoustic pulse amplitude and speed to increase the ejection force of the surface film, and that all the included layers were indeed necessary.

Though successful in desorbing GNPs, this substrate and laser combination was not successful in desorbing various protein solutions. This indicates that proteins have a higher sticking coefficient to the Ti foil surface than GNPs. While the higher binding force of protein might be overcome by continued increases in laser power, this can risk damage to the proteins [9]. Therefore an engineered substrate is necessary to minimize required laser power and thus the risk of damage to

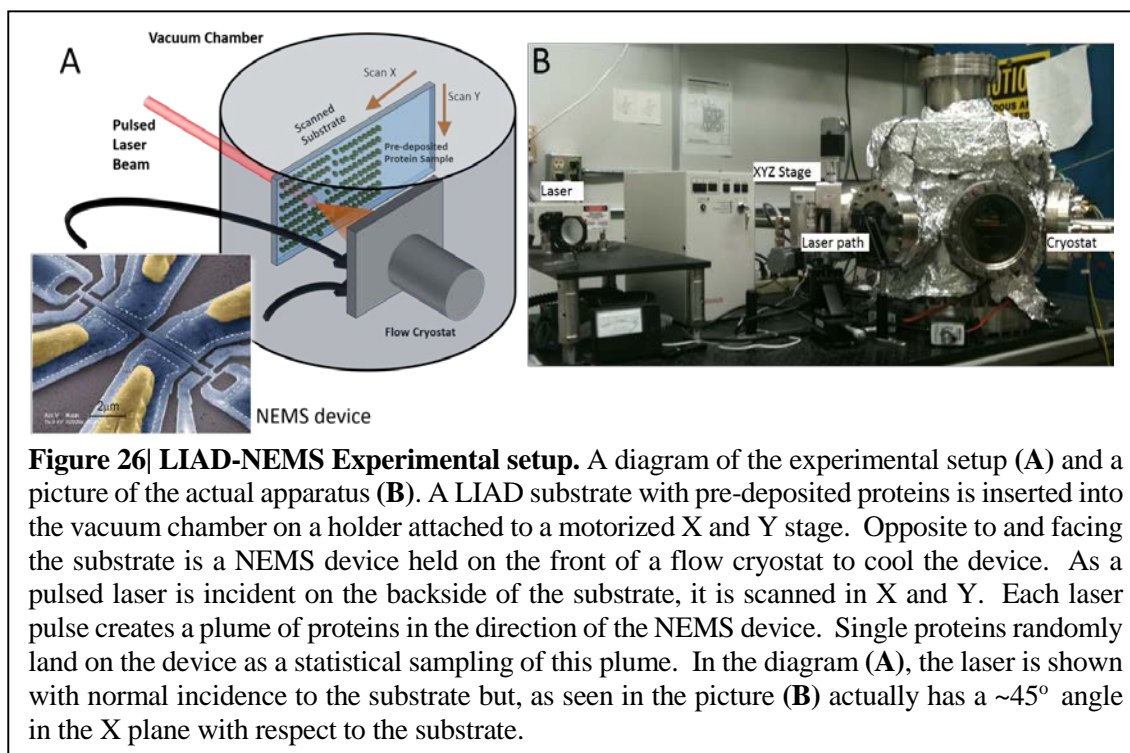
the proteins before the binding force is overcome by simply boosting the laser power. Additionally, since future work will utilize arrayed-NEMS devices which will require a larger desorption plume and laser spot, it is advantageous to minimize the required laser intensity through substrate optimization. Though methodologies exist to reduce protein binding by chemical treatments of the substrate surface, implementation would be extensive and is a subject of future work.

## **4.5 Experimental setup**

The experimental setup is shown in Figure 26. A LIAD sample, with pre-deposited surface proteins, is inserted onto the sample holder in the UHV chamber (Kurt Lesker). The substrate sample holder is connected to a motorized, UHV X and Y manipulator (Kurt Lesker). This manipulator also features z-axis manual movement to adjust the sample-NEMS distance. The LIAD sample is held opposite to, and facing, a NEMS device mounted at the end of a UHV flow cryostat (Janis). The NEMS chip mounting consists of a custom fabricated PCB to which the chip is attached with copper tape. The on-chip device leads are wire bonded to the PCB leads attached to soldered SMA heads. The cryostat allows for vacuum cooling of the device using liquid nitrogen or helium. The laser spot is previously aligned to the NEMS device using a transparent substrate without protein sample. The distance between the LIAD substrate and the NEMS device can be varied, but is fixed during an experimental run and is usually held at ~2-3cm.

During an experimental session, the laser is constantly pulsed at 1 Hz while the substrate is scanned in X and Y directions. Each laser pulse produces a plume of protein material towards the device wherein individual proteins randomly land on the device. At the same time, the device remains in a phase-locked loop (PLL) to track the two-mode resonance frequencies in real-time (see chapter three for details). When a protein lands on the device, simultaneous frequency jumps are recorded in each mode. These jump pairs are used to calculate the mass and position of each particle that lands on the device. The 1 Hz pulse rate of the laser was set to ensure that multiple proteins would not land on the device during a PLL time constant (250ms). Future work with the next generation of electronics will enable significant reduction in the PLL time constant ( $<10\text{ms}$ ), which will in turn allow for faster laser pulse rates and thereby increase data collection rates (even with a single device) by at least an order of magnitude.

Further details of the chamber setup and construction are given in chapter two. For the LIAD experiments, an Nd:YAG laser was used featuring much greater power than the previous lasers. The



new laser, a Minilite II from Continuum (10 mJ/pulse, 3.5 ns pulse width, 337nm), proved to be the final requirement in obtaining protein desorption.

## 4.6 Protein deposition

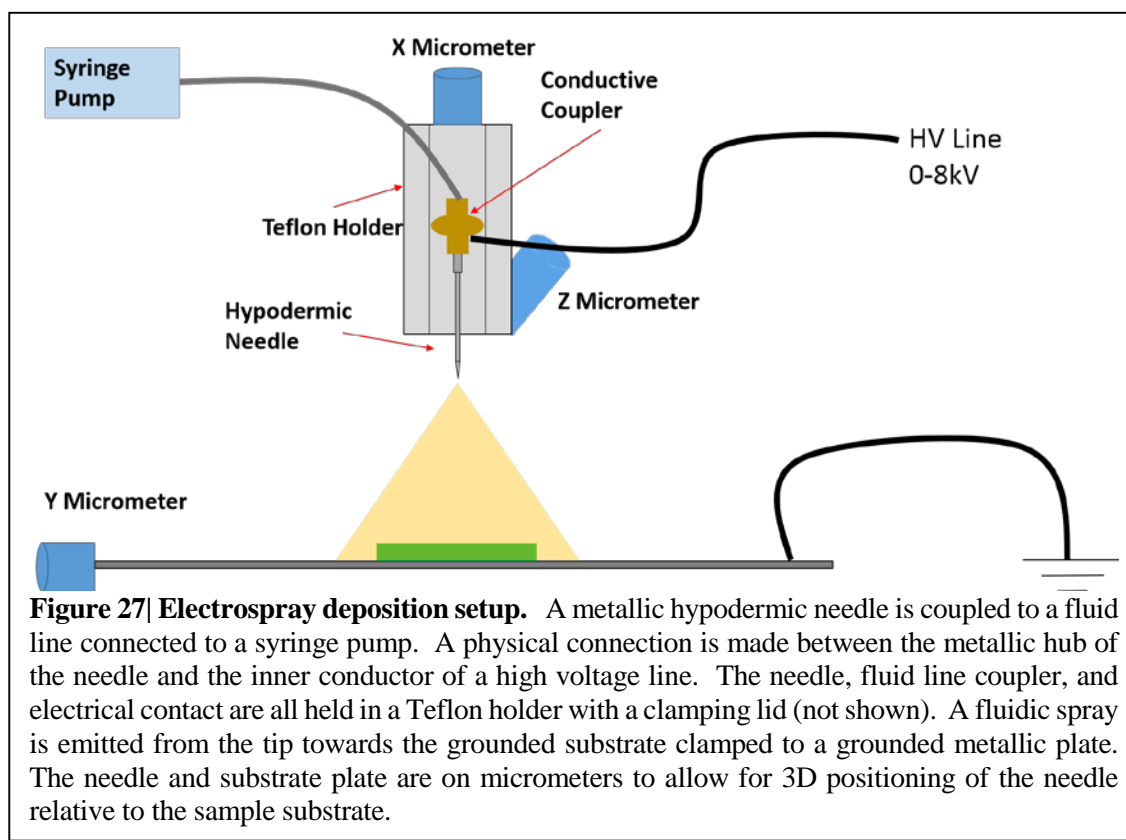
Initially, proteins were deposited on the LIAD substrate from solution using a pipette and dried in ambient conditions. As will be seen below, while this suffices for protein desorption and detection by the NEMS device, significant bunching effects remain. To overcome these bunching effects and reduce the protein binding force, an electrospray deposition setup was constructed (Figure 27). Electrospray deposition is an established technique within the mass spectrometry community to prepare LIAD and MALDI samples with good homogeneity and, in the case of MALDI, good mixing of analyte and matrix. For present purposes, the main advantage of electrospray deposition is isolation of the protein molecules (to avoid bunching) and faster drying (reduces binding force and also helps reduce bunching).

In the following mass spectra, some results were obtained from electrospray deposition and some from pipetting. Moreover, the electrospray deposition setup underwent several iterations. Figure 27 displays the final iteration of the electrospray deposition setup from which the majority of the results were obtained.

As seen in Figure 27, a stainless steel hypodermic needle (VWR) is connected by a conductive coupler to PEEK tubing. The needle's inner diameter is 300  $\mu\text{m}$ . The tubing originates at a syringe pump that can vary the flow rate out of the needle up to 9  $\mu\text{l}/\text{min}$ . A physical connection is made between the metallic hub of the needle and the inner conductor of a high voltage line. The needle, line couple, and electrical contact are all held in a custom-machined Teflon holder with a clamp to ensure proper connections (Teflon clamping lid not shown). Based on known principles, when the high voltage and the pump are both operating, a fluidic spray is emitted from the tip featuring

the characteristic Taylor cone of electro spray systems. The Taylor cone can be seen under high flow conditions with the aid of a magnifying glass and strong light conditions. The substrate is clamped on a conducting plate connected to the power supply ground. The clamps ensure electrical grounding between the Ti foil and the grounded plate. The high voltage supply uses the same ground. The needle and substrate plate are on micrometers to allow for 3D positioning of the needle relative to the sample substrate. Needle-substrate distance is variable and set to 4cm for most runs. The needle is usually held at 6kV (a single Taylor cone is observed up to the maximum voltage, 8kV).

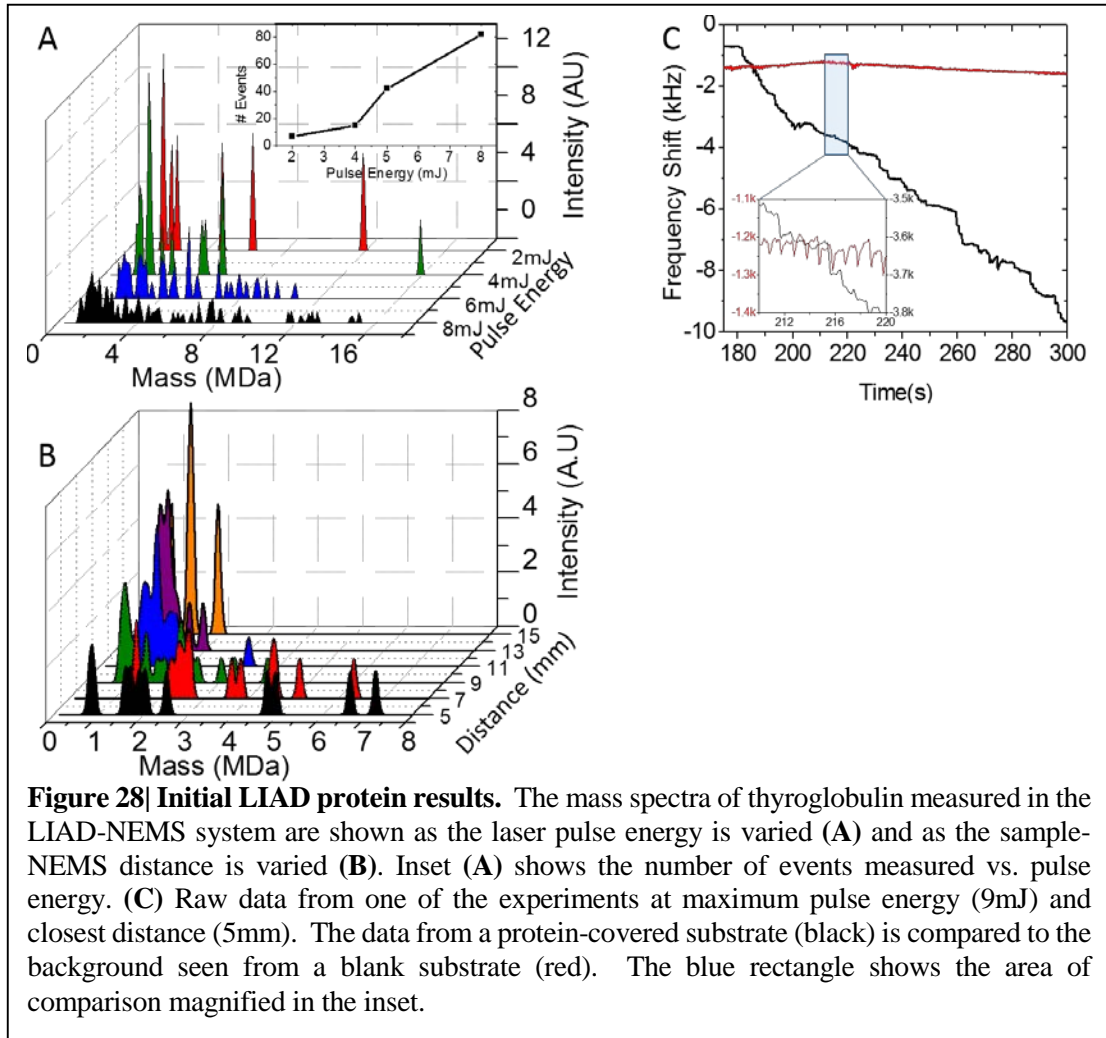
A previous incarnation of electro spray deposition setup featured a Varian electro spray needle assembly. This assembly contained connections for high voltage supply, the liquid sample, and N<sub>2</sub> drying gas. The needles used in this setup had an inner diameter of 100 μm and were operated at a lower voltage of 3.5kV. This setup was used for the IgM, thyroglobulin, apoferritin, and RAG



complex samples, while the 300  $\mu\text{m}$  needle setup was used for the proteasome complex and the ribosome results. The 100  $\mu\text{m}$  needle often clogged after only a few runs, despite thorough flushing between runs and ammonium acetate buffer exchange of the protein solutions. The protein solutions were usually between 0.5 and 2  $\mu\text{M}$  ( $M = 1 \text{ mole/L}$ ), and this high concentration may be responsible for the clogging.

#### **4.7 Results: protein desorption**

Using the Minillite II laser and the engineered substrate, thyroglobulin was successfully desorbed and detected by the NEMS device. The results of this first successful protein desorption are shown in Figure 28. The thyroglobulin (Sigma Aldrich) was deposited using a previous electrospray deposition setup with much closer needle-sample distance (1 cm) and no proper grounding. These sample conditions largely explain the high amount of bunching seen in the mass spectra. As the laser power is reduced (Figure 28a), the total number of events declines, but the bunching effect remains. This indicates that while laser power is needed for efficient desorption, it does not significantly affect the clumping of particles desorbed from the surface. As the distance between the sample and the NEMS (Figure 28b) is varied, however, there is a clear reduction in relative intensity of high mass species. This indicates that bunching is caused by clumps of particles loosely held together that, when ejected into the gas phase, require time to fully separate. This data also suggests that some of the bunching effects may be due to multiple particles landing on the device. As the distance is increased,



the flux rate is reduced. Subsequent experiments were performed at a distance of 20 mm (not shown in Figure 28) to minimize the possibility of measuring clumping event and/or multiple particles. From Figures 28a and 28b, however, it is apparent that the experimental parameters cannot fully compensate for sample preparation conditions. This motivated improvements to the sample electrospray setup resulting in the configuration shown in Figure 27.

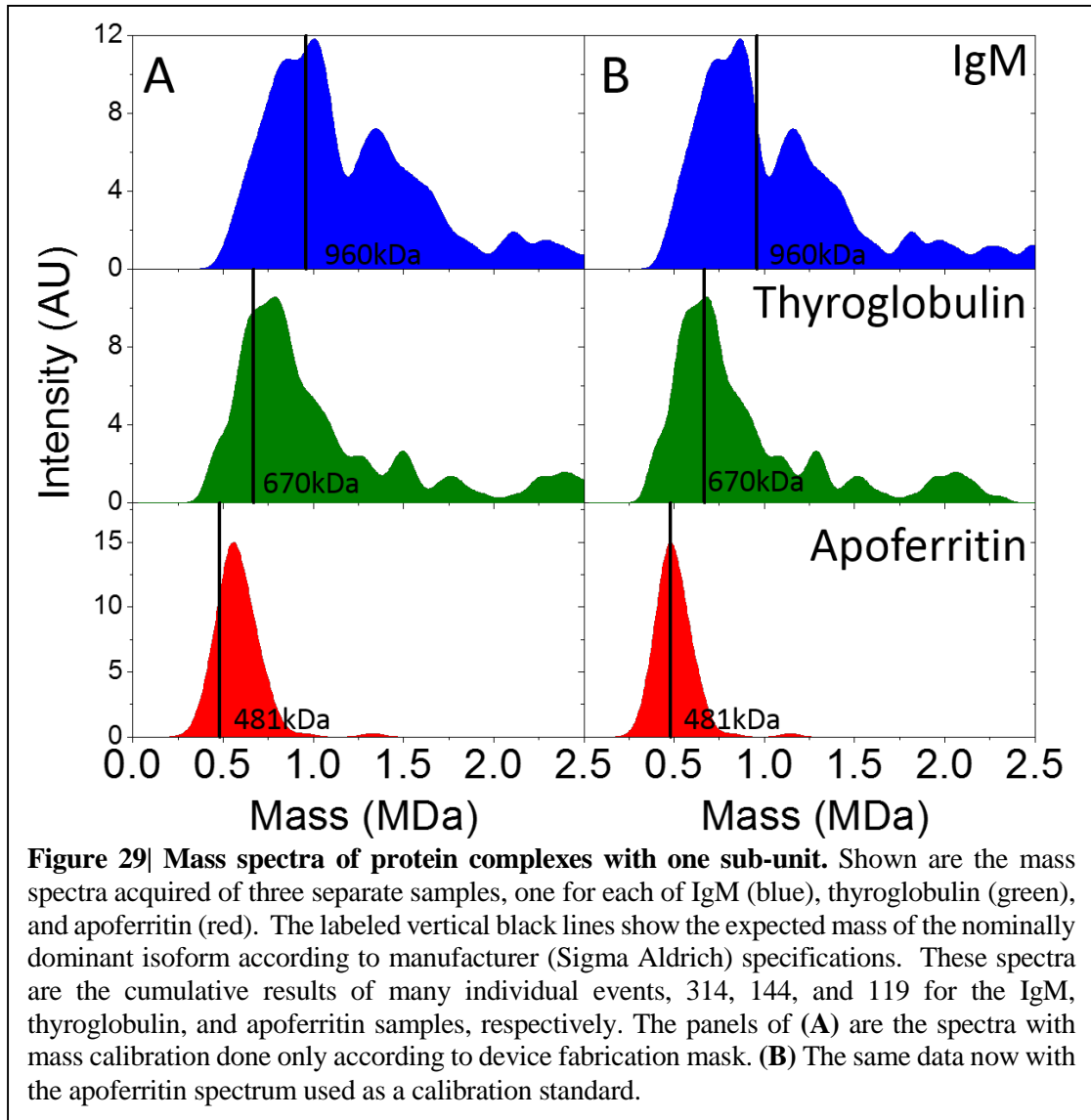
A concern in the implementation of the LIAD process is that the substrate itself is not ablated and thereby contaminates the sample. Figure 28c shows the first mode temporal frequency raw data of the NEMS device for a substrate with (black) and without (red) a pre-deposited protein film. The effect of mass loading from the protein substrate is clearly seen as precipitous jumps (black), while

the blank sample (red) shows no precipitous jumps indicative of mass loading. However, there are background effects seen from the blank sample shown in magnification in the inset of Figure 28c, where the frequency briefly jumps down and then returns to the original level. During the experiment, the sample was manually moved while the NEMS frequency was monitored in real time. These jumps occurred only when the laser spot was near the edge of the sample and are due to light scattering directly onto the NEMS device, an effect seen previously.

This data was acquired at the maximum available laser energy (9mJ) and point of closest approach (5mm). While the laser-induced jumps are of comparable size to the mass data, this plot clearly shows that the Ti foil substrate is not ablated and only the pre-deposited proteins are ejected towards the NEMS device. Microscopic investigations of the substrates before and after exposure to the laser confirmed this with no evidence of substrate ablation on the front side exposed to the NEMS. To counter the laser-induced false jumps, a frame of copper tape was placed around the perimeter of each LIAD substrate sample. This proved successful in eliminating laser-scattering effects on the NEMS.

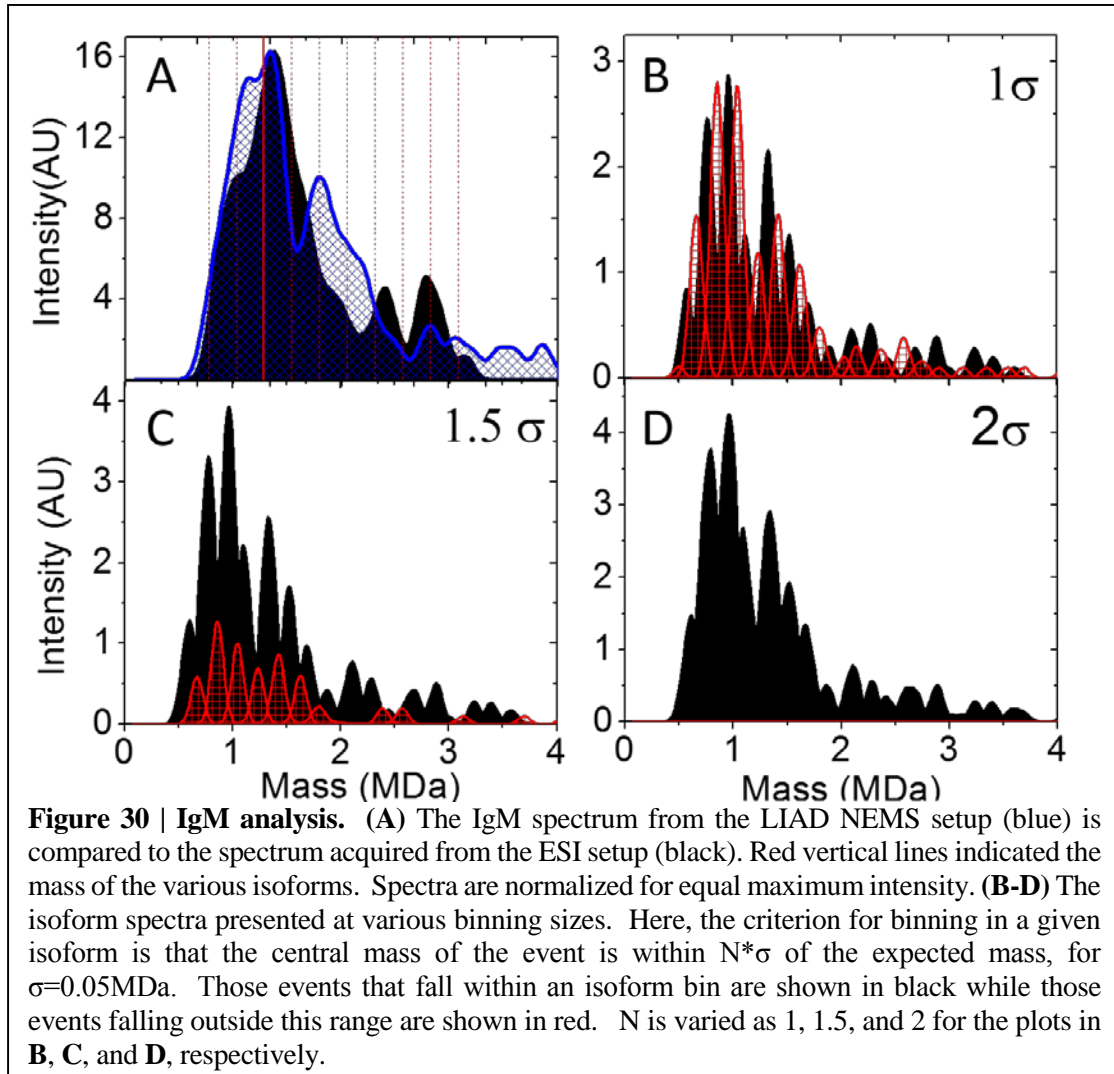
## **4.8 Results: protein mass spectrometry**

Now, with an improved electrospray deposition setup, engineered substrate, and a sufficiently powerful laser, identifiable protein spectra were obtained using a single NEMS device. Shown in Figure 29 are spectra taken from three protein complexes that are each composed of a single sub-unit. As in chapter three, these spectra are the cumulative result of the individual spectra acquired for each particle event. The additive process of constructing cumulative spectra from individual events is detailed in chapter three. The total number of individually measured particles used to construct each spectrum are 314, 144, and 119 for IgM, thyroglobulin and apoferritin, respectively.



During the experiments, the sample-NEMS distance was 25 mm, the laser pulse power was 7mJ and the repetition rate was 1 Hz.

All three spectra are close to the expected results, but not exactly matched. As seen in Figure 29a, for the IgM and thyroglobulin spectra, significant intensity is seen at higher mass values. While some of these are due to the presence of larger isoforms in the sample, it is also possible that a minority of these events are clumped particles or multiple particles landing on the device. Additionally, while



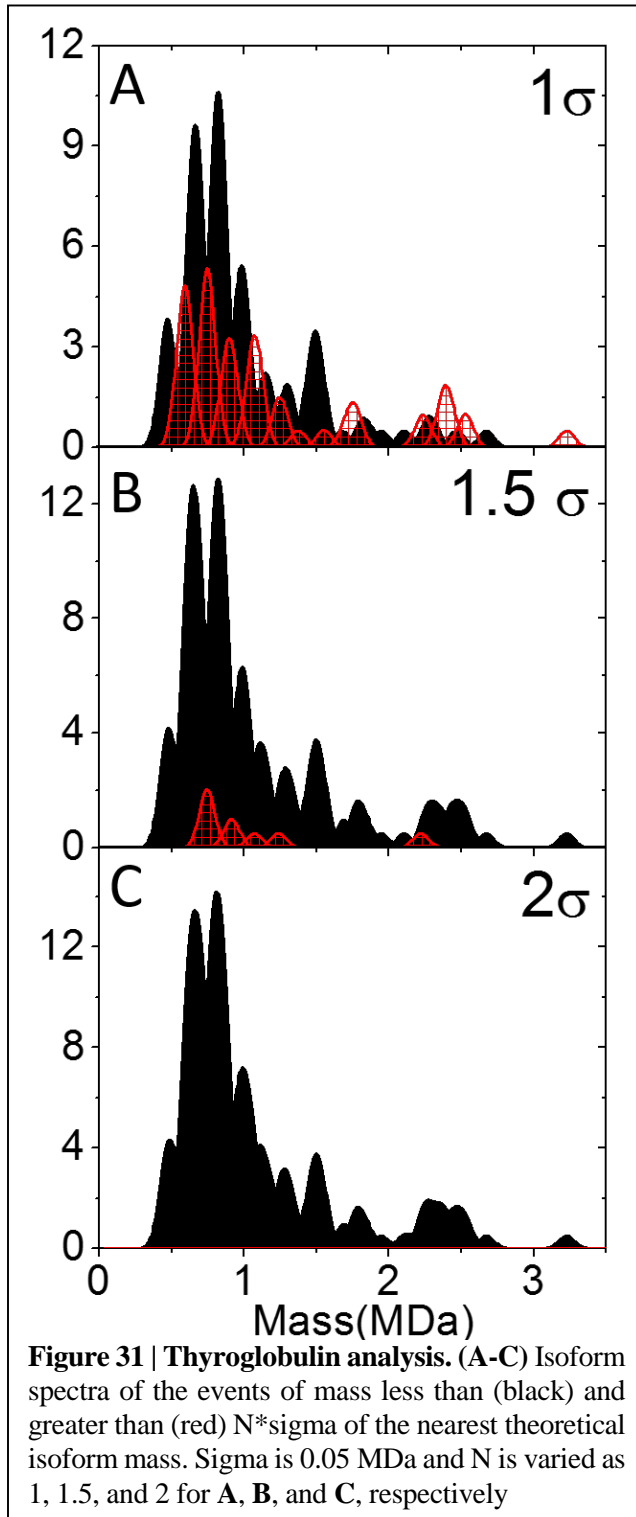
the dominant IgM peak at  $1.00 \pm 0.05 \text{ MDa}$  is within the uncertainty of the expected mass ( $0.96 \text{ MDa}$ ) of the dominant isoform (the pentamer), both thyroglobulin and apoferritin display a dominant peak close to, but outside the uncertainty range of the expected mass. In the case of thyroglobulin, there are evidently two peaks with similar intensity values that dominate the spectrum. The centroid of the slightly smaller peak,  $0.67 \pm 0.05 \text{ MDa}$ , exactly matches that of the theoretically dominant isoform (the tetramer). The more experimentally dominant peak, however, at a mass of  $0.79 \pm 0.05 \text{ MDa}$ , is within uncertainty of the next highest isoform, the pentamer with an expected mass of  $0.835 \text{ MDa}$ .

Finally, regarding apoferritin, while the spectrum is much cleaner than the other two, the observed peak mass of  $0.56 \pm 0.05$  MDa is outside uncertainty of the expected mass value of 0.48 MDa. In the following, a more in-depth analysis of each individual spectrum is undertaken.

These differences between the experimental peaks and the expected values are possibly explained by a calibration offset. The mass spectra are here calibrated only according to the nominal device dimensions from the mask fabrication. Alternatively, one could use one of the measured protein species as a calibration standard. Figure 29b displays the same spectra as in Figure 29a, where now apoferritin is used as calibration standard. In this case, the thyroglobulin spectrum is well matched between the dominant peak and the expected value. The IgM, spectrum, however, now displays a dominant feature well below the expected value. Additionally, as is shown below, the sub-unit masses of the multi-unit protein complexes are well matched to expected values using only the device fabrication mask for mass calibration.

None of the present measurements individually produce a linear calibration offset that appears equally valid for all the other species. A nonlinear calibration is possible, but is not well explained with present NEMS-MS theory. It is also possible that a linear calibration offset could be altered for different samples or experimental sessions, if due, for example, to a background affect. The following analysis is performed without calibration other than nominal fabrication values, but it is possible that a lack of calibration can explain some of the offsets seen in the data.

The IgM data summarized in Figure 29a is analyzed in greater detail in Figure 30. First, in Figure 30a, the IgM spectrum from the LIAD-NEMS system (blue) is compared with that taken on the ESI-NEMS system (black) described in chapter three. The LIAD curve represents the cumulative result of 315 individual events, while the ESI curve represents 75 events. The two spectra are normalized to have equal intensity at the global maxima for ease of comparison. The two curves match quite well regarding the location of the dominant isoform, the pentamer, as well as the locations



of the peaks of the various isoforms. The relative intensities of the isoforms, however, exhibit some fluctuation. This is explained in part by the differences between the actual samples used. For the ESI data, the sample was IgM from human serum, while the LIAD data was taken using IgM derived from mouse serum. It is possible that the two species express relatively different levels of the various isoform populations. Furthermore, the protein delivery mechanism (ESI or LIAD) could possibly affect the isoform intensities. Finally, statistical fluctuations may result in variances in the relative intensities of the isoform subpopulations.

The mass of the IgM sub-unit, 0.195 MDa, provides the location of the expected peaks of the isoforms at  $k \cdot 0.195$  MDa ( $k=1, 2, 3 \dots$  etc.). The problem then consists of accurately labeling the individually measured particles as one isoform or another. This is the same as the

binning problem for a histogram. Each event is identified with its peak or central mass (the events

are all Gaussian or near-Gaussian along the mass axis). The peak masses for each event are then binned. The bin centers are the theoretical isoform masses and the widths are twice the experimental uncertainty, 0.05MDa ( $= \sigma$ ). All those events within each bin are added together to form the black peaks seen in Figure 30b. Some events, however, fall outside the bins. All of those events that lie between neighboring isoform bins are similarly added together and are plotted as the red curves in Figure 30b. In this way, one can measure how many of the measured events correspond to the expected isoform mass, and how many have mass values farther away from the expected values and might possibly represent contaminants or experimental errors. The uncertainty level of 0.05MDa represents a statistical average of the frequency fluctuations. Thus, individual frequency jumps could have uncertainties larger or smaller than this amount. The bin width is then increased as coefficients of  $\sigma = 0.05\text{MDa}$ . Thus, at a bin width of 1.5 times  $\sigma$  (Figure 30c), the number of events that fall within the expected isoform mass bins (black curves) is far greater than those that fall outside of these bins (red curves). As the bin width is further increased to two times  $\sigma$  in Figure 30d, the red entirely disappears since, at that bin width, the bins are now touching.

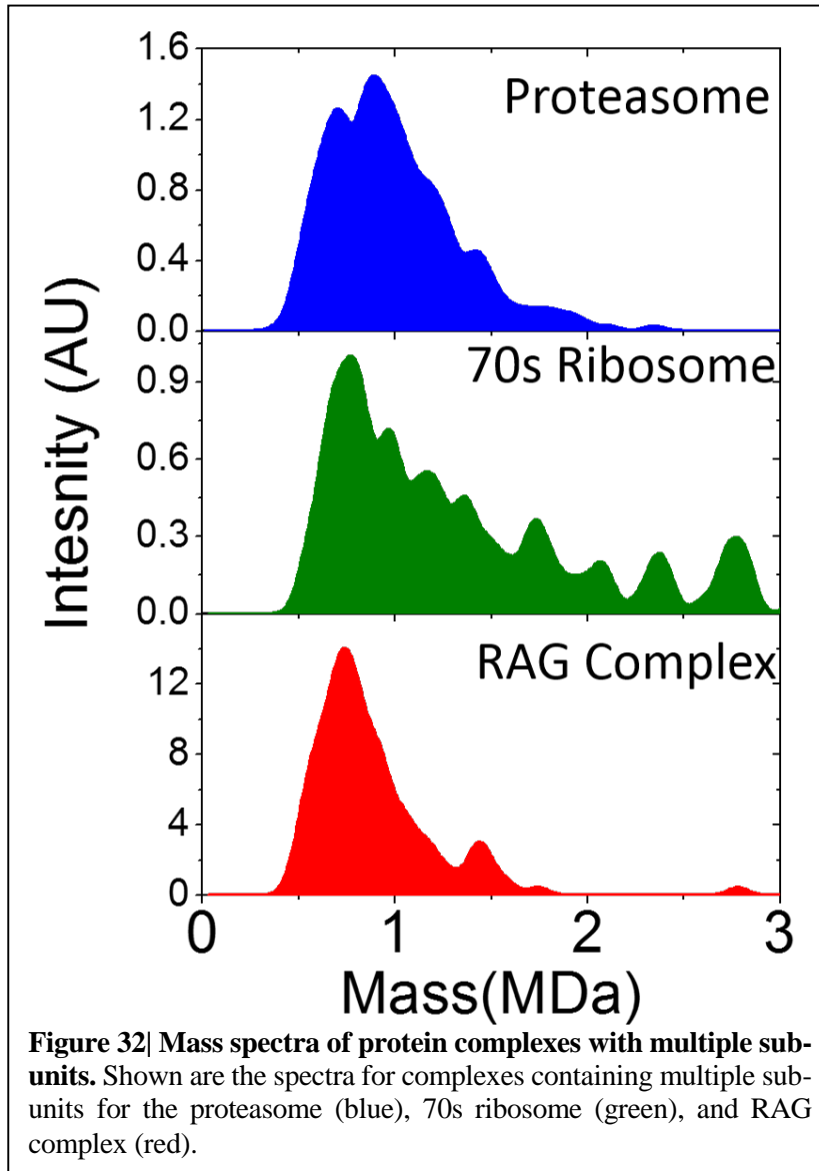
This binning analysis suggests that the quoted uncertainty level of 0.05MDa, which is based on the Allan Deviation measured with the laser off, may be under-representing some of the actual uncertainty in the measurement. While contamination may be an issue as it is with many mass spectrometry experiments, it is unlikely that contaminants were so evenly distributed as to increase the number of events outside of the expected isoform mass bins. For Gaussian distributed noise (as is the case here), all events within one sigma of the expected (zero noise value) should be 68% of the total. Thus, if the noise level is 0.05MDa, the number of events representing the black curve in Figure 30a should be 68% of total. In this case, the black events (165) are 53% of the total, only slightly more than half. The 68% mark is not reached until the bin width is increased to 1.3\*sigma. This indicates that the actual mass resolution is  $1.3 \times 0.05 \text{MDa} = 0.065 \text{MDa}$ , a 30% increase over the level

given by frequency fluctuation alone. One may thus conclude that the many peaks seen in the cumulative IgM spectrum (Figure 29a top and Figure 30a) indeed represent the various isoforms, but that the actual uncertainty or variation in the individual mass measurements is 0.065MDa. This additional source of fluctuations may be due to a small-particle background from the sample.

A similar analysis is done for thyroglobulin, shown in Figure 31. In this case, at the 1\*sigma level (Figure 31a), the black events represent 64% of the total, with the 68% mark reached at 1.1\*sigma = 0.055 MDa, a 10% increase. This indicates that the additional (i.e., not frequency-based) noise present during the measurement was less for the thyroglobulin experiments than the IgM experiments. Nonetheless, the analysis demonstrates that the various peaks seen in Figure 31a are due to the presence of different isoforms of thyroglobulin. In both the IgM and thyroglobulin cases, it is noted this analysis is possible only because the sub-unit masses of these two structures are known *a priori*. Without this structural knowledge, more resolution or greater sample purification (to eliminate the non-dominant isoforms) would be required for discovery-mode species identification.

Additionally, both these mass spectra exhibit tails in the mass intensity at the high mass end but not the smaller mass end. This indicates that, though bunching or multiple landing events may occur in a minority of events, they are nonetheless agglomerations of the whole species to be measured and not random assortment of smaller fragments. If the latter were the case, then the distributions would feature tails on the short mass end and the peaks would exhibit much less agreement with the expected isoform mass distributions.

Apoferitin (from horse spleen, Sigma Aldrich), is a 24-meric complex with a sub-unit mass of ~20kDa (there actually two sub-units of 19.9 and 22.2 kDa, respectively, but our measurement is insensitive to this difference). Because the sub-unit mass is less than our mass resolution (50 kDa), an isoform analysis as done with IgM and thyroglobulin is not possible. As mentioned above, the



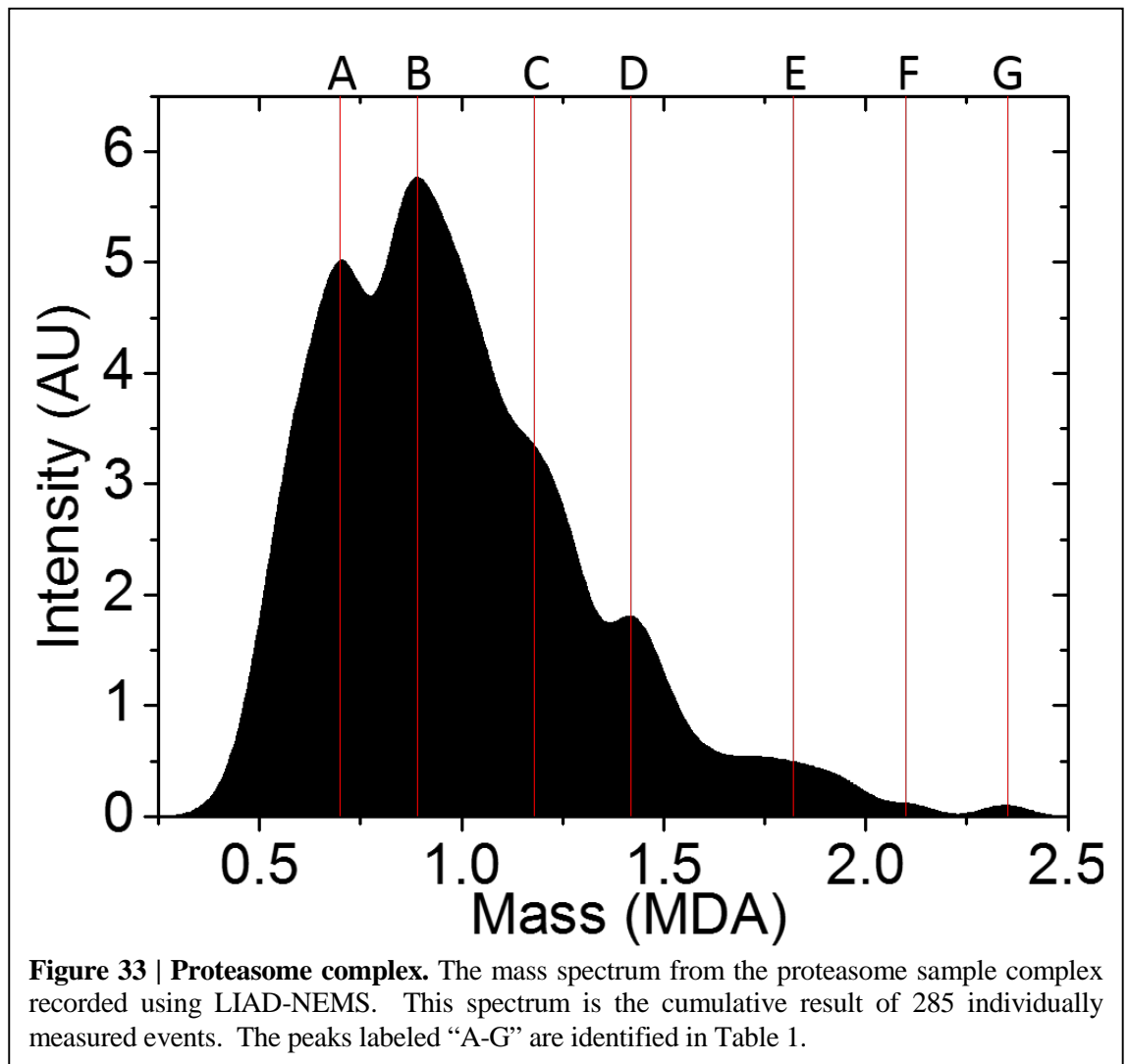
expected value of apoferritin (0.48 MDa) is outside the uncertainty range of the measured peak value (0.56 MDa), which may be due to a mass calibration offset. If the device were mass loaded (a possible cause of miscalibration), then the measured peak mass would be smaller, not larger, than the expected mass. As seen especially in the case of IgM, the actual mass uncertainty could be larger than 0.05 MDa, and if so, could

explain the 0.08 MDa discrepancy between the expected and measured values of apoferritin.

In addition to the apoferritin peak mass, one can analyze the width of the curve. It is possible that various apoferritin isoforms are present in the sample, and, because their mass differences are less than our resolution, the existence of these additional peaks results in an overall broadening of the main peak. A similar type of 480 kDa apoferritin was measured on an ESI-TOF system [16], and the peak corresponding to the whole complex does indeed feature a distribution of sub-units. In that case,

the measured peak had a half-width half-maximum (HWHM) value of 56 kDa while the red apoferritin peak in Figure 29 has a HWHM value of  $124 \pm 50$  kDa. Considering this uncertainty of 50kDa, it is possible that the width seen in the LIAD-NEMS data does indeed correspond to the native distribution of isoform subpopulations that are not resolvable with our current mass resolution. It should be further noted that the apoferritin measurement from [16] derives from a different species than what is measured here. This may further differentiate the relative intensities of isoform subpopulations, and thus the width of a mass spectral curve in which the isoforms remain unresolved.

In addition to proteins that form as multiples of the same sub-unit, several protein complexes composed of a different sub-units were also measured. Figure 32 shows the mass spectra for three



<b>Feature</b>	<b>Measured Mass (kDa)</b>	<b>ID</b>	<b>ID Mass (kDa)</b>
A	700	Core	670
B	890	Cap, Core+BLM10	917,915
C	1180	Core + Cap Scaffold	1220
D	1420	Two Cores	1340
E	1820	Whole Proteasome – (Cap Scaffold, Rpn1)	1836
F	2100	Whole Proteasome – (BLM10, Rpn1)	2148
G	2350	Whole Proteasome – Rpn1	2388

**Table 1| Peak identification of the proteasome complex.** The columns from left to right display the peak label, the peak mass, the sub-unit identification of the peak, and the theoretical mass of the sub-unit. All measured peak masses are within the uncertainty of 0.05MDa of the theoretical mass except for peak “D” whose value is 0.08MDa larger than the theoretical mass. Commas indicate alternative sub-unit permutations. On feature “B”, for example, the ID of “19s Cap, Core+BLM10” read as “19s Cap or a combination of the core unit attached to a BLM10 protein”.

such complexes measured on the LIAD-NEMS system: the proteasome, 70s ribosomes, and the RAG complex. In the cases of the proteasome and the 70s ribosome, the intact complexes at 2.5 MDa and 2.3 MDa, respectively, are fragmented into subcomponents. Meanwhile, for the RAG complex, which has a mass of 0.36 MDa, only the dimer and tetramer of the intact complex are clearly distinguishable as separate peaks.

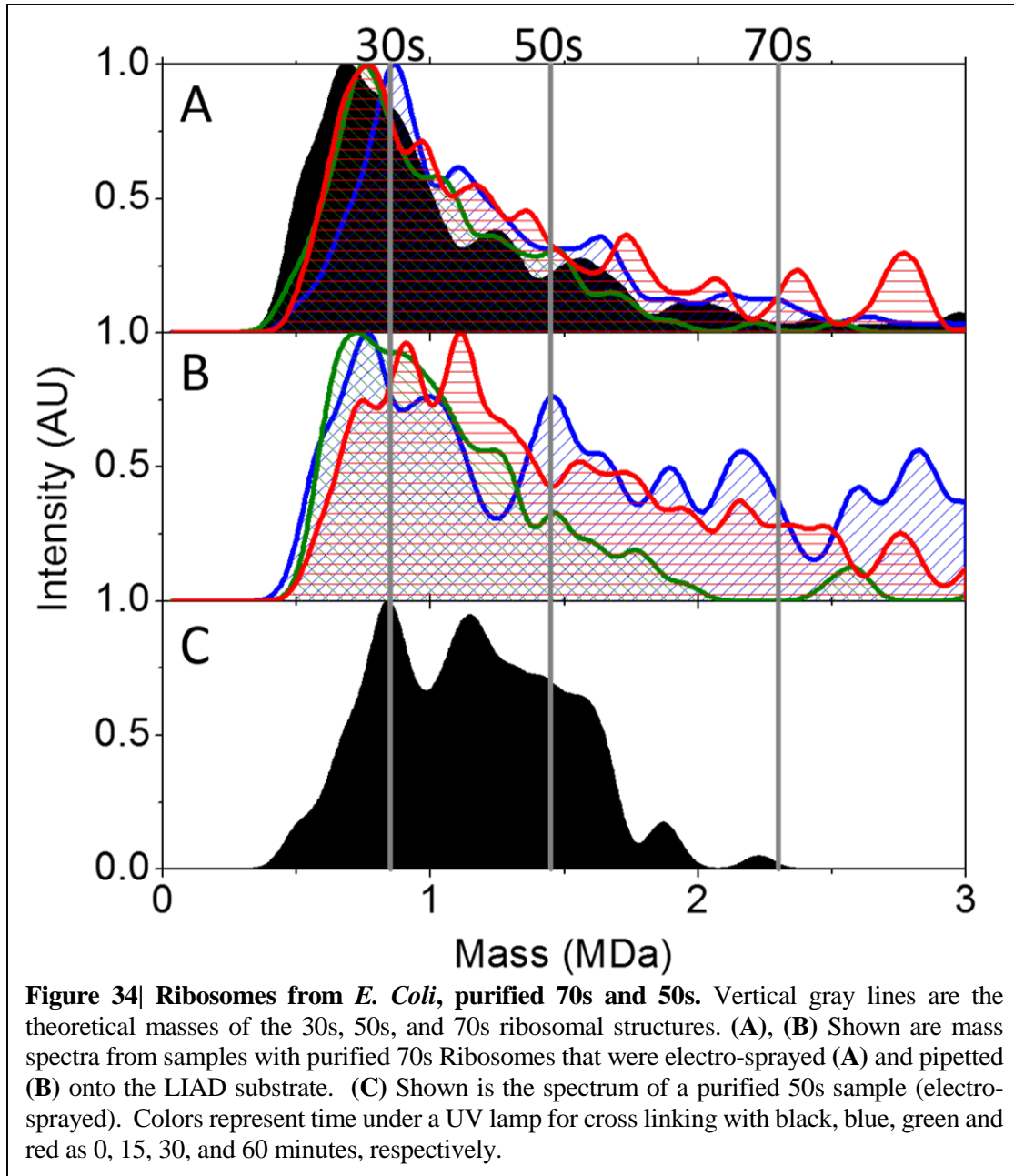
The proteasome (eukaryotic) samples were provided by our collaborator, Prof. Andreas Matouschek of the University of Texas at Austin. The RAG complex was also prepared by a collaborator, Geoffrey Lovely, of Prof. Rob Philip’s group at Caltech. The ribosome samples were

prepared by Adam Neumann, a graduate student in the Roukes group. In each case, there were significant discussions regarding proper buffer and sample preparation conditions. Continued improvement in the sample preparation of these protein complexes to improve stability is ongoing. Presented herein are initial results with identifiable mass features that match the known sub-unit masses.

The proteasome complex is a large structure inside the cell responsible for degrading cellular proteins and plays a critical role in many processes including cellular signal transduction, cycle regulation, transcription, destruction of mis-folded or damaged proteins, and produces some of the cell surface peptides as part of the adaptive immune response [22]. As a highly complex structure, identification of the various sub-units can be a difficult task, and Table 1 was produced via private correspondence with Prof. Matouschek and his student, Suchie Bhattacharyya.

An overview of the proteasome structure and various sub-units is found in [23]. The complex consists of the three main units, a core particle (670kDa) which contains the proteases responsible for degradation and two capping regions (917kDa each) responsible for selecting and admitting proteins to the core. The caps are in turn broken down further into a scaffold consisting of the proteins Rpn1 and Rpn2 and the receptor region consisting of Rpn10 and Rpn13 [23]. An additional protein, BLM10, is an alternative for the cap scaffolding present in the samples provided.

All of the peaks present in the mass spectrum of the proteasome seen in Figure 33 are thus able to be identified with known, biochemically possible, sub-unit permutations. Most prominent in the spectrum are two peaks that well correspond to an isolated core unit (peak, “A”) and an isolated cap unit (peak, “B”). During fragmentation, these are expected to be the most prevalent sub-units [private correspondence with A. Matouschek and S. Bhattacharyya]. Of all the identified peaks, only peak “D”, which corresponds to two core particles bound together, has a measured mass (1.42 MDa) that differs from the theoretical mass (1.34 MDa) by more than the experimental uncertainty



(0.05MDa). It is possible that when two isolated core complexes bind together, there are minor deletions in one unit.

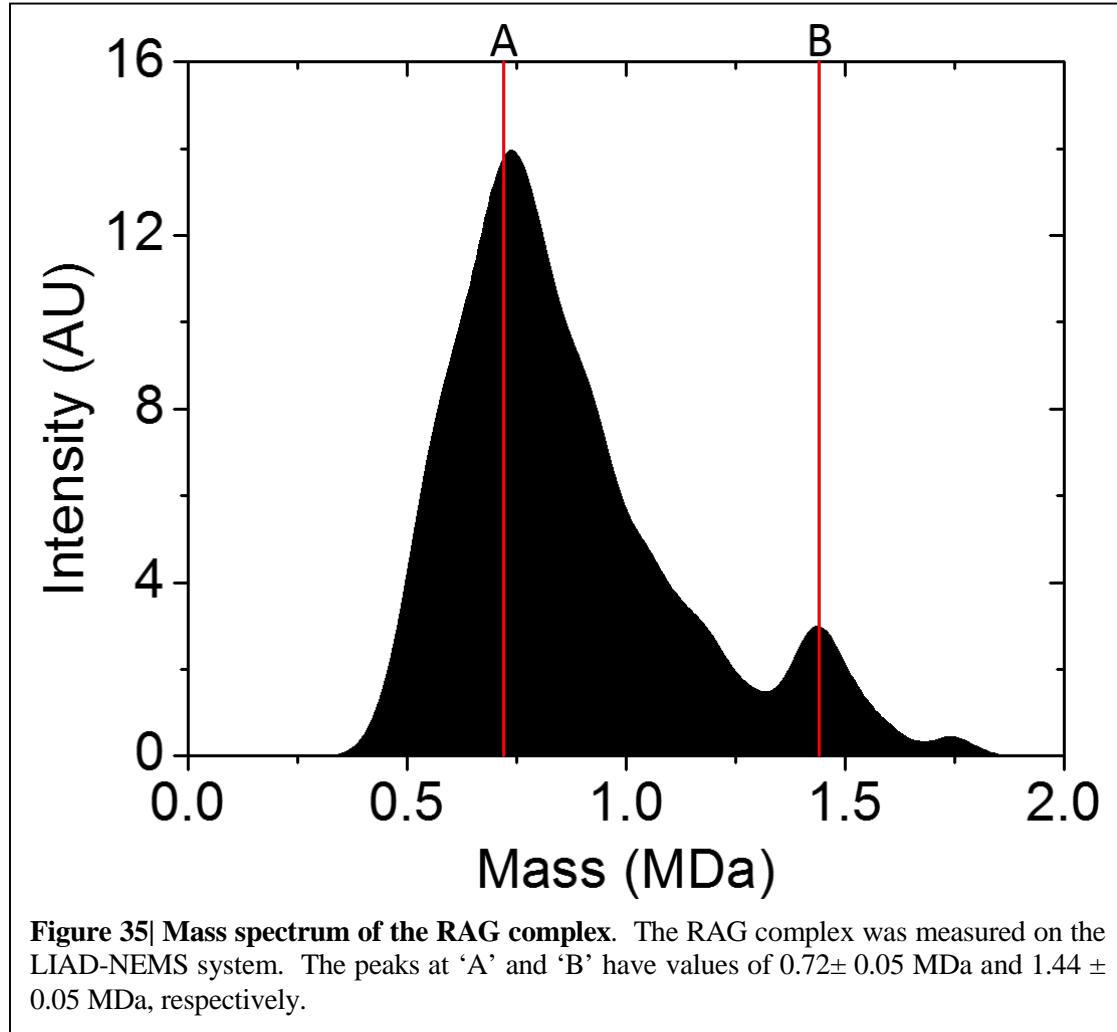
Another complex protein structure measured with the LIAD-NEMS setup is the *E. Coli*, ribosome. Ribosomes are highly complex structures consisting of an intact 70s unit composed of one 50s and one 30s sub-unit. The 50s (30s) sub-unit is in turn formed from 35 (20) different proteins

and 2 (1) RNA strands [24]. The 70s, 50s, and 30s complexes have masses of 2.3, 1.45, and 0.85 MDa, respectively. It is possible to purify each of the main sub-units as individual species. Additionally, ribosome formation can often produce dead-ends of partially intact substructures in many different permutations [25].

Regarding the mass spectra, a fully purified sample of 70s ribosome should produce a single peak at 2.3 MDa while, if partial fragmentation occurs, should also yield smaller peaks at 1.45 and 0.85 MDa, corresponding to the 50s and 30s sub-units, respectively. This triple-peaked structure would then be indicative of purified ribosomal particles without the “dead-end” substructures. As seen in Figure 34, only the 30s peak repeatedly appears as a dominant peak in the spectra while peaks at the 50s and 70s masses, though present, fail to locally dominate over nearby peaks of “dead-end” or fragmented substructures.

Apparent from these spectra is that the 70s and 50s sub-units both experience considerable fragmentation and peaks corresponding to the many possible intermediate forms are seen. Additionally, in all of our spectra, the 30s peak is clearly seen although there is some slight variation in the peak position from spectrum-to-spectrum indicating the presence of nearby fragments. The 30s sub-unit is known to be much more stable than either the 50s or 70s sub-unit, in agreement with the repeated dominance of the 30s peak under different sample conditions.

Figures 34a and 34b show spectra acquired from purified 70s ribosomes that were sprayed (a) or pipetted (b) onto the LIAD substrates. In an attempt to improve the stability of the whole 70s ribosomal complex, some of the samples were exposed to UV light in a microscope. Various exposure times were used, 15, 30, and 60 minutes for the blue, green, and red curves, respectively. The longest exposure time (red), shows a marked increase in the relative intensity of high mass species, but considerable fragmentation still exists. The 30 minute exposure samples (green) show a reduction in high-mass intensity compared to the 15 minute exposure samples, suggesting there may have been additional complications with those specific samples and/or the cross-linking process.



Comparing the pipetted samples (Figure 34b) to the electrosprayed samples (Figure 34a) also shows a marked increase in the high-mass intensity across all exposure times. The 15 minute exposure time, pipetted sample (Figure 34b, blue curve) comes closest to the expected spectra (three dominant peaks representing the 30s, 50s, and 70s ribosomal units). This suggests that the electrospraying does induce fragmentation of the complexes, consistent with the above results for the proteasome complex. Additionally, the cross-linking was not wholly successful in preserving the 70s sub-unit, as done in [26]. More work is needed to improve the cross-linking procedure as 10 minutes was sufficient time for 70s preservation in the nano-ESI setup described in [26].

Shown in Figure 34c is the spectrum from a purified 50s sub-unit. While fragmentation is evident from the spectrum, there is a very large reduction in the intensity of mass species higher than the 50s value compared with the spectra in Figures 34a and 34b, as expected. Figure 34c also clearly identifies the 30s peak, which could be due to fragmentation of the 50s unit or insufficient purification during sample preparation. While some particles larger than the 50s unit remain, this is a clear indication that the measurements corroborate the presence or absence of the intended purified species.

Finally, all the spectra of Figure 34 exhibit peaks corresponding to the many intermediate forms of the ribosomal sub-units. It is not presently known whether these are native to the sample resulting from the ribosomal growth process or are the result of fragmentation effects during sample preparation. Independent means of measuring the entire ribosome using the same samples are not presently available but are under development.

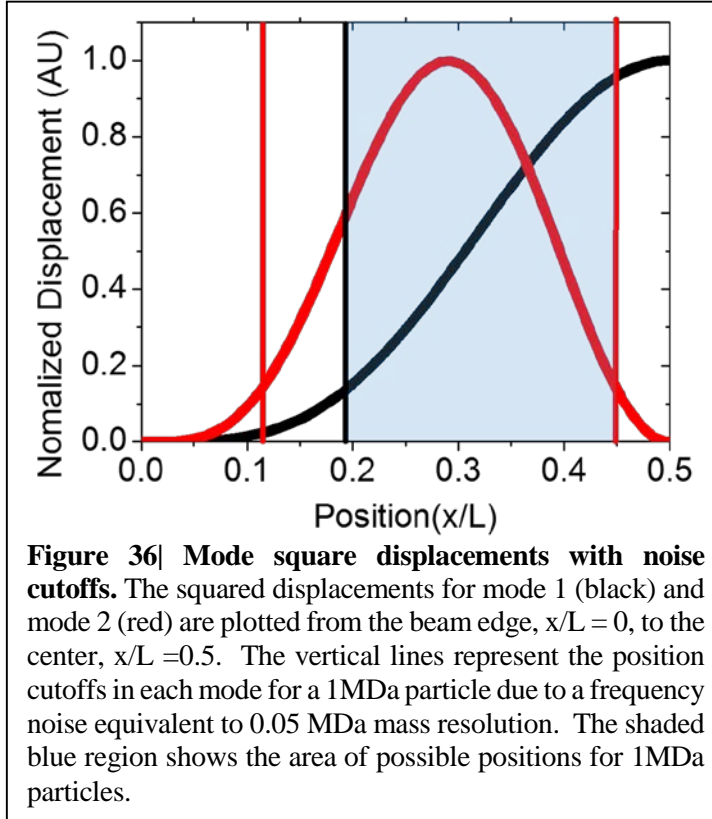
The final protein complex measured with the LIAD-NEMS system is the RAG complex (forthwith referred to simply as RAG). RAG is a protein complex responsible for folding DNA and plays a critical role in cellular transcription and replication. Structurally, RAG is composed of two sub-units, R1 and R2, with masses of 120 and 60 kDa, respectively. The entire RAG structure (360 kDa) consists of two of each of the sub-units. During preparation, the RAG complex can form as

various oligomers of the entire base unit. Complicating a mass analysis, however, is the fact that the RAG complex can sometimes form with or without an additional R2 unit. Thus, for example, a monomer of the entire RAG complex can have three possible mass species: (2)R1 + (1)R2 (300 kDa), (2)R1 + (2)R2 (360 kDa), and (2)R1 + (3)R2 (420 kDa). Oligomers of this monomeric complex will have similar permutations. The R2 mass of 60kDa is only just above our mass resolution so these species are likely blurred together in the mass spectra.

The spectrum shown in Figure 35 displays peaks, “A” and “B” at masses of 0.72 and 1.44 MDa ( $\pm 0.05$  MDa), respectively. These values correspond exactly with the theoretical mass of the dimer and tetramer of whole complex (without R2 subtractions or additions). There are no peaks, however, at the expected monomer mass indicating that these proteins were grouped either in solution or bunched during sample preparation. There are various features, or “shoulders” in the spectrum both below peak A and between peaks A and B. These likely correspond to the various permutations of the complex under addition or subtraction of an extra R2 sub-unit. As compared to the proteasome and ribosome complexes, there is not as much observed fragmentation in the RAG spectrum. This may reflect an increase in structural stability in the RAG complex as compared to the proteasome and 70s ribosomal complexes.

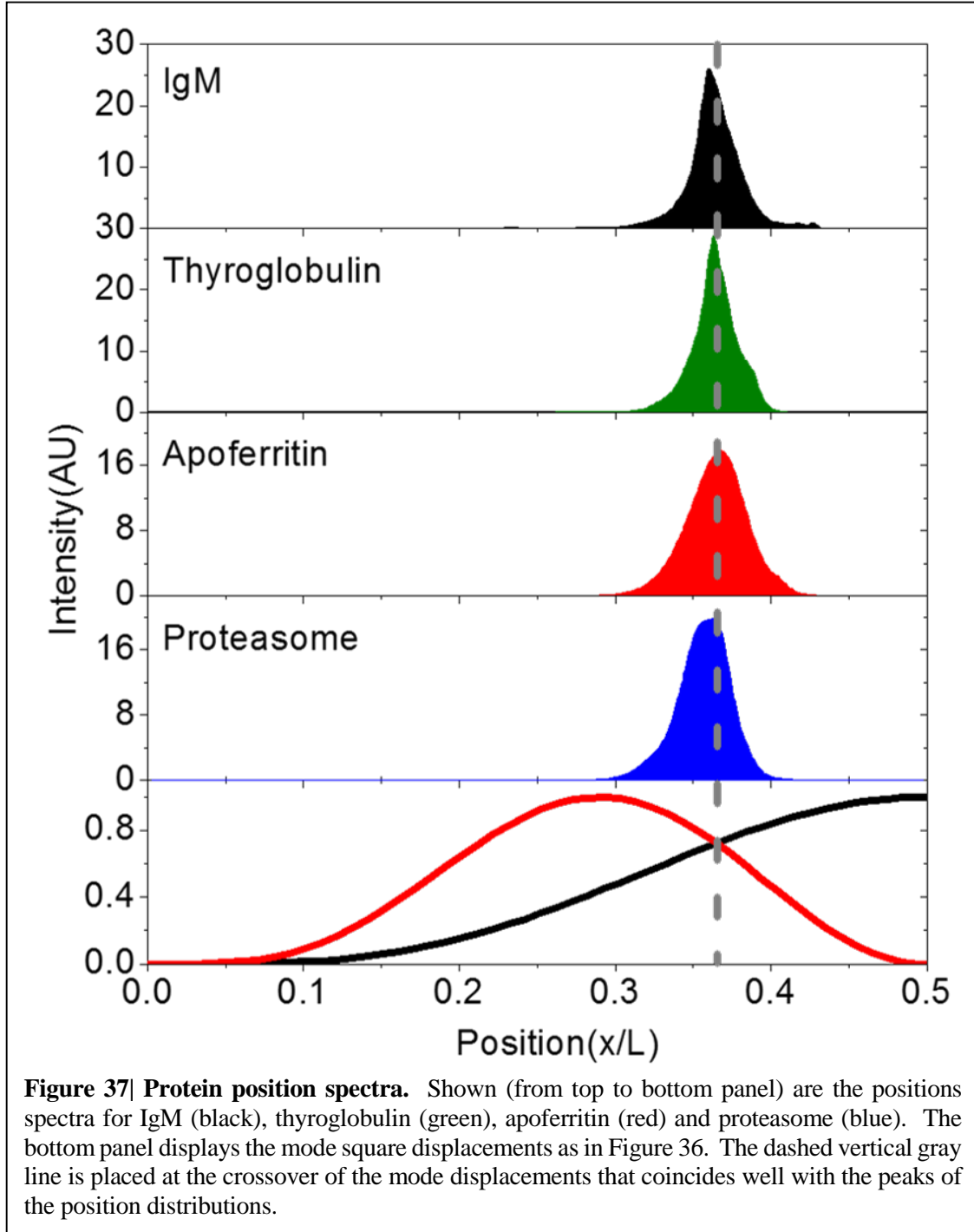
## 4.9 Discussion: protein mass spectra

All the protein mass spectra herein presented demonstrate the success of LIAD-NEMS in desorbing and detecting protein species via single-particle measurement. While each individual spectrum can be well identified with *a priori* knowledge of the sample, the combination of bunching and fragmentation effects would complicate attempts to identify an unknown species. This is in part due to the fact that all these spectra occur within a small mass range of 0.5-3MDa, compared to the detectable range of the device of 0.15MDa – 1GDa.



Regarding the spectra of single-sub-unit complexes, Figures 29-31, the sub-unit mass could be calculated from the spectra with a better signal to noise ratio (SNR). Although a 1MDa protein detected on our system has a SNR of 20, the difference between neighboring isoforms has an SNR of only  $\sim 4$  in the case of IgM, and  $\sim 3$  in the case of thyroglobulin. A better mass resolution, therefore, would

easily distinguish nearby peaks with a repeatable mass difference that could be used to extract the sub-unit mass even in cases with bunching.



The fragmentation of the proteasome and ribosome spectra (Figures 33 and 34), while presenting difficulties for discovery-mode mass spectrometry, nonetheless presents a useful tool for examining these complexes and the modification of their sub-units. The effects of different sample

preparation conditions on the degree of fragmentation suggest that the cause of the fragmentation is sample preparation before insertion into the vacuum chamber, and not the LIAD process itself. This is further supported by a lack of fragmentation seen in other measured protein species. Additionally, LIAD is widely used in the community over a range of analyte masses both less than and greater than the ones in the present study [10-14].

Nonetheless, significant work remains to improve the sample preparation procedure to reduce fragmentation and bunching effects. This includes refining the electrospray process to reduce the voltage while allowing for better drying. A complication in the overall system is that, with only a single device used for detection, the samples require very high analyte concentrations in solution. Planned future work involves the installation of NEMS arrays with 100 devices possible in the near future. This will vastly increase the data collection and would allow for lower concentrations to be used that are more compatible with a more delicate electrospray process (smaller needles, lower voltage, and shorter drying times).

#### **4.10 Results: protein particle position analysis**

In addition to providing the mass of each particle as it arrives on the device, multimode theory also provides the position of the particle (due to beam symmetry, this position is distance from the edge to the center) [2]. As the protein plume (~ few mm in diameter) is much larger than the device (10  $\mu\text{m}$ ), particles are expected to land randomly along the device. Due to frequency noise, particles that land too close to a modal node produce a frequency response too small to be detected. This then limits the range of possible detectable positions for a given mass species. The exact range depends on the mass of the particle; a heavier particle will produce a larger frequency response at the same position.

This cutoff range is depicted in Figure 36, which plots the squared mode displacements of the first (black) and second (red) modes. The vertical lines represent the noise position cutoffs in each mode for a 1MDa particle with 0.05 MDa mass resolution due to frequency noise. When selecting frequency jump pairs to calculate mass and position, the criterion of selection requires that the jump in each mode is larger than a frequency-noise defined cutoff (a three-sigma cutoff is used here). For a fixed particle mass, this frequency noise will then correspond to a limiting position value defined by the mode shape. As seen in Figure 36, because mode 2 has a node at the center, this sets the position cutoff on the right. The position cutoff on the left is set by mode 1. The shaded blue region of Figure 36 indicates the possible region of the position spectrum produced in any given experiment (for 1MDa particles). For smaller particles, the blue region will shrink; for larger particles it will expand. Within this region, the particles should still arrive randomly on the device and thus a relatively flat distribution is expected within this region defined by the position-noise cutoffs.

What is seen from the data, however, is that the position spectra for all the protein experiments have a very narrow distribution and are highly peaked. This data is shown in Figure 37, which displays the position spectra from the IgM, thyroglobulin, apoferritin, and proteasome experiments. The other experiments displayed the same behavior, but only those 4 are shown for brevity. The bottom panel shows the squared mode displacements as in Figure 36. The gray line is set at the crossover point where the modes have equal displacement. The interesting result is that the peaks of the protein spectra are well aligned with the mode crossover point.

There are several possible explanations for this behavior. First, it could be a statistical result from the data analysis process, wherein the noise cutoffs are much smaller than anticipated. In that case, however, the distributions should still be relatively flat within the region of possibility and would not be peaked at the mode cross-over point. A second explanation is that this is the result of bunching effects (as discussed in chapter two). If multiple small particles land on the device, but the mass and

position is mistakenly calculated as coming from a single particle, the position “answer” is peaked around the crossover point. This is because, as the limit of uniform mass loading is approached, the modes tend to have relative frequency jumps of equal magnitude. Thus the position, which is determined by the ratio of the relative frequency jumps between the two modes, approaches the point where the two modes overlap. This explanation, however, cannot account for the mass data which shows peaks that well match expected values. While bunching may be present in a minority of events in the IgM, thyroglobulin, and some ribosome spectra, if the results were from random agglomerations of small particles, then the mass spectra would be similarly random and not well-matched to expected values.

The third and most well-supported explanation to account for these unpredicted results is that the particles are being moved along the beam to this point due to the 2-mode beam actuation. This is an instance of a phenomenon known as Chladni modes, first described in 1787 with sand particles on square plates. As the plates were excited with multiple fundamental harmonics (by, for example, drawing a violin bow across the plate edge), the sand particles would accumulate and trace out the nodal patterns resulting from a superposition of the various harmonics. More recently, this behavior has been studied in the context of nano-beads moving in a liquid environment on a micro cantilever [27] and simulations of atomic reorganization on a vibrating crystalline substrate [28]. Importantly, the latter study concluded that the atoms on a vibrating surface move to the energy minimizing position at the antinodes of the driven harmonics. In that study only one mode was actuated, but the results should hold for a superposition of modes. This is in contrast with canonical Chladni figures where the particles accumulate at the nodes, the points of least displacement.

The difference appears to depend on the dynamics of the potential energy model of the system. For sand particles on a plate, the node accumulation is due to interactions with the gravitational potential where the points of minimal change in potential energy occur at the nodes. For

atoms on a lattice, on the other hand, the authors conclude that the points of minimal change in energy potential are the points where the lattice experiences minimal stretching and strain, the antinodes [28]. Thus, a determination of whether the expected points of particle accumulation are the nodes or antinodes depends on the precise mechanism of protein binding to the vibrating surface.

For the proteins on a cooled Si nano-beam, a detailed protein-binding and friction model is not at hand. For the present case, the net displacement of the two modes and the position of the net nodes and antinodes are considered relative to the peaks of the protein position spectra.

First, it is necessary to estimate the relative displacement amplitudes of the two actuated modes. Following [29], for a beam wherein the dissipation is proportional to the beam velocity and the actuation frequency is close to the resonance frequency, the displacement amplitude,  $A_n$ , can be written:

$$A_n = \frac{\eta_n F_n}{M(\omega^2 - \omega_n^2 - i\omega^2 / Q_n)} \quad (4)$$

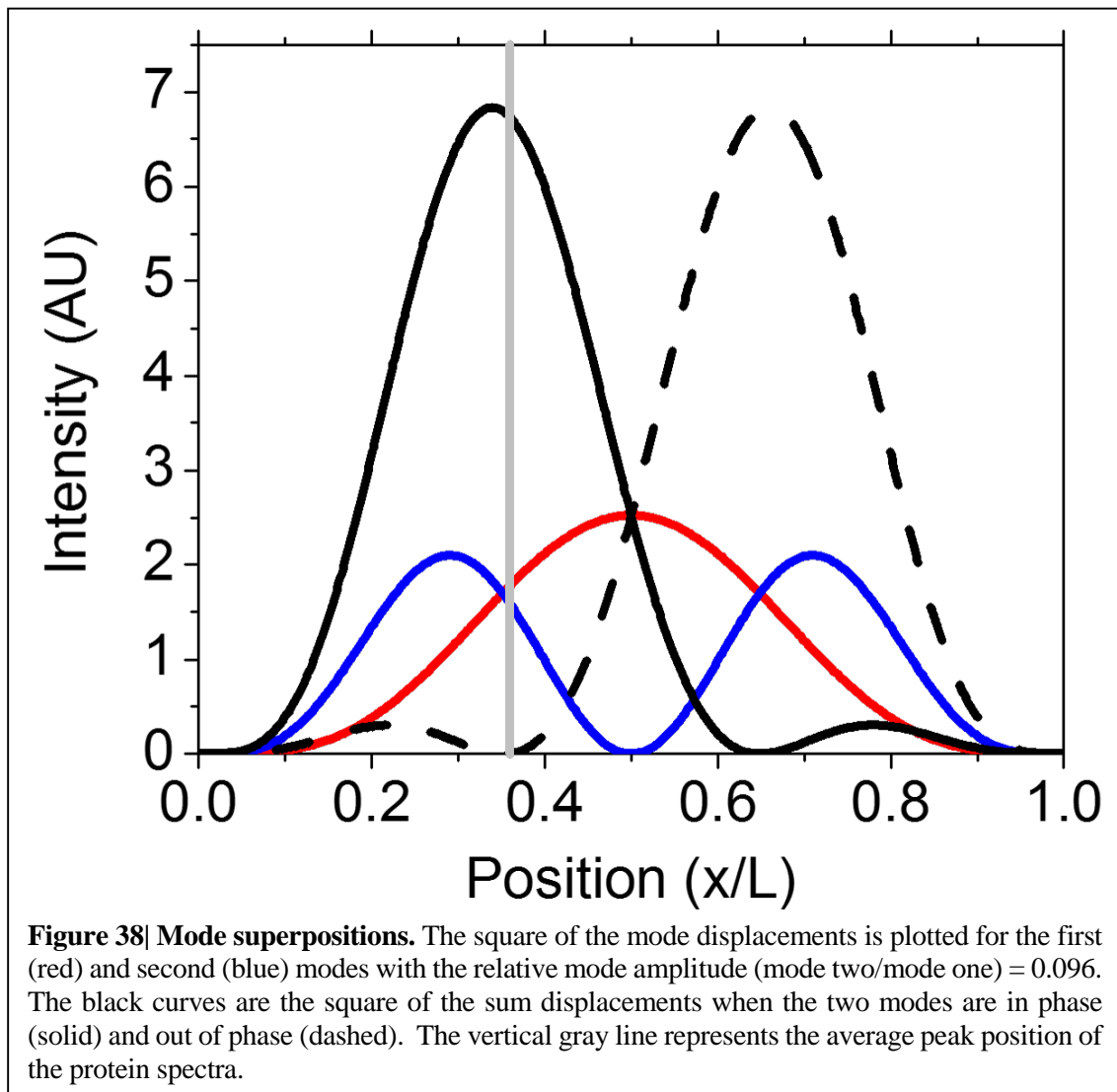
Where, for the  $n$ th mode:  $\eta_n$  is a numeric factor resulting from the integral of the mode displacement and the length of the beam along which the force is applied,  $F_n$  is the force amplitude (assuming the force is applied homogeneously as is the present case),  $M$  is the beam mass,  $\omega$  is the actuation frequency,  $\omega_n$  is the mode frequency, and  $Q_n$  is the dissipation quality factor. Our present calculation is concerned only with the ratio of  $A_1$  and  $A_2$  so one can write:

$$\frac{A_2}{A_1} = \frac{\eta_2 Q_2 F_2 \omega_1^2}{\eta_1 Q_1 F_1 \omega_2^2} \quad (5)$$

With the force being applied homogeneously along half of the beam, possessing equal quality factors (at 80K, we experimentally find the two modes have near equal quality factors), with the force magnitude proportional to the applied voltage squared (capacitive actuation), and modal frequencies

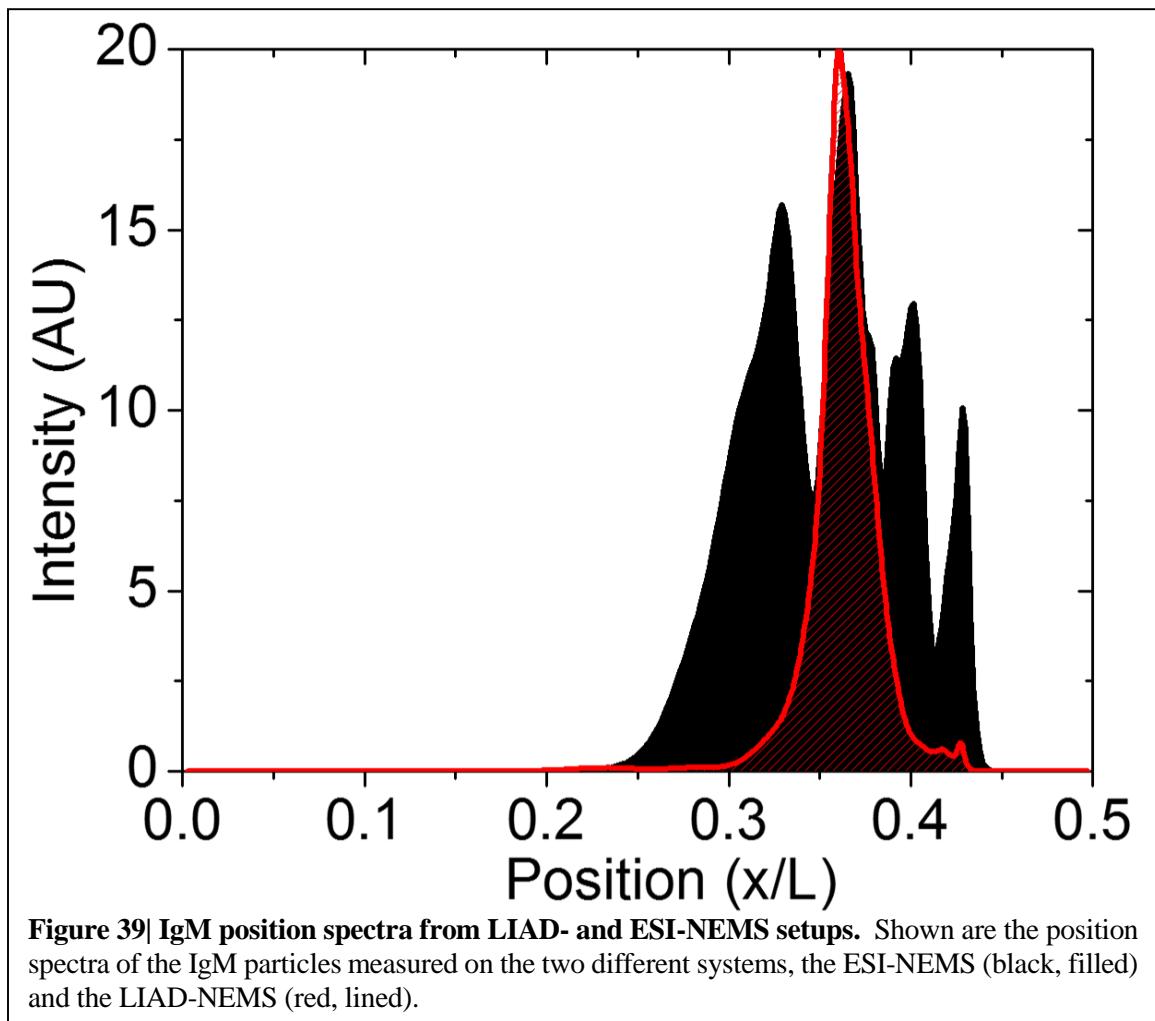
of 27.5 MHz and 72.5 MHz, respectively, the relative amplitude of the two modes is  $A_2/A_1 = 0.96$ . While this calculation could be refined and the relative displacements properly measured (canonically by, for example, measuring the thermomechanical noise), this provides a sufficient guide for the present situation.

Assuming this relative amplitude, the squared displacements of the individual modes and the superpositions are shown in Figure 38. If the two modes are in phase, the net squared displacement will appear as the solid black curve in Figure 38 while, for the out-of-phase case, the net squared



displacement seen by the proteins will be the dotted black line. In both cases, the node is the same position from the center and so our position spectra will appear the same in either case. Additionally, while the distance of the antinode from the center differs from the nodal distance from the center, the two are very close to each other. Thus, it is not possible at present to determine whether the particles are moving to the nodes or antinodes since the measured protein position spectra would look almost the same in either case.

Though this explanation has not been experimentally confirmed, there is additional experimental evidence in support of the theory. Figure 39 shows the position spectra of IgM particle measurements from the ESI- and LIAD-NEMS experimental setups. Though the ESI spectrum shows

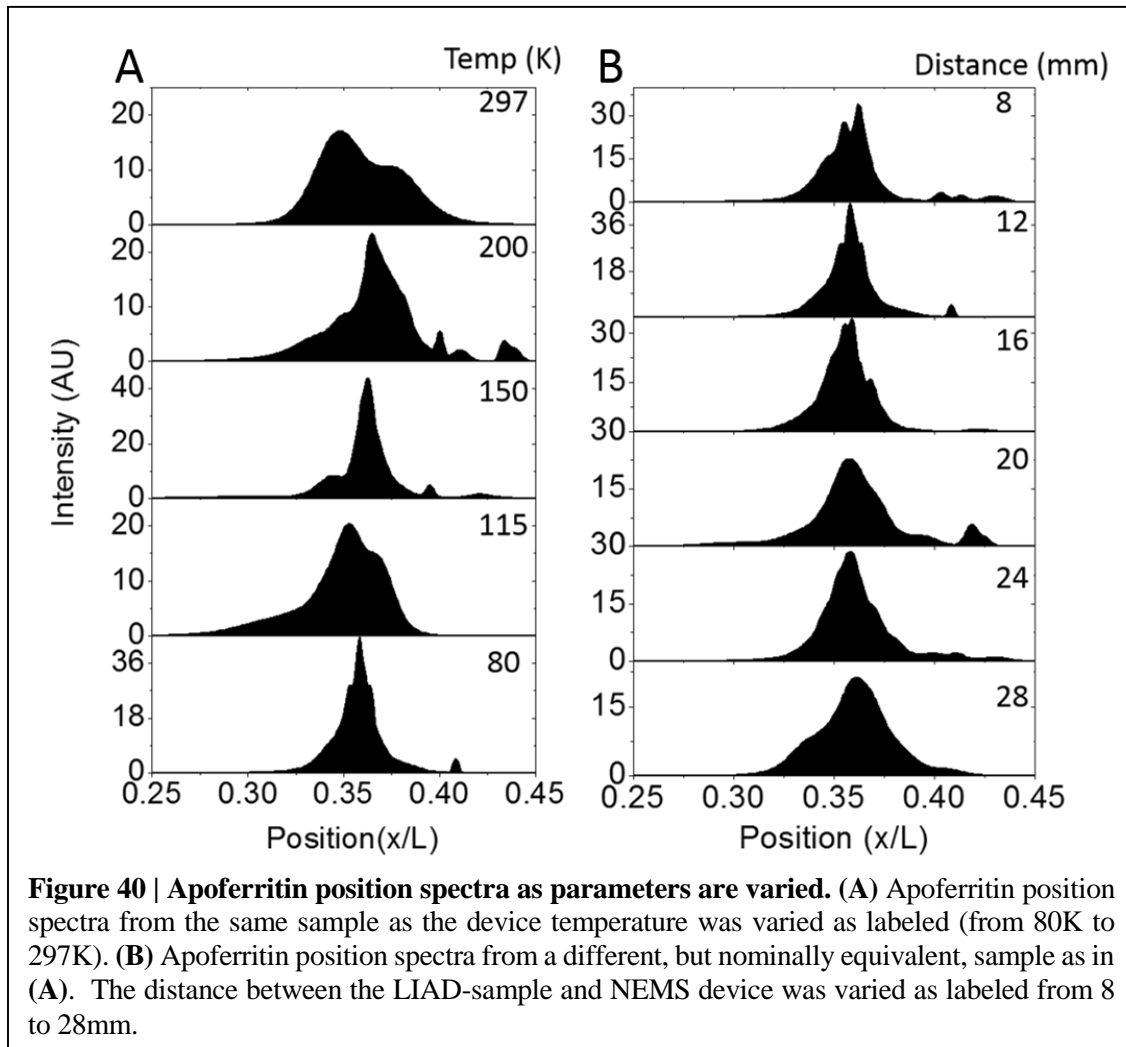


clear broadening, the centroids of the two spectra well overlap. There are some significant differences in the two systems that could account for this relative broadening. The ESI system is at higher pressure ( $10^{-6}$  vs.  $10^{-9}$  Torr), a different device surface orientation (horizontal versus vertical, relative to the gravitation field) and a lower particle kinetic energy. Again, without a specific model, definitive conclusions are difficult, but the overlap of the centroid in the two spectra indicates a mutual phenomenon, while the difference in widths indicates this phenomenon is related to experimental parameters and not data analysis.

Additional experiments were done with apoferritin to further explore this phenomenon; however, these were not conclusive. Shown in Figure 40 are panels of position spectra taken as two variables, device temperature and sample-NEMS distance, were varied. As seen in Figure 40a, the device temperature fails to correlate well with either increasing or decreasing the position spectral width. It was expected that varying the device temperature would vary the time constants involved in particle movement (if that is indeed occurring). Possibly, even at low temperature, the time scales are much smaller than the PLL time constant. Additionally, the particles arrive on the device at room temperature, so the diffusion is not simply related to the device temperature but also to the cooling process of the particles that occurs over some time scale.

Figure 40b similarly shows apoferritin position spectra as the sample-NEMS distance is varied. Again, there is no strong overall trend, although there does appear to be a very slight broadening as the distance is increased. This would be consistent with the bunching theory for the position spectra, but this effect is not strong enough to fully explain the data.

In sum, the Chladni effect – whereby the protein particles are transported to critical points determined by the mode superposition – is a reasonable explanation for the observed position data. There is as yet, however, insufficient data to confirm this effect. Future work to explore this phenomenon will involve modulating the relative mode amplitudes and phases. This modulation will



tune the position of the nodes and antinodes of the net displacement and, if the theory is correct, should similarly tune protein position spectral peaks. Additionally, reducing the PLL timescale may allow particle motion to be captured in real time from the temporal frequency data. It should be clarified that these position results do not affect the mass spectra, so long as the PLL timescale is longer than the timescales governing particle movement (which appears to be the case). The possibility of this surface phenomenon in the data represents an exciting opportunity to explore particle dynamics in the realm of NEMS sensing and opens a window into the utility of NEMS devices as a tool to probe surface-particle interactions.

## 4.11 Conclusion

Laser-induced acoustic desorption has been implemented in a NEMS-based mass spectrometry system for the real-time measurement of large, intact proteins and protein complexes. The viability of this LIAD-NEMS-MS system has been demonstrated through the acquired mass spectra of several different proteins and protein complexes that are built up, event-by-event, from the detection and measurement of individual particles, via a process described in chapter three. Proteins containing a single sub-unit, IgM, thyroglobulin, and apoferritin, have been measured and, for IgM and thyroglobulin, the isoform distributions have been analyzed and match expected values. Protein complexes containing multiple sub-units have also been successfully measured with sub-unit or oligomer masses well-correlated with expected values. This has been shown for the proteasome complex, ribosomes, and the RAG complex. Such an ability allows for the investigation of changes in sub-unit masses (due to growth conditions or mutations) and the relative stability of different sub-unit permutations, which can provide critical insight into protein structural formation and dynamics.

Construction and operation of this experimental system required significant upgrades to an existing laser-desorption-based NEMS-MS (details of this construction and operation are in chapters

two and three). Also required was the engineering of a LIAD substrate to maximize the laser-induced acoustic amplitude. This optimization is important not only for current operational utility, but for future efforts which will require a much larger desorption spot due to the implementation of macroscopically sized arrays of NEMS devices. Without substrate optimization, this would necessitate rapidly increasing amounts of laser power that may not be feasible in most experimental settings.

LIAD-NEMS-MS reveals important capabilities of NEMS-MS compared with conventional mass spectrometry systems. These include the ability to measure the mass of large proteins with high accuracy, and quantification of protein spectra at the single-particle level. Additionally, due to the ability to desorb and detect the proteins in a neutral manner, a LIAD-NEMS-MS system is optimally suited for Native-MS efforts and, with the future implementation of arrayed detectors, high-throughput mass spectrometry systems.

Additionally, LIAD-NEMS-MS exists as a next generation of NEMS-based mass spectrometry, removing the need for ion optics and differential pumping to enable an increase in overall flux rate with a single device from one event every 30 minutes to one event every second. As mentioned above, an important limitation of laser-desorption based NEMS-MS compared with the earlier ESI-NEMS-MS system is the inability to receive continual protein injection from solution and the necessity of sample plate preparation.

Finally, an interesting and unexpected phenomenon present in the data is explored. The position spectra, which represent an ensemble probability density function of the individual protein landing positions, reveal a much more narrow concentration than expected. The peaks of these narrow spectra are repeated across the different species and are well correlated with the nodal positions of the net displacements of the beam under simultaneous 2-mode actuation. This suggests that the protein particles, after landing at an initial random position on the NEMS device, are moved,

via the Chladni effect, to critical points defined by the nodes (or antinodes) of the net displacement. It is emphasized that this is one interesting possibility, but there is presently insufficient data to confirm this interpretation. Additional future experiments, which controllably vary the relative drive strengths and phases of the two modes and/or alter the surface chemistry interactions, are required to fully investigate this process.

Future work on the mass spectrometry aspects of the LIAD-NEMS-MS system will focus on improvements to the sample preparation process in order to reduce bunching and fragmentation effects induced by the system. Additionally, the implementation of arrayed NEMS devices will be undertaken to improve system throughput. This is critical for enabling many biological experiments which require the analysis of many different samples and higher statistical sampling efficiency.

## 4.12 Bibliography

1. Cole, R.B., *Electrospray and MALDI mass spectrometry: fundamentals, instrumentation, practicalities, and biological applications*. 2011: Wiley.
2. Hanay, M.S., et al., *Single-protein nanomechanical mass spectrometry in real time*. *Nature Nanotechnology*, 2012. **7**(9): p. 602-608.
3. Golovlev, V.V., et al., *Laser-induced acoustic desorption*. *International Journal of Mass Spectrometry*, 1997. **169**: p. 69-78.
4. Tam, A.C., et al., *Laser-Cleaning Techniques for Removal of Surface Particulates*. *Journal of Applied Physics*, 1992. **71**(7): p. 3515-3523.
5. Kolomenskii, A.A., et al., *Interaction of laser-generated surface acoustic pulses with fine particles: Surface cleaning and adhesion studies*. *Journal of Applied Physics*, 1998. **84**(5): p. 2404-2410.
6. Gupta, V., et al., *Measurement of Interface Strength by Laser-Pulse-Induced Spallation*. *Materials Science and Engineering a-Structural Materials Properties Microstructure and Processing*, 1990. **126**: p. 105-117.
7. Youssef, G., et al., *Inter-wafer bonding strength characterization by laser-induced shock waves*. *Journal of Applied Physics*, 2012. **111**(9): p. 094902-094902-4.
8. Ikeda, R., et al., *Laser spallation method to measure strength against Mode-I decohesion of CVD diamond films*. *Diamond and Related Materials*, 2005. **14**(3-7): p. 631-636.
9. Shea, R.C., et al., *Characterization of laser-induced acoustic desorption coupled with a Fourier transform ion cyclotron resonance mass spectrometer*. *Analytical Chemistry*, 2006. **78**(17): p. 6133-6139.
10. Shea, R.C., et al., *Design and characterization of a high-power laser-induced acoustic desorption probe coupled with a fourier transform ion cyclotron resonance mass spectrometer*. *Analytical Chemistry*, 2007. **79**(7): p. 2688-2694.
11. Gao, J.S., et al., *Laser-Induced Acoustic Desorption/Atmospheric Pressure Chemical Ionization Mass Spectrometry*. *Journal of the American Society for Mass Spectrometry*, 2011. **22**(3): p. 531-538.
12. Cheng, S.C., et al., *Using Laser-Induced Acoustic Desorption/Electrospray Ionization Mass Spectrometry To Characterize Small Organic and Large Biological Compounds in the Solid State and in Solution Under Ambient Conditions*. *Analytical Chemistry*, 2009. **81**(3): p. 868-874.
13. Peng, W.P., et al., *Charge-monitoring laser-induced acoustic desorption mass spectrometry for cell and microparticle mass distribution measurement*. *Angewandte Chemie-International Edition*, 2007. **46**(21): p. 3865-3869.
14. Peng, W.P., et al., *Laser-induced acoustic desorption mass spectrometry of single bioparticles*. *Angewandte Chemie-International Edition*, 2006. **45**(9): p. 1423-1426.
15. Heck, A.J.R., *Native mass spectrometry: a bridge between interactomics and structural biology*. *Nature Methods*, 2008. **5**(11): p. 927-933.
16. Kaddis, C.S., et al., *Sizing large proteins and protein complexes by electrospray ionization mass spectrometry and ion mobility*. *Journal of the American Society for Mass Spectrometry*, 2007. **18**(7): p. 1206-1216.
17. Tuomikoski, S., et al., *Preparation of porous n-type silicon sample plates for desorption/ionization on silicon mass spectrometry (DIOS-MS)*. *Lab on a Chip*, 2002. **2**(4): p. 247-253.

18. Greving, M.P., G.J. Patti, and G. Siuzdak, *Nanostructure-initiator mass spectrometry metabolite analysis and imaging*. Analytical Chemistry, 2011. **83**(1): p. 2-7.
19. Yuan, J. and V. Gupta, *Measurement of Interface Strength by the Modified Laser Spallation Technique .1. Experiment and Simulation of the Spallation Process*. Journal of Applied Physics, 1993. **74**(4): p. 2388-2404.
20. Gupta, V. and J. Yuan, *Measurement of Interface Strength by the Modified Laser Spallation Technique .2. Applications to Metal-Ceramic Interfaces*. Journal of Applied Physics, 1993. **74**(4): p. 2397-2404.
21. Yuan, J., V. Gupta, and A. Pronin, *Measurement of Interface Strength by the Modified Laser Spallation Technique .3. Experimental Optimization of the Stress Pulse*. Journal of Applied Physics, 1993. **74**(4): p. 2405-2410.
22. Inobe, T., et al., *Defining the geometry of the two-component proteasome degron*. Nature Chemical Biology, 2011. **7**(3): p. 161-167.
23. Schrader, E.K., K.G. Harstad, and A. Matouschek, *Targeting proteins for degradation*. Nature Chemical Biology, 2009. **5**(11): p. 815-822.
24. Nomura, M., *Assembly of Bacterial Ribosomes*. Science, 1973. **179**(4076): p. 864-873.
25. Bunner, A.E., A.H. Beck, and J.R. Williamson, *Kinetic cooperativity in Escherichia coli 30S ribosomal sub-unit reconstitution reveals additional complexity in the assembly landscape*. Proceedings of the National Academy of Sciences, 2010. **107**(12): p. 5417-5422.
26. Rostom, A.A., et al., *Detection and selective dissociation of intact ribosomes in a mass spectrometer*. Proceedings of the National Academy of Sciences of the United States of America, 2000. **97**(10): p. 5185-5190.
27. Dorrestijn, M., et al., *Chladni figures revisited based on nanomechanics*. Physical Review Letters, 2007. **98**(2).
28. Taillan, C., N. Combe, and J. Morillo, *Nanoscale Self-Organization Using Standing Surface Acoustic Waves*. Physical Review Letters, 2011. **106**(7).
29. Cleland, A.N., *Foundations of nanomechanics: from solid-state theory to device applications*. 2003: Springer Verlag.

## Chapter 5

# INERTIAL IMAGING WITH NANOMECHANICAL SYSTEMS

### 5.1 Introduction

Over the last decade, mass measurements using nanomechanical devices have been systematically improved to the point where they now offer interesting potential for new forms of mass spectrometry. Nanoelectromechanical systems (NEMS) are extremely sensitive to the added mass of adsorbed particles [1-5], and this has led to advances that include mass detection of single proteins [6, 7], nanoparticles [8], and large biomolecules [9, 10] as well as demonstrations of atomic [11-13] and sub-atomic [14] mass resolution. Given its capability for measuring neutral, single particles in both the low and high mass (>500 kDa) domains, NEMS-based mass spectrometry (NEMS-MS) is being pursued as a new analytical approach for proteomics, structural biology, and particle detection.

This chapter demonstrates a new methodology that further extends the capabilities of real-time, NEMS-based measurements of single molecules. It is shown that it is possible to simultaneously measure the mass, position, and shape of individual adsorbates – that is, to obtain their *inertial image* – using the multimodal frequency response of a mechanical resonator to the discrete molecular adsorption events. Below, this approach is validated by analyzing experimental data and by investigations using finite element modeling (FEM). Further inertial imaging with atomic-scale resolution is possible using advanced NEMS devices. In fact, there are no fundamental

diffraction-based limits to the resolution of this technique; instead stochastic frequency-fluctuation processes in the nanomechanical resonator impose the ultimate resolution limits. This contrasts with other imaging paradigms where wavelength dependent diffraction effects typically set resolution limits.

The theoretical work presented here is the result of an intense collaboration between myself, Professor John Sader (University of Melbourne, Australia), Dr. Mehmet Selim Hanay of the Roukes group, and Professor Michael Roukes.

## **5.2 Superpositions of resonator modes<sup>2</sup>**

In NEMS-MS, adsorption of an individual analyte on a nanomechanical resonator perturbs each of its vibrational modes differently; the mode shapes themselves give rise to a distinct position dependence of the adsorbate-induced frequency shifts [6]. For each mode, the analyte-induced frequency shift is maximal for adsorption at vibrational antinodes, whereas it vanishes at the nodes. Previous work (chapter three), employed two resonator modes to measure, simultaneously in real-time, the mass and position-of-adsorption of each analyte that adsorbed upon the NEMS [6].

Here it is shown that by employing a new method of analysis that incorporates additional resonator modes one can, in effect, obtain a spatially independent mass sensitivity. By extending this analysis, we further show that it is possible to image the spatial moments of the mass distribution for each adsorbate. Without loss of generality, this work explores the ultimate and practical limits to the sensitivity of this inertial imaging technique for small adsorbate masses, which do not perturb the resonator mode shapes. The analysis proceeds by defining what termed the moment generating functions,

---

<sup>2</sup> Equations are now renumbered starting with this chapter. The first equation in Chapter 5 is now equation 1.

$$F_n(\mathbf{r}) = \int_{\Omega} \rho(\mathbf{r}) \Phi_n^2(\mathbf{r}) dV. \quad (1)$$

Here,  $\Phi_n(\mathbf{r})$  are the unperturbed vibrational modes of the device – that is, those prior to analyte adsorption – and  $\rho(\mathbf{r})$  is the mass distribution for the adsorbed analyte; both are functions of the coordinates,  $\mathbf{r}$ , within the spatial integration region  $\Omega$ . Euler-Bernoulli beam mechanics [15] allows these  $F_n(\mathbf{r})$  to be directly related to the discrete, experimentally measured fractional-frequency shifts that are induced upon each analyte adsorption event,  $\Delta\omega_n = (\omega_n - \omega_n^{(0)}) / \omega_n^{(0)}$ . The analysis yields  $F_n(\mathbf{r}) = -2 \Delta\omega_n M \int_{\Omega} \Phi_n^2(\mathbf{r}) dV$ ; where  $\omega_n^{(0)}$  is the unperturbed frequency of the  $n$ th mode,  $\omega_n$  is the shifted resonance frequency after adsorption of the analyte, and  $M$  is the unperturbed device mass.

### Derivation of Equation. 1

Precipitous downward shifts in the mode resonance frequencies of a nanomechanical device occur during a particle landing event as in [6]. These measured frequency shifts are then used to calculate the mass, position, and shape of the particle attached to the NEMS. Importantly, in the limit where the particle mass is much less than the device mass, the sequential measurement of multiple particles is unaffected by the mass loading due to previous particles.

Previous work [6, 7] considered the particles as point-like masses with respect to the beam. Here, the individual particles are modeled as finite-sized objects with a (initially unknown) mass distribution along some length of the beam. First only Euler-Bernoulli beam theory regarding the device physics is assumed. Thus, this can be readily expanded to a variety of geometries and 2-dimensional devices. A generalized derivation is given here.

The resonance frequency for any unaltered harmonic oscillator can be calculated by equating the maximum kinetic and potential energies. Assuming that the additional particle is soft (the

Young's modulus of the beam remains unchanged), and the mass is much less than the beam mass, then the change in potential energy of the beam is much less than the change in kinetic energy and can be neglected. Using  $\rho_0$  as the unaltered, homogenous mass distribution of the beam, the frequency,  $f'$ , of the device after a particle landing event can be given as:

$$f' = \frac{1}{2\pi} \sqrt{\frac{U_n^{\max}}{\int_{\Omega} (\rho_0 + \rho(\mathbf{r})) \Phi^2(\mathbf{r}) dV}} \quad (2)$$

Now, using the assumption,  $\rho(\mathbf{r}) \ll \rho_0$ , the resonance angular frequency of the  $n$ th mode,  $\omega_n$ , is:

$$\omega_n^2 \approx \frac{U_n^{\max}}{\int_{\Omega} \rho_0 \Phi_n^2(\mathbf{r}) dV} \left[ 1 - \frac{\int_{\Omega} \rho(\mathbf{r}) \Phi_n^2(\mathbf{r}) dV}{\int_{\Omega} \rho_0 \Phi_n^2(\mathbf{r}) dV} \right] \quad (3)$$

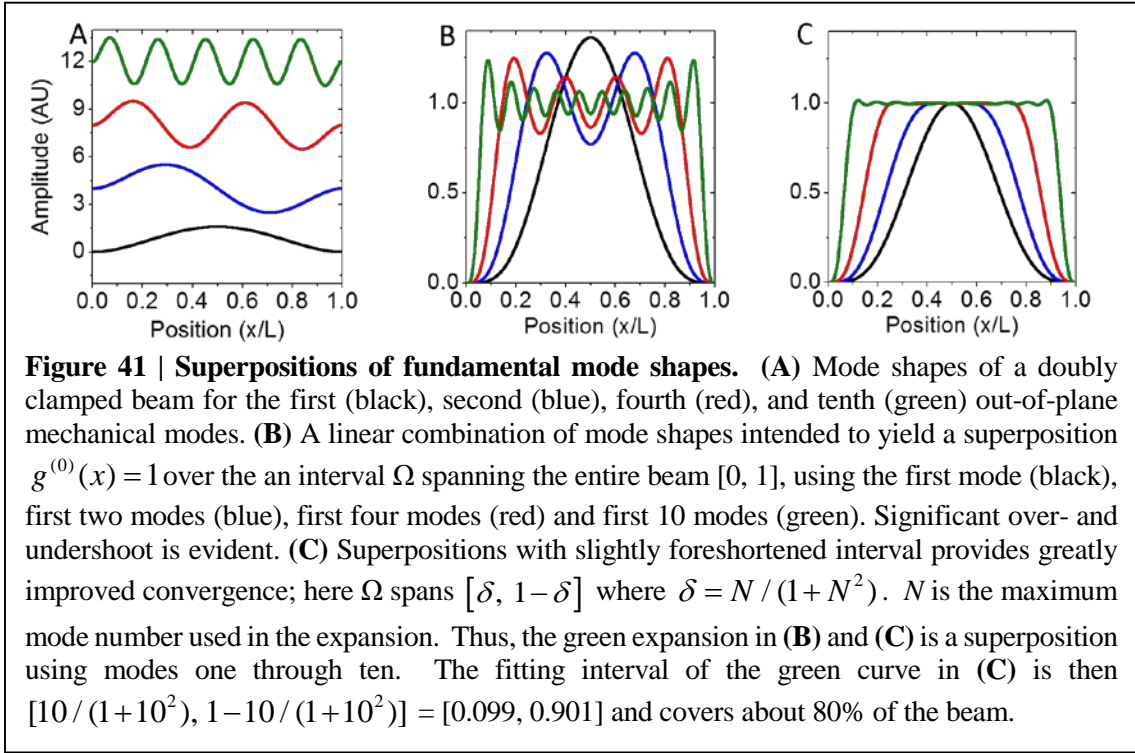
Taylor expanding around  $\rho(\mathbf{r})$  then gives a relative angular frequency of:

$$\frac{\omega_n}{\omega_n^{(0)}} = 1 - \frac{\int_{\Omega} \rho(\mathbf{r}) \Phi_n^2(\mathbf{r}) dV}{2 \int_{\Omega} \rho_0 \Phi_n^2(\mathbf{r}) dV} \quad (4)$$

Where  $\omega_n^{(0)}$  is the native, unloaded resonance frequency of the  $n$ th mode. Now, the total frequency shift due to the particle landing is:

$$\Delta\omega_n = \frac{\omega_n - \omega_n^{(0)}}{\omega_n^{(0)}} = - \frac{\int_{\Omega} \rho(\mathbf{r}) \Phi_n^2(\mathbf{r}) dV}{2M \int_{\Omega} \Phi_n^2(\mathbf{r}) dV} \quad (5)$$

This immediately gives Eq. (1) as a function the measured frequency shifts and the unperturbed device mass.



Eq. (1) indicates the relevance of these moment generating functions: the  $F_n(\mathbf{r})$  are weighted spatial averages of the analyte's mass distribution function. It follows, then, that it is possible to deduce moments of the analyte's mass distribution,  $m^{(k)}$ , by forming linear combinations of these moment generating functions,

$$m^{(k)} = \sum_{n=1}^N \alpha_n^{(k)} F_n = \int_{\Omega} \rho(\mathbf{r}) g^{(k)}(\mathbf{r}) dV \quad (6)$$

Here,  $g^{(k)}(\mathbf{r}) = \sum_{n=1}^N \alpha_n^{(k)} \Phi_n^2(\mathbf{r})$  are superpositions of squares of  $N$  mode shapes, assembled using coefficients  $\alpha_n^{(k)}$  chosen in a specific manner, and  $k$  is the moment order.

For example, the adsorbate mass  $m$  can be deduced from Eq. (6) by picking a particular set of coefficients  $\alpha_n^{(0)}$  that creates a superposition ideally approximating  $g^{(0)}(\mathbf{r}) = 1$  over the integration region  $\Omega$ ; in this case  $\int_{\Omega} \rho(\mathbf{r}) dV = m \approx m^{(0)} = \int_{\Omega} \rho(\mathbf{r}) g^{(0)} dV$ . Similarly, creating the

superposition,  $g^{(1)}(\mathbf{r}) = x$ , to create  $m^{(1)}$ , yields the analyte's approximate center-of-mass –  $\mu_x = m^{(1)}/m^{(0)}$  – along coordinate  $x$ , which is proportional to  $\int_{\Omega} \rho(x) x dx$ ; in other words, its position-of-adsorption along  $x$  can be obtained. Continuing by creating higher expansions along direction  $x$ , one can form  $g^{(2)}(\mathbf{r}) = x^2$  to obtain  $m^{(2)}$ ; this allows deduction of the analyte's standard deviation along  $x$  (its average size in that coordinate),  $\sigma_x = \sqrt{(m^{(2)}/m^{(0)}) - (\mu_x)^2}$ . The moments thus calculated are in units where device dimension along  $x$  is normalized to unity.

Analogous relations yield higher spatial moments of the analyte's mass distribution along  $x$ , for example its skewness and kurtosis, which involve  $g^{(3)}(\mathbf{r}) = x^3$  and  $g^{(4)}(\mathbf{r}) = x^4$ , respectively. The skew of the distribution is given as  $\gamma_{1x} = [(m^{(3)}/m^{(0)}) - 3\mu\sigma_x^2 - \mu_x^3]/\sigma_x^3$ , and the kurtosis is  $\gamma_2 = m^{(4)}/(m^{(0)}\sigma_x^4)$ . The first three moments of an arbitrary mass distribution are derived explicitly for the case of a one-dimensional doubly-clamped beam in the Appendix.

Eq. (6) applies generally to mechanical devices of any geometry. The spatial dimensionality of the deduced moments of the analyte mass distribution arises from the spatial variation of the vibrational modes employed in the expansion (Eq. (6)). For example, the out-of-plane displacements of a doubly-clamped beam change with one spatial variable (along the longitudinal axis); accordingly such modes can provide moments of the adsorbate mass distribution along that one coordinate. Membrane resonators, for example, with vibrational mode shapes that vary in two dimensions, can provide two-dimensional moments of the adsorbate distribution. In the following analysis, we describe general one-dimensional relations for a doubly-clamped beam device.

Figure 41 presents mode shapes and superpositions for the out-of-plane displacements of a simple doubly-clamped beam of length  $L$ . Figure 41a depicts the first, second, fourth, and tenth mode shapes along the longitudinal coordinate,  $x$ . Figure 41b shows the superpositions used to

approximately yield  $g^{(0)}(x) \approx 1$  over the full length of the beam; these involve from one up to all  $N$  of the modes chosen, for  $N$  equal to one, two, four, and ten. The ideal coefficients,  $\alpha_n^{(0)}$  for the expansion of  $g^{(0)}$  are determined by a least-squares algorithm.

As in Figure 41c, Figures 42a, b, and c show the superpositions using modes one through four to extract the first, second and third moments, respectively. The red shading in Figure 42 indicates the measurement zone  $\Omega = [4/(1+4^2), 1/2]$ . As seen in the Appendix, due to beam symmetry only the first half of a doubly-clamped beam can be considered when creating the superposition for moments of higher order than zero. This is because those fitting functions are asymmetric across the beam length, while the mode shapes are symmetric about the beam midpoint. This forces the assumption that the adsorbates are entirely contained on one half of the beam or other. Other devices without this symmetry, such as cantilevers, can measure adsorbates that span both halves of the device. In this work, the attention is focused on small particles much less than the span of the device. As seen in the bottom row of Figure 42, outside of the measurement zone the superposition (red) poorly approximates the ideal expansion (black).

Though the coefficients used in Figures 41 and 42 were calculated using a least-squares fitting algorithm, it can be shown rigorously that a unique analytic solution for these coefficients exists.

### **Proof of Unique Analytic Solution**

Continuing to assume the out-of-plane displacement modes of a doubly-clamped beam, performed is a least squares fit to the function,  $f_i(x)$ :

$$f_i(x) = x^i, \text{ for } i = 0, 1, 2, 3 \text{ (mass, 1}^{st}, 2^{nd}, 3^{rd} \text{ moments)} \quad (7)$$

This is done by creating a linear superposition of the squared mode shapes,  $\Phi(x)$ :

$$F_\alpha(x) = \sum_{n=1}^N \alpha_n \Phi_n^2(x) \quad (8)$$

Where  $\alpha_n$  are the coefficients to be evaluated. The least squares fitting then consists of the minimizing the function:

$$\delta(\alpha_1, \alpha_2, \dots, \alpha_n) = \int_{x_{\min}}^{x_{\max}} (F_\alpha(x) - f_i(x))^2 dx \quad (9)$$

Where  $x_{\min}$  and  $x_{\max}$  are defined by the measurement zone. The fitting condition for Eq. (9) is that  $\partial\delta/\partial\alpha_n = 0, \forall n \in [1, \dots, N]$ . Plugging Eq. (8) into Eq. (9) and solving for the derivative gives:

$$\frac{\partial\delta}{\partial\alpha_n} = 2 \left[ \sum_{m=1}^1 \alpha_m \int_{x_{\min}}^{x_{\max}} \Phi_n^2(x) \Phi_m^2(x) dx - \int_{x_{\min}}^{x_{\max}} f_i(x) \Phi_n^2(x) dx \right] \quad (10)$$

We now define two matrices:

$$\begin{aligned} T_{nm} &= \int_{x_{\min}}^{x_{\max}} \Phi_n^2(x) \Phi_m^2(x) dx \\ b_n &= \int_{x_{\min}}^{x_{\max}} f_i(x) \Phi_n^2(x) dx \end{aligned} \quad (11)$$

Now, eqn. (10) can be rewritten as:

$$\frac{\partial \delta}{\partial \alpha_n} = 2 \left[ \sum_{n=1}^N T_{nm} \alpha_m - b_n \right] \quad (12)$$

Setting eqn. (12) equal to zero, in matrix notation then:

$$T\alpha = b \quad (13)$$

Then, the coefficients are immediately solved for (since  $T$  is invertible) as  $\alpha = T^{-1}b$ . Thus, the superposition coefficients are indeed a unique solution to the least squares fitting problem, given choice of moment and measurement zone.

### 5.3 Residual error and adaptive fitting

The fidelity of the adsorbate's inertial image obtained is determined by how well the finite superpositions,  $g^{(k)}(\mathbf{r})$  in Eq.(6), converge to their intended spatial functions over the entire integration region,  $\Omega$ . For the specific case illustrated in Figure 41, involving one-dimensional modes

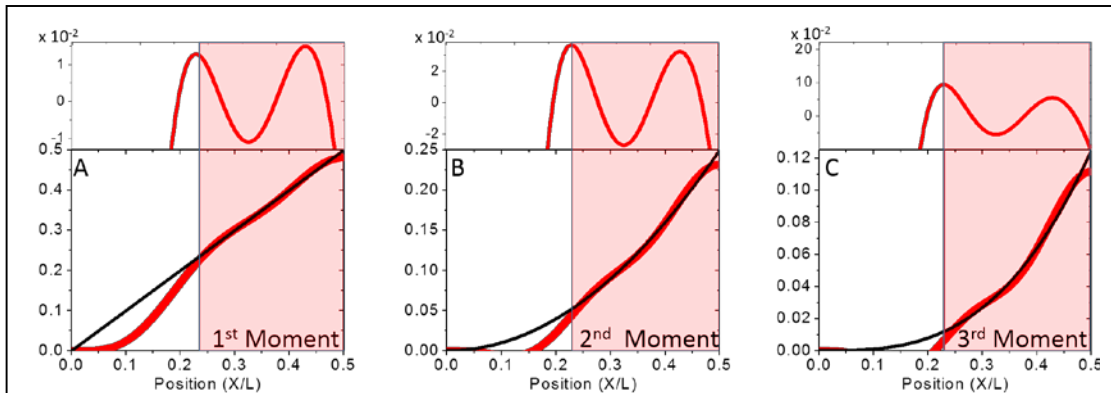


**Figure 42| Four-mode superposition functions to calculate the first three moments.**

Bottom row: Red curves are the superposition function as a linear combination of the mode shapes. These are created using the coefficients to calculate the first (A), second (B), and third (C) moments of the mass distribution of the particle. Red shading indicates the measurement zone used for these calculations ( $[N / (1+N^2), 1/2]$ ). The solid black curves represent the fitting functions. It is clearly seen the superpositions well match the fitting function within the measurement zone, but depart in the region (unshaded) outside the measurement zone. Top row: the residual of the superposition curves as approximations to the fitting function.

of a doubly-clamped beam, one seeks an expansion  $g^{(0)}(\mathbf{r}) \approx 1$  that is convergent over  $\Omega$ . Figure 41b shows the usual Gibbs phenomena (over- and under-shoot); this indicates that choosing  $\Omega$  to span the full beam length  $L$  is nonideal. This choice, in turn, will yield moments that poorly approximate those of the analyte mass distribution. Figure 41c shows that convergence is very significantly improved with the choice of a slightly foreshortened integration region. Practically, this foreshortened  $\Omega$  now defines the effective measurement zone – so such improvement comes at the cost of excluding a small fraction of experimental data from analytes that adsorb outside  $\Omega$ . When  $\Omega$  exceeds the actual size of an infinitesimal analyte, the residual fitting error,  $\varepsilon^{(k)}$  for the moment  $k$  varies with a power of the measurement zone,  $\varepsilon^{(k)} \propto \Omega^{N+1/2} / N!$ . Here,  $N$  is again the highest mode number used in the expansion.

The error is not exactly the same for all moments. As will be shown shortly, there is a prefactor in the above error expression that depends on a set of coefficients, different than the ones used above for the superposition of modes. These coefficients in the prefactor will depend on  $k$ , the moment order. The important result is that, within an order of magnitude, the moments will all have approximately the same error. One must be careful to remember, however, that the particle quantities are functions of several moments, and careful error propagation must be performed. For example, as shown above, the standard deviation,  $\sigma$ , is a function of  $m^{(0)}$ ,  $m^{(1)}$ , and  $m^{(2)}$ . So while  $\varepsilon^{(1)} \approx \varepsilon^{(2)}$ , the error or uncertainty in the standard deviation will generally be larger than the uncertainty in the center-of-mass position or the mass since the uncertainty in both mass and position propagate through in the calculation of standard deviation.

### **Derivation of Residual Fitting Error**

The fitting function, Eq. (7), is approximated by another function that is a linear superposition of mode shape squares:

$$h(x) = \sum_{n=1}^N \alpha_n \psi_n(x) \quad (14)$$

$\psi_n(x)$  is the response function for the  $n$ th mode, which is the square of mode shape:  $\Phi_n^2(x) = \psi_n(x)$

. These  $\alpha_n$  coefficients will now be solved for differently than was done above.

When approximating  $f(x)$  by  $h(x)$  the object is to minimize the squared-error within a measurement zone of  $2\Omega$  centered on the particle position,  $x_0$ . Removing the indexing,  $i$ , in the expression for the fitting function as this analysis applies equally to all values of  $f(x)$ , the squared error can be written as:

$$error^2 = \int_{x=x_0-\Omega}^{x=x_0+\Omega} [f(x) - h(x)]^2 dx \quad (15)$$

In practice, the measurement zone becomes a small fraction of the beam's length and we can safely assume that  $\Omega \ll 1$ . Since the integration zone is small, one can approximate both  $f(x)$  and  $h(x)$  using their Taylor expansions around  $x_0$ . For the target function, this expansion is

$$f(x) = \sum_{m=0}^{\infty} \frac{f^{(m)}(x_0)}{m!} (x - x_0)^m \quad (16)$$

Here,  $f^{(m)}(x_0)$  means the  $m$ th derivative of the function  $f(x)$  evaluated at point  $x_0$ .

One can write a similar expression for  $h(x)$ , which is a superposition of the response functions (Eq. (14)), so one can perform the Taylor expansion on each response function:

$$h(x) = \sum_{m=0}^{\infty} \sum_{n=1}^N \frac{\alpha_n \Psi_n^{(m)}}{m!} (x - x_0)^m \quad (17)$$

Now combining the Taylor expansions (16) and (17) in the error term (15), one obtains:

$$error^2 = \sum_{m=0}^{\infty} \frac{1}{m!^2} \left[ f^{(m)}(x_0) - \sum_{n=1}^N \alpha_n \Psi_n^{(m)}(x_0) \right]^2 \times \int_{x=x_0-\Omega}^{x=x_0+\Omega} (x - x_0)^{2m} dx$$

The integral is directly calculated as  $2\Omega^{2m+1} / (2m+1)$ . By using this value one obtains:

$$error^2 = \sum_{m=0} \frac{2\Omega^{2m+1}}{(2m+1)m!^2} \left[ f^{(m)}(x_0) - \sum_{n=1}^N \alpha_n \Psi_n^{(m)}(x_0) \right]^2$$

In this form, it is evident that each term in  $m$  gets smaller than the preceding term by a factor of  $\sim \Omega^2/m$ .

Since this occurs in the limit of small  $\Omega$ , ( $\Omega \ll 1$ ), the error can be minimized by eliminating the terms with small powers of  $m$ . To achieve this cancellation, one can eliminate the first  $N$  powers in  $m$ , which means from  $m = 0$  to  $m = N - 1$ :

$$error^2 = \sum_{m=0} \frac{2\Omega^{2m+1}}{(2m+1)m!^2} \underbrace{\left[ f^{(m)}(x_0) - \sum_{n=1}^N \alpha_n \Psi_n^{(m)}(x_0) \right]^2}_{\text{By adjusting } \alpha_n \text{ this term equals zero for } m \in [0, \dots, N-1]}$$

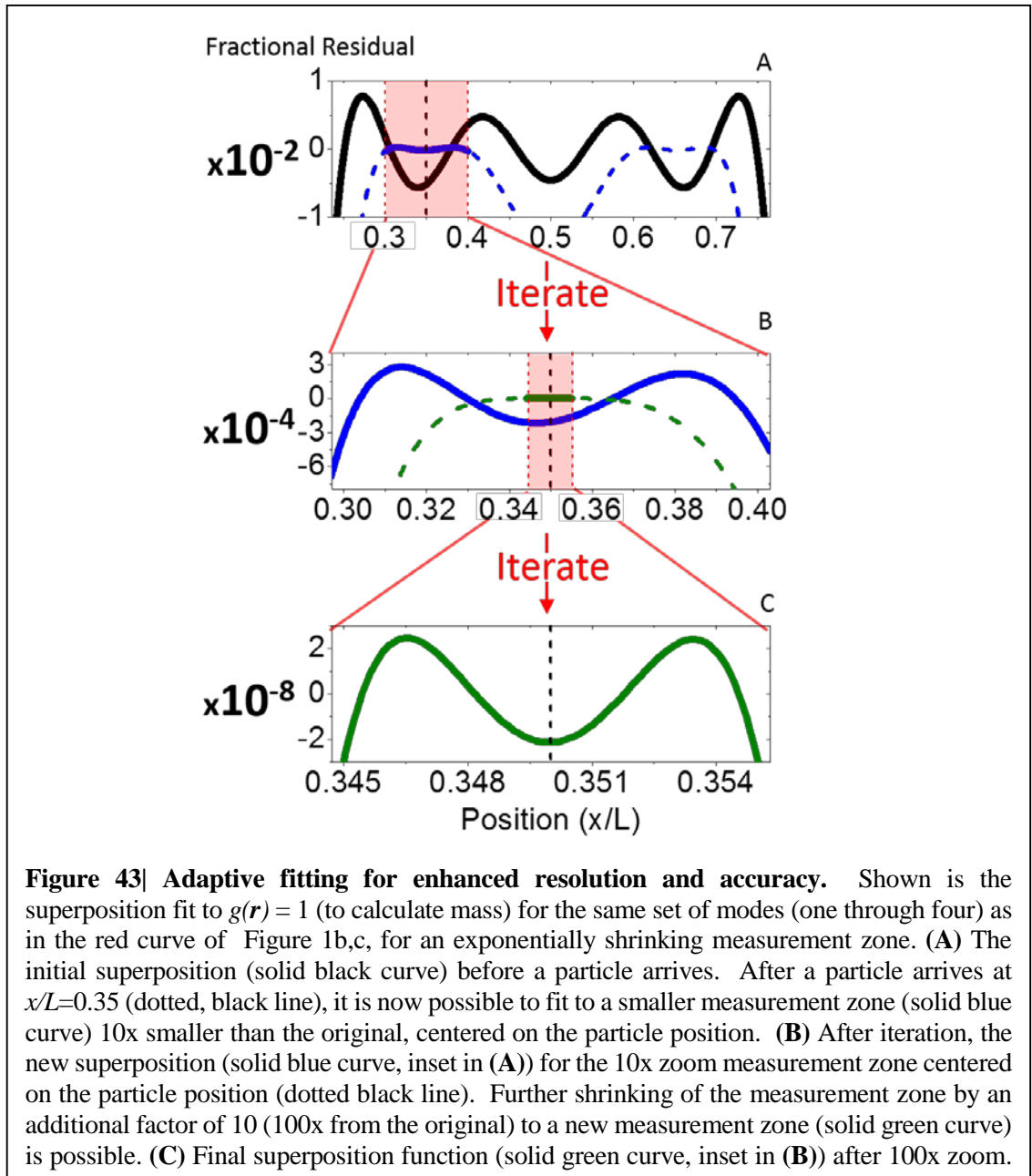
The linear system to be solved for is similar in format to Eq.(13):

$$\begin{bmatrix} \Psi_1^{(0)} & \Psi_2^{(0)} & \dots & \Psi_N^{(0)} \\ \Psi_1^{(1)} & \Psi_2^{(1)} & \dots & \Psi_N^{(1)} \\ \vdots & \vdots & \ddots & \vdots \\ \Psi_1^{(N-1)} & \Psi_2^{(N-1)} & \dots & \Psi_N^{(N-1)} \end{bmatrix} \begin{bmatrix} \alpha_1 \\ \alpha_2 \\ \vdots \\ \alpha_N \end{bmatrix} = \begin{bmatrix} f^{(0)} \\ f^{(1)} \\ \vdots \\ f^{(N-1)} \end{bmatrix} \quad (18)$$

Where the functions are meant to be evaluated at  $x = x_0$ . Solving this system for  $\alpha_n$  means that one eliminates the first  $N$  powers of  $\Omega$ , from  $\Omega^0$  to  $\Omega^{N-1}$ . The leading term in the error squared can now be written as:

$$error^2 = \frac{2\Omega^{2N+1}}{(2N+1)(N!)^2} \left[ f^{(N)}(x_0) - \sum_{n=1}^N \alpha_n \Psi_n^{(N)}(x_0) \right]^2 + \mathcal{O}(\Omega^{2N+3}) \quad (19)$$

The term in the bracket is determined by the solution of the linear system. Ignoring higher order terms:

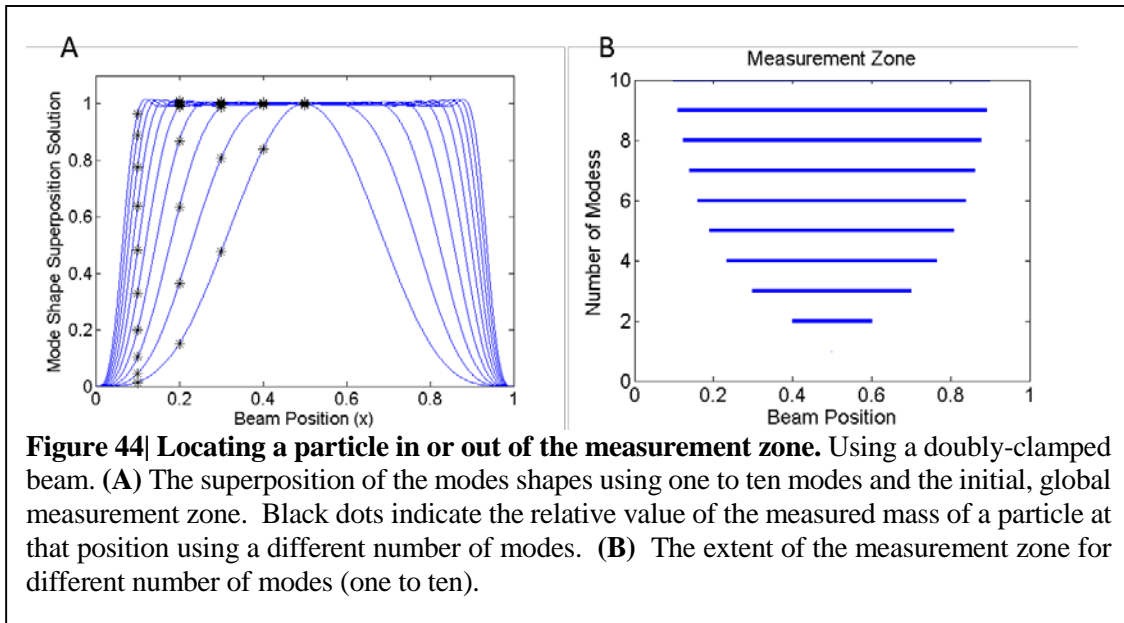


$$error \propto \frac{\Omega^{N+0.5}}{N!} \quad (20)$$

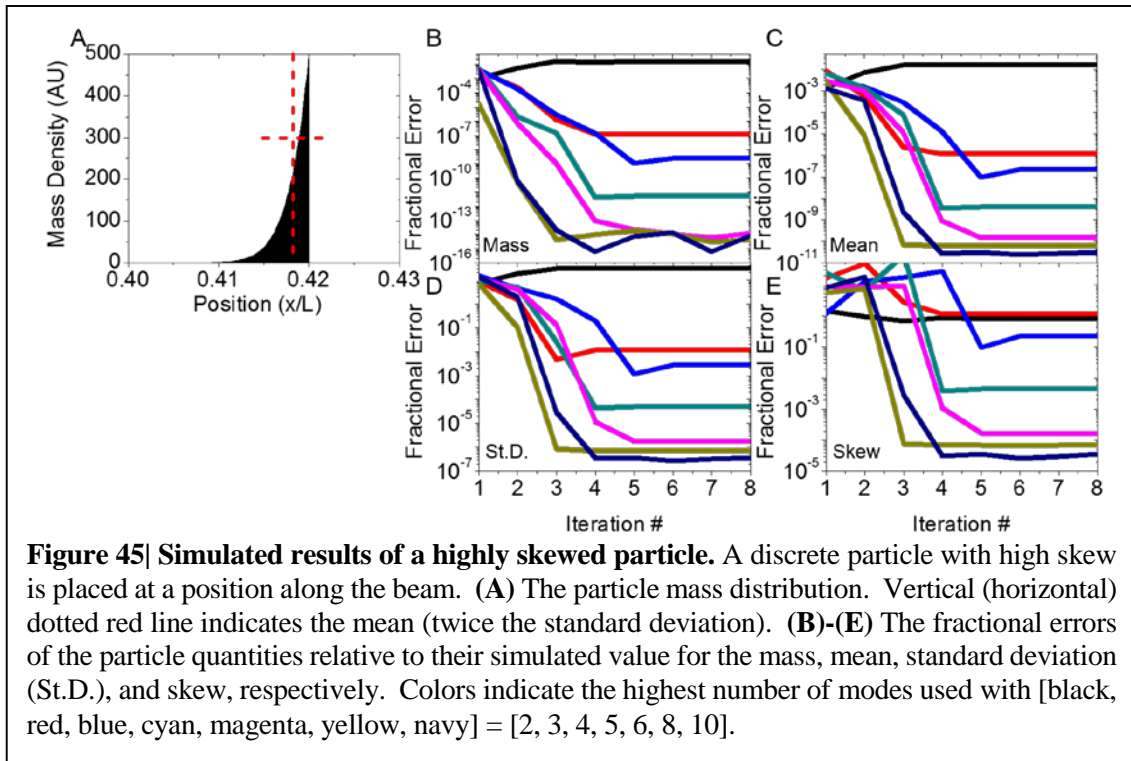
In general, analytes are typically quite small compared to the beam length; hence by adaptively fitting the measurement zone,  $\Omega$ , to the analyte the residual error in inertial imaging can be markedly decreased. This straightforward computational procedure can be carried out, without

loss of generality, *after* the adsorption-induced frequency shifts are acquired; no extra measurements are involved. Figure 43 demonstrates the concept: the expansion interval  $\Omega$  is iteratively shrunk around the position of the adsorbate, once its location is determined from the first pass of analysis. An exponential decrease in uncertainty is attainable; Figure 43 demonstrates a decrease in residual error by six orders of magnitude, as  $\Omega$  is ultimately reduced to a value somewhat larger than the size of the analyte. In practice, the random position for each adsorption event can initially be quickly determined by comparing data from the different device modes.

This experimental procedure – determining whether a randomly arriving particle lands in the measurement zone – is shown schematically in Figure 44 for the case of a point-like particle on a doubly-clamped beam. The procedure is readily expanded to larger particles by considering the mass and center-of-mass positions. For  $N$  measured frequency shifts, the mass of the particle can be calculated using  $[1, 2, 3 \dots N]$  number of modes, giving a set of  $N$  mass values:  $mass(n)$ . In Figure 44, the superpositions for  $N=1$  to 10 are shown. The mass values will have relative ratios dictated by the value of the  $n$ th superposition at different positions. Referring to Figure 44, a particle landing at the center is within the measurement zone of all the modes, and thus  $mass(n)$  is the same for all  $n \in$



[1, N]. The particle at  $x=0.4$ , however, is outside the first mode measurement zone. Here, then,  $mass(n)$  is only the same (within residual fluctuations) for  $n \in [2, N]$ . As the particle position is moved toward the clamping edge, it begins to move out of the measurement zone of the superpositions resulting from fewer modes. As seen in the left most position in Figure 44, the particle is now outside the measurement zone of all superpositions for  $N \leq 10$ . Thus, the criterion for being within the  $n$ th measurement zone is if  $mass(n)$  is the same for at least  $n=N, N-1$  (if not other values of  $n$  as well). If that condition holds, it can be assured the particle is within the  $N$ th mode measurement zone. If not, the event should be discarded. Figure 44 shows the empirical measurement zone,  $\Omega = \left[ \frac{N}{1+N^2}, 1 - \frac{N}{1+N^2} \right]$  for modes one through ten. As the number of modes is increased, the measurement zone expands, allowing for utilization of a larger area of the device. Note the measurement zone for one mode is a single point at  $x=0.5$ .



After validating that a particle has landed inside the measurement zone, it is found that adaptive fitting converges – that is, the residual error saturates at a minimum level – typically after less than ten iterations. Further, this procedure of convergent measurements over the full length of the beam becomes possible only if the initial measurements are sufficiently accurate such that convergence occurs to the correct region of the beam. This depends on the size and mass of a particle. For very light or small particles, an initial measurement zone – a subset of the entire device length – may be required, such that the initial set of particle measurements are of sufficient accuracy that the adaptive fitting procedure converges to the proper region of the beam. This adaptive fitting procedure is demonstrated for a simulated test particle on an ideal doubly-clamped beam. The results are shown in Figure 45.

Using an analytic expression for the mass distribution of a simulated particle (Figure 45), the frequency shifts induced on the out-of-plane displacement modes of a doubly-clamped beam

resonator were calculated. These frequency shifts are then used to estimate the mass, center-of-mass position, standard deviation, and skew of the particle using inertial imaging with adaptive fitting. The measurement zone used in the adaptive fitting procedure was  $\Omega = [\mu_i \pm 4\sigma_i]$ , where  $i$  denotes the iteration number. At each stage the measurement zone is shrunk from the initial, global region to a localized region around the particle according to the above formula. As the iterations are increased, the measurement zone shrinks to a small region around the particle wherein the particle quantities see reduced uncertainty.

As seen in Figures 45b-e, the fractional error usually saturates after 3-5 iterations of the adaptive fitting procedure, though numerics in the simulation may account for some of the fluctuations seen at low absolute values of the error. Additionally, as the number of modes is increased, the saturated error level is reduced, as expected. Of particular note are the curves using two modes (Figures 45b-e, black), which all experience increasing error during the adaptive fitting process. This is because, as shown below, two modes are insufficient to get size information, so the iterative measurement zone in effect “zooms in” on the wrong region of the beam.

## 5.4 Minimum number of modes

We can rigorously calculate the minimum necessary number of modes. To evaluate the  $k^{\text{th}}$  moment of the analyte mass distribution, a minimum of  $k+1$  modes must be measured. For example, as demonstrated previously [6], extracting average analyte mass (first moment) requires two modes. Increasing the  $\{\Phi_n(\mathbf{r})\}$  basis set in the expansions for  $g^{(k)}(\mathbf{r})$  beyond the minimum requisite  $k+1$  modes provides increased accuracy. The ultimate attainable resolution is determined by the frequency stability of the resonator modes, as will be described later. The minimum required number of modes is shown as follows.

Starting with the expression for the mode superposition,  $h(x)$  (Eq. (14)), the measurement zone,  $\Omega$ , is centered on the particle position,  $x_0$ , and spans the domain  $x_0 - \Omega \leq x \leq x_0 + \Omega$ . Shrinking the measurement zone to zero, then, formally corresponds to the limit of  $\Omega \rightarrow 0$ . To obtain an exact measurement in this asymptotic limit,  $h(x)$  must exactly represent the fitting function,  $f_i(x)$ . Proceeding as with the above uncertainty analysis,  $h(x)$  is expanded as a Taylor Series about  $x_0$ :

$$h(x) = \sum_{n=1}^M \frac{h^{(n)}(x_0)(x-x_0)^n}{n!} + O\left([x-x_0]^{M+1}\right) \quad (21)$$

### Mass

First consider the mass measurement, where the fitting function is  $f_0(x) = 1$ . If one chooses to use only a single device mode,  $N=1$ , then equating Eq. (21) to the fitting function gives:

$$1 = \alpha_1 \Psi_1(x_0) + O(x-x_0) \quad (22)$$

This has a solution,  $\alpha_1 = 1 / \Psi_1(x_0)$ . Thus, one mode is sufficient to represent the function  $f_0(x) = 1$  in the measurement zone. This is asymptotically exact in the limit,  $\Omega \rightarrow 0$ , since all higher order terms vanish. Thus,  $N=1$  allows exact evaluation of the mass as the size of adsorbed region goes to zero (the particle becomes point-like).

Using more than one mode, i.e.  $N=2$ , enables higher orders of the Taylor Expansion to be satisfied. Using 2 modes then, Eq. (22) becomes

$$1 = \alpha_1 \Psi_1(x_0) + \alpha_2 \Psi_2(x_0) + \{x-x_0\} \{ \alpha_1 \Psi_1'(x_0) + \alpha_2 \Psi_2'(x_0) \} + O\left([x-x_0]^2\right) \quad (23)$$

Equating powers of  $(x-x_0)$  yields the following system of equations:

$$\begin{aligned} 1 &= \alpha_1 \Psi_1(x_0) + \alpha_2 \Psi_2(x_0) \\ 0 &= \alpha_1 \Psi_1'(x_0) + \alpha_2 \Psi_2'(x_0) \end{aligned} \quad (24)$$

Which can be directly solved for  $\alpha_1, \alpha_2$ . Inclusion of yet more terms in the superposition, (Eq. (14)) enables a yet higher order of the Taylor expansion to be set to zero. However, these terms vanish in the asymptotic limit,  $\Omega \rightarrow 0$ , leaving the leading order (constant) term only. One can thus conclude that only one mode ( $N=1$ ) is required to measure mass.

#### *Position*

In this case, the required fitting function is now  $f_1(x) = x$ . Using only one mode, equating the Taylor expansion to the fitting function gives  $x = \alpha_1 \Psi_1(x_0) + O(x - x_0)$ , which has no solution. However, using two modes ( $N=2$ ) gives:

$$x = \alpha_1 \Psi_1(x_0) + \alpha_2 \Psi_2(x_0) + \{x - x_0\} \{ \alpha_1 \Psi_1'(x_0) + \alpha_2 \Psi_2'(x_0) \} + O([x - x_0]^2) \quad (25)$$

The solution is given by the system of equations:

$$\begin{aligned} 1 &= \alpha_1 \Psi_1(x_0) + \alpha_2 \Psi_2(x_0) \\ 0 &= \alpha_1 \{ \Psi_1(x_0) - x_0 \Psi_1'(x_0) \} + \alpha_2 \{ \Psi_2(x_0) - x_0 \Psi_2'(x_0) \} \end{aligned} \quad (26)$$

which is solvable. Consequently, the use of two modes is sufficient to asymptotically represent the fitting function  $f_1(x) = x$  in the measurement zone. Therefore,  $N=2$  allows for exact determination of the particle position, as the measurement zone vanishes. As in the case for the mass measurements, use of greater than two modes enables higher order terms in the Taylor expansion to be set to zero. Since these terms vanish in the asymptotic limit where the measurement zone vanishes, the use of only two modes enables an exact determination of position. Use of more than two modes has no effect in this limit.

#### *Standard Deviation, Skew*

A similar analysis can be applied to the high moments of the particle mass distribution such as standard deviation and skew, using the respective fitting functions,

$f_2 = (x - x_0)^2$ ,  $f_3 = \left(\frac{x - x_0}{\sigma}\right)^3$ . It is found that three modes are required for the standard deviation

and four modes are required for the skew.

Thus, the minimum of modes required to measure the  $k$ th moment is  $k+1$ . For point-like particles, use of additional higher order modes has no effect on the accuracy of the results.

## 5.5 Theory validation with experimental data and FEM simulations

Having provided a rigorous mathematical derivation, the methodology is now validated by analyzing data from two experimental studies. The first study measured single IgM antibodies using multimode theory and the first two driven, in-plane displacement modes of a doubly-clamped beam NEMS resonator [6]. In the second study, shifts in the resonance frequency of the first four out-of-

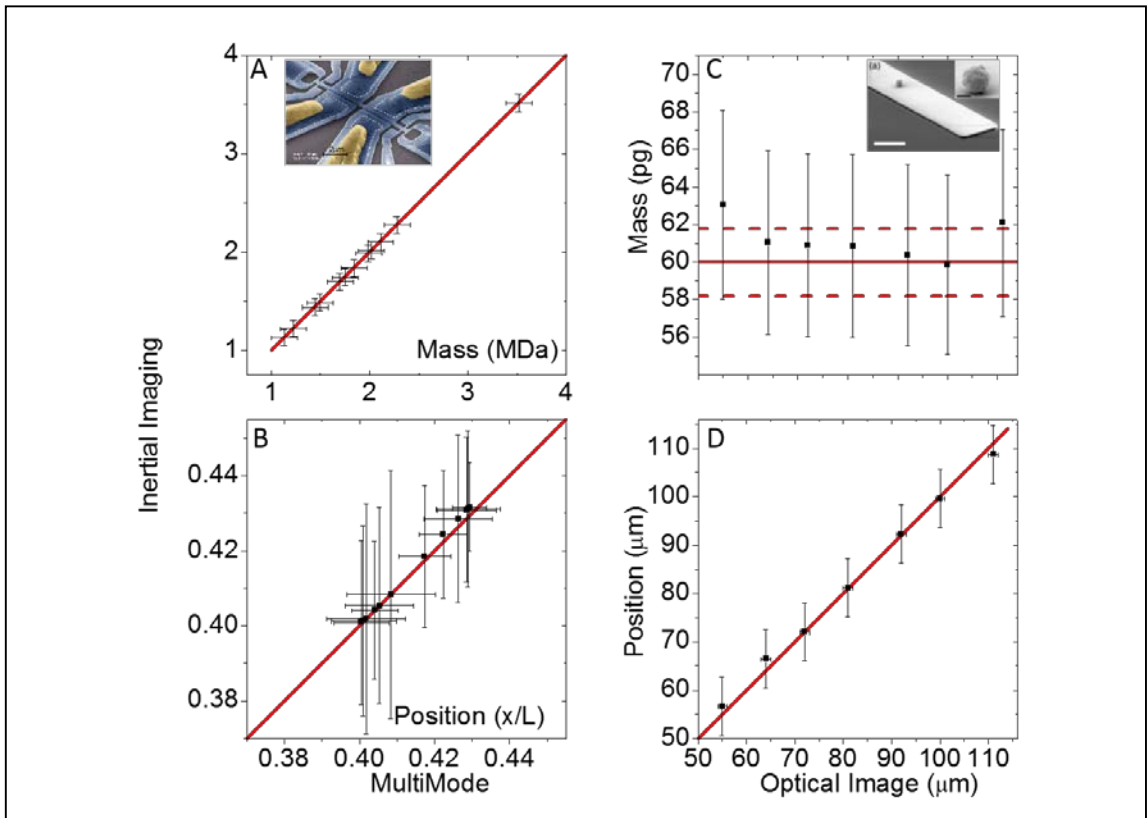
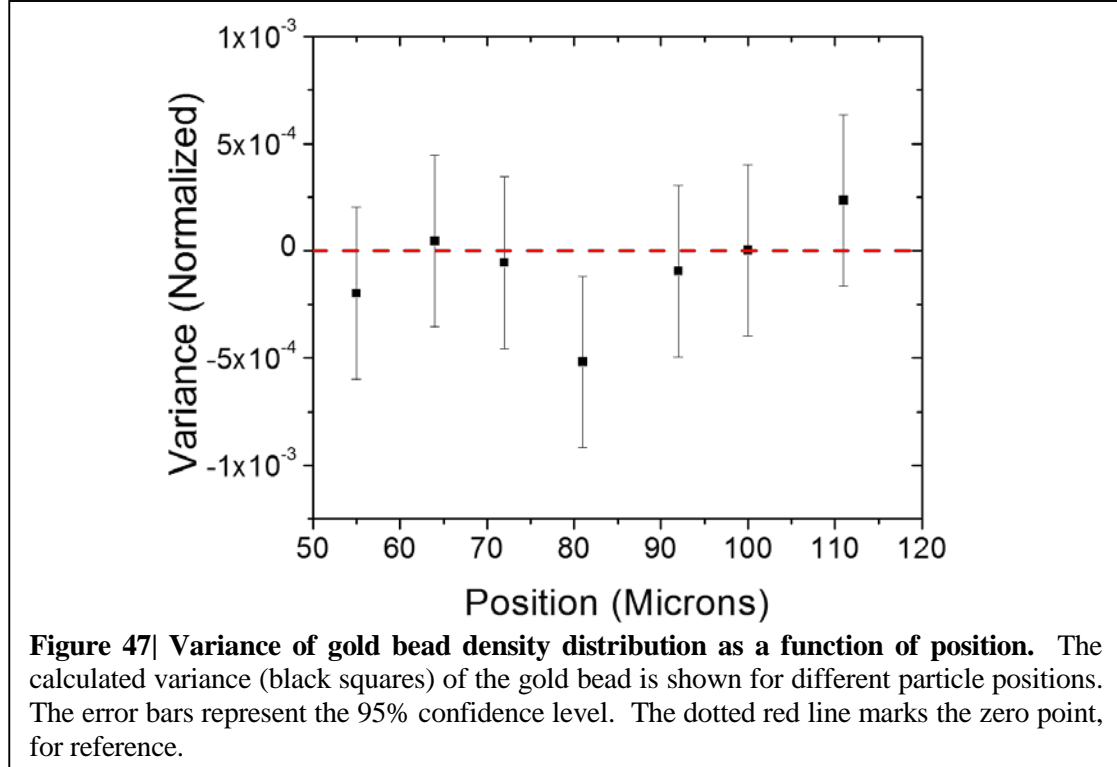


**Figure 46 | Inertial imaging using experimental data.** All error bars represent the two-sigma, 95% confidence level. **(A, B)** Mass and position calculations, respectively for the experimental data from using 2 modes of a doubly-clamped beam (reference 6). The values for mass and position are compared with the previous values from the paper using multimode theory. The error bars in superposition theory reflect the total error due to both the fitting residual and frequency noise. **(C)** Analysis of the particle mass for different positions using the four-mode measurement of the same particle along a cantilever device (reference 16). The particle expected mass is estimated from the SEM measurements of the paper (solid red line) with 2% assumed uncertainties in that measurement (dotted red lines). **(D)** Position calculation using the same data compared with the optically measured position. The red lines in **(A)**, **(B)**, and **(D)** represents curves of exact agreement between the two methods. Insets are electron micrographs of representative devices used in the two respective studies.

plane modes of a microscale cantilever device were measured as a gold bead was manually positioned, stepwise, along the device length [16].

The results of the analysis of the first study are shown in Figures 46a and 46b. The two-mode frequency jump data is used to calculate the mass (Figure 46a) and position (Figure 46b) of the particles using inertial imaging theory, and the results are compared to multimode theory [6]. The error bars along both axes (2-sigma, 95% confidence level) illustrate the effects of both experimental noise and, in the case of inertial imaging theory, the residual errors. Excellent agreement between inertial imaging theory and multimode theory is evident for deduced mass and position values.

Figures 46c and 46d compare the results of inertial imaging theory with the optical measurements of the position of the gold bead on the cantilever in the second study. Using the 4-mode frequency measurements reported in [16], the mass and position of the particle are calculated with inertial imaging theory. Figures 46c and 46d show that particle mass and position values obtained from inertial imaging provide excellent agreement with expected mass, as well as for the observed positions [16].

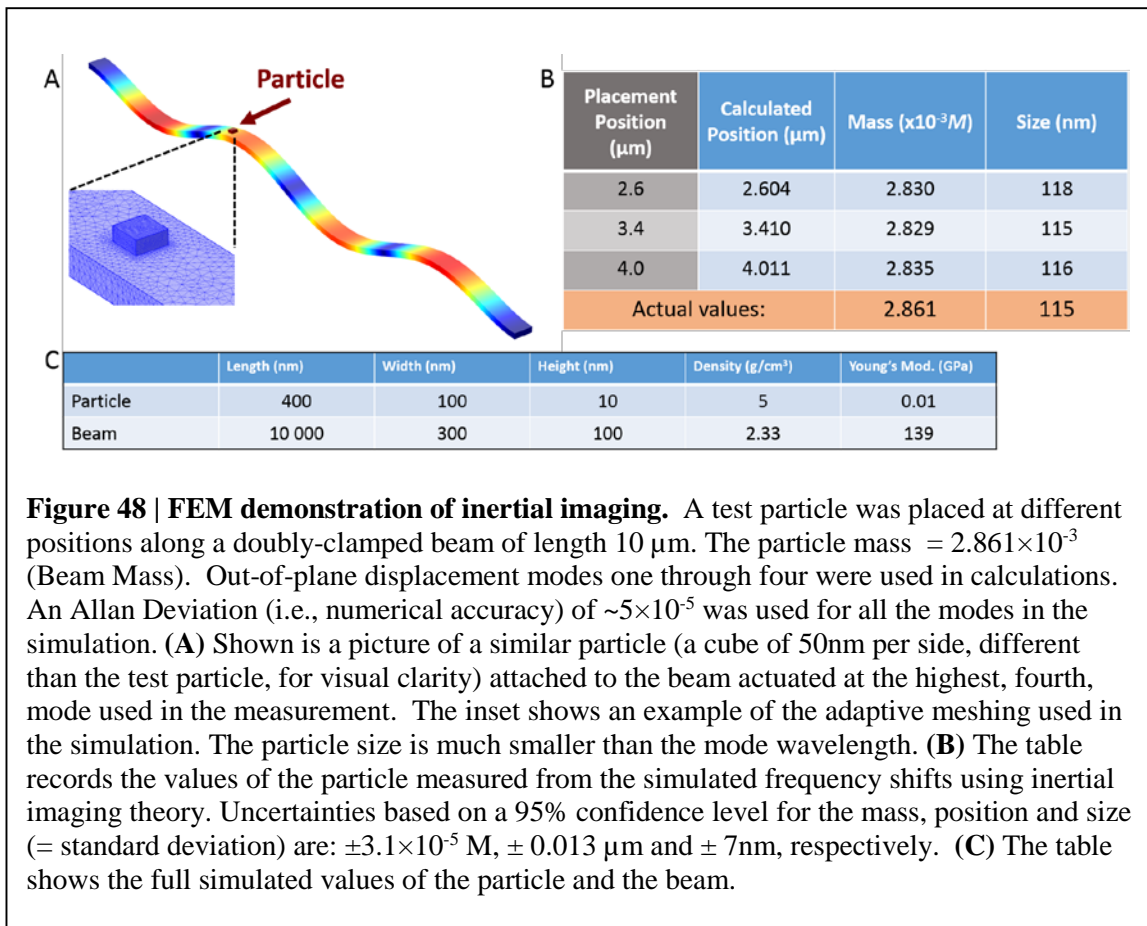


Evaluation of particle size from such existing experimental data is more difficult. The first data set includes only two modes and is, thus, insufficient to permit such analysis. The second data set, when analyzed for particle size, yields uncertainty comparable to the measured value itself because of the significant noise present in the data.

In Figure 47 is plotted the calculated variance using inertial imaging theory for the particle distribution from [16] at different positions. The variance is normalized to the beam length. Due to the large uncertainty in the measurements, some of the calculated variance values are negative. These measurements provide a mean value for the variance of  $-8.5 \times 10^{-5} \pm 1 \times 10^{-4}$  (mean  $\pm$  2s.d. /  $\sqrt{n}$ ). Physically, however, the variance must be positive. This estimate can be used to set an upper bound for the normalized variance of  $1.5 \times 10^{-5}$ . This in turn gives an upper bound for an estimate of the true size (radius) of the particle of  $\sqrt{1.5 \times 10^{-5}} \times 153 \mu\text{m}$  (length of the beam) =  $0.6 \mu\text{m}$ . Considering the

actual particle radius of  $0.9\ \mu\text{m}$  (SEM measurements of [16]), this estimated upper limit of  $0.6\ \mu\text{m}$  ( $2/3$  of actual particle size) is consistent with the point attachment of a rigid sphere to the cantilever.

To provide initial validation of inertial imaging for analyte size, FEM simulations are performed of the response of a device to a small test particle of specific mass, position, density, and shape. The results of this analysis are shown in Figure 48. A rectangular test particle that is much smaller than the wavelength of the highest mechanical mode is employed (Figure 48a). This test particle is positioned at various positions along a doubly-clamped beam device, and the first four out-of-plane displacement modes are used to calculate mass, position, size (=standard deviation of the particle in the direction along the main axis of the beam) of the particle by inertial imaging. As seen



in Figures 48b-d, the deduced values for the particle are all well within uncertainty of the expected values.

FEM simulations are a validating method for three dimensional modeling of realistic experimental systems. They are susceptible, however, to limits in computing power. Increasing the number of mesh elements would reduce the numerical uncertainty of the simulations. This is equivalent to reducing the frequency instability of a device in an actual measurement.

## 5.6 Ultimate resolution

In experiments there are practical limitations to the resolution that can be attained. Upon absorption, frequency shifts are induced by the physical attachment of the analyte to the resonator. If this adhesion is tenuous, the accuracy of the deduced properties of the analyte will be compromised. Soft analytes, such as proteins, will comply well with the surface topography as they physisorb due to Van der Waals forces. More rigid particles, such as metallic nanoparticles may instead reflect an inertially imaged size more representative of the (smaller) region of attachment; in this case patterning a compliant surface layer on the resonator may help extend the zone of adhesion to the full particle diameter.

Beyond such straightforward experimental issues, the primary source of uncertainty – and the ultimate limits to the resolution of inertial imaging – arise from the frequency instability of the resonator. Fundamental uncertainty in analyte size (as deduced from the first and second moments of the analyte mass distribution), can be calculated from Eq. (6) using standard error propagation of the frequency fluctuations.

The uncertainty in particle size due to frequency noise is now derived for the doubly-clamped beam geometry. Assuming the mass,  $m^{(0)}$  and position,  $\mu$ , of a particle have been calculated and that errors in those values are much smaller than the uncertainty in size (as is usually the case), one can

set the superposition function  $g(x) = (x - \mu)^2$  to extract the coefficients,  $\alpha_n^{(2)}$ . Now, using Eq. (1) and (6), the standard deviation of the particle distribution can be calculated as:

$$\sigma = \left[ \frac{-2M}{m^{(0)}} \sum_{n=1}^N \alpha_n^{(2)} \Delta \omega_n \right]^{1/2} \quad (27)$$

Where, the coefficients,  $\alpha_n^{(2)}$ , are solved using:

$$\sum_{n=1}^N \alpha_n^{(2)} \Phi_n^2(x) = (x - \mu)^2 \quad (28)$$

Device	Dimensions ( $L \times w \times t$ )	Est. Allan Deviation	Min. Spatial Resolution (nm)
Silicon Microbeam (ref. 9)	200 x 33 x 7 ( $\mu\text{m}$ )	$1 \times 10^{-8}$	370
Silicon Nanobeam (ref. 6)	10 x 0.3 x 0.1 ( $\mu\text{m}$ )	$8 \times 10^{-8}$	15
Graphene Nanoribbon (ref. 17)	1760 x 200 x 0.14 (nm)	$1.3 \times 10^{-6}$	4.2
SW Carbon Nanotube (ref. 14)	150 x 1.7 x 1.7 (nm)	$2 \times 10^{-6}$	0.3

**Table 2| Imaging resolution for typical micro- and nanomechanical resonators.** The diameters of the smallest measurable analytes are tabulated for the cases of a silicon microbeam (reference 9), silicon nanobeam (reference. 6), graphene nanoribbon (reference. 17), and a single-wall carbon nanotube (reference. 14). Doubly-clamped beam geometry with actual device dimensions, and representative experimental values for resonator frequency instability are employed. Frequency fluctuations are characterized by the Allan deviation, which was either reported directly or deduced from the reported mass sensitivity. The attainable spatial resolution is calculated assuming a rigidly adsorbed hemispherical particle with  $2 \text{ g/cm}^3$  mass density, from measurements of the first four mechanical modes (assumed to have identical frequency stabilities).

Here, the mode shapes have all been normalized such that the mode effective mass is just the total device mass. Now, one can directly calculate the statistical uncertainty in the standard deviation of the particle distribution,  $\sigma$ , due to frequency noise characterized by the Allan Deviation,  $\eta_{a,n}$ :

$$\Gamma(\sigma) = \left[ \frac{4 \sum_{n=1}^N (\alpha_n^{(2)})^2 \eta_{a,n}^2}{(m^{(0)} / M)^2} \right]^{1/2} \quad (29)$$

$\Gamma(\sigma)$  is then the statistical uncertainty in the standard deviation of the particle distribution. Heavier particles, relative to the beam, more easily overcome frequency noise (though they are more susceptible to fitting error) as they register a larger impact compared to the frequency noise. As the particle size is reduced, frequency fluctuations will dominate over the fitting error. Thus, the ultimate resolution of a given system is fully determined by Eq. (29). This equation also shows that the use of additional modes is useful only if those modes do not induce too much additional frequency noise.

Table 2 provides examples of the anticipated frequency-noise-limited size resolution attainable with current micro- and nano- resonator technology. Four devices are evaluated, a silicon microbeam [9], a silicon nanobeam [6], a graphene nanoribbon [17], and a single-walled carbon nanotube [14]. As seen in Table 2, the smallest measurable particle scales with both the beam and magnitude of frequency fluctuation. As shown, today's smallest devices are capable of atomic-scale resolution.

## 5.7 Conclusion

Inertial imaging enables measurements of both the mass and shape of analytes that adsorb on a nanomechanical resonator. Analogous to the previous nanomechanical measurements of mass and position-of-adsorption of individual proteins [6], inertial imaging is possible in real time, one-by-one, as individual analytes adsorb on a NEMS sensor. The ultimate resolution of this technique is not

limited by the modal wavelengths, but instead only by the frequency instability of the nanomechanical resonators employed. NEMS-based inertial imaging can enable single-molecule mass spectrometry and, simultaneously, evaluation of molecular shapes with atomic-scale resolution.

## 5.8 Bibliography

1. Ekinci, K.L., X.M.H. Huang, and M.L. Roukes, *Ultrasensitive nanoelectromechanical mass detection*. Applied Physics Letters, 2004. **84**(22): p. 4469-4471.
2. Ilic, B., et al., *Attogram detection using nanoelectromechanical oscillators*. Journal of Applied Physics, 2004. **95**(7): p. 3694-3703.
3. Yang, Y.T., et al., *Zeptogram-Scale Nanomechanical Mass Sensing*. Nano Letters, 2006. **6**(4): p. 583-586.
4. Li, M., H.X. Tang, and M.L. Roukes, *Ultra-sensitive NEMS-based cantilevers for sensing, scanned probe and very high-frequency applications*. Nature Nanotechnology, 2007. **2**(2): p. 114-120.
5. Gil-Santos, E., et al., *Nanomechanical mass sensing and stiffness spectrometry based on two-dimensional vibrations of resonant nanowires*. Nature Nanotechnology, 2010. **5**(9): p. 641-5.
6. Hanay, M.S., et al., *Single-protein nanomechanical mass spectrometry in real time*. Nat Nano, 2012. **7**(9): p. 602-608.
7. Naik, A.K., et al., *Towards single-molecule nanomechanical mass spectrometry*. Nat Nano, 2009. **4**(7): p. 445-450.
8. Schmid, S., et al., *Real-time single airborne nanoparticle detection with nanomechanical resonant filter-fiber*. Sci Rep, 2013. **3**: p. 1288.
9. Burg, T.P., et al., *Weighing of biomolecules, single cells and single nanoparticles in fluid*. Nature, 2007. **446**(7139): p. 1066-1069.
10. Gupta, A., D. Akin, and R. Bashir, *Single virus particle mass detection using microresonators with nanoscale thickness*. Applied Physics Letters, 2004. **84**(11): p. 1976-1978.
11. Jensen, K., K. Kim, and A. Zettl, *An atomic-resolution nanomechanical mass sensor*. Nature Nanotechnology, 2008. **3**(9): p. 533-7.
12. Chiu, H.Y., et al., *Atomic-scale mass sensing using carbon nanotube resonators*. Nano Lett, 2008. **8**(12): p. 4342-6.
13. Lassagne, B., et al., *Ultrasensitive mass sensing with a nanotube electromechanical resonator*. Nano Lett, 2008. **8**(11): p. 3735-8.
14. Chaste, J., et al., *A nanomechanical mass sensor with yoctogram resolution*. Nature Nanotechnology, 2012. **7**(5): p. 300-303.
15. Landau, L.D., et al., *Theory of elasticity*. 3rd English ed. Course of theoretical physics. 1986, Oxford Oxfordshire ; New York: Pergamon Press. viii, 187 p.
16. Dohn, S., et al., *Enhanced functionality of cantilever based mass sensors using higher modes*. Applied Physics Letters, 2005. **86**(23).
17. Chen, C.Y., et al., *Performance of monolayer graphene nanomechanical resonators with electrical readout*. Nature Nanotechnology, 2009. **4**(12): p. 861-867.

## CONCLUDING REMARKS

This thesis has presented my work in the development of NEMS-MS for bio-molecules. Demonstrated is the construction and operation of a system designed to perform LD-NEMS-MS of single particles and proteins. It was found that UHV conditions ( $<10^{-8}$  Torr) are optimally suited for this type of system in order to minimize noise and background effects. Further, there exists a trade-off between sample surface mass density and sample-NEMS distance based on the plume density profile. Implementation of a backside desorption process is optimal to produce a high flux on the NEMS device, while minimizing bunching effects of the sample. Further, it was found that spectra of particle landing positions on the NEMS device can aid as a diagnostic tool in distinguishing single particle events from small-particle film deposition. It was ultimately discovered that MALDI is unsuitable for NEMS-MS due to the broad matrix background.

Though traditional MALDI is not a feasible delivery mechanism for proteins, gold nanoparticles can be individually measured in the LD-NEMS-MS system. These measurements are combined with measurements of individual IgM antibodies in an ESI-NEMS-MS system to demonstrate the potential of NEMS-MS systems for single-particle nanomechanical mass spectrometry in real-time. It is shown that particles are sequentially delivered to a NEMS device and introduce abrupt shifts in the resonance frequencies of the device upon adsorption. Through continuous frequency tracking of two displacement modes of a NEMS device, pairs of frequency shifts are used to calculate the mass and landing position of individual gold nanoparticles and IgM antibodies.

Single-protein mass spectrometry was finally performed in the LD-NEMS-MS system through the incorporation of LIAD as a protein delivery technique. To accommodate LIAD, the system was appropriately modified and a new substrate was engineered to optimize the LIAD process for NEMS-MS. The LIAD-NEMS-MS system was used to record the mass spectra of

various proteins species. The measured proteins included those that are polyforms of a single sub-unit and complex protein structures composed of multiple sub-units. These results demonstrate the ability of LIAD-NEMS-MS to perform single-protein mass spectrometry, but continued development of the sample preparation protocols and optimization of the system parameters is desired to improve the data. Further, there is evidence to suggest, but not yet conclude, that proteins are transported along the device surface due to the surface vibrations of the resonant modes of the device in a Chladni-style process.

Finally, the capabilities of NEMS for single particle measurements are extended beyond mass spectrometry to now inertial imaging of single particles. This new methodology shows that the spatial distribution of mass within an individual analyte can be imaged – in real-time and with molecular-scale resolution – upon its adsorption onto a multimodal nanomechanical resonator. By continuously monitoring multiple vibrational modes, the spatial moments of mass distribution can be deduced for individual analytes, one-by-one, as they adsorb. This information amounts to an image of the adsorbate itself, attained through the inertial effect on the device – inertial imaging. The ultimate resolution of this technique is not limited by the modal wavelengths, but instead only by the frequency instability of the nanomechanical resonators employed. This new technique is validated through a reanalysis of experimental data and FEM simulations. It is further demonstrated that using existing NEMS devices, particle imaging on the atomic scale is possible with this technique.

These results reveal that NEMS-MS is a promising technology for single-particle mass spectrometry and imaging. The experiments presented in this work can be continued in a number of promising directions in the future. One immediate task for future work, mentioned in chapter four, is to improve sample preparation and optimization of the protein delivery mechanism in LIAD-NEMS-MS. This will involve the development of protocols to maintain the original

configuration of the protein structures from when they are deposited from solution until they land on the device. A new NEMS-MS system is being developed in collaboration with our LETI collaborators that seeks to address the issue of maintaining protein structure. This new system utilizes a technique, surface acoustic wave nebulization (SAWN), that can inject proteins directly into vacuum from the liquid phase – as in ESI-NEMS-MS – but avoids charging the proteins or using ion optics – as does LIAD-NEMS-MS. An additional area of further development for protein delivery is to multiplex the protein plumes or particle beams such that multiple arrays can be simultaneously addressed from the same biological sample. This would significantly enhance system throughput while maintaining an optimal particle flux per device.

There are also a number of areas of continued research concerned with enhancing the technical capabilities of the NEMS devices. One of these is improving the mass resolution of the NEMS devices. Currently limited to 50 kDa for the devices employed in this work, the mass resolution can be improved by overcoming sources of frequency noise. As mentioned in chapter one, the measured frequency instability of our devices is much larger than what is expected from thermomechanical fluctuations alone. This suggests the presence of an additional noise source. Investigation of possible noise sources in NEMS devices is being continued by Caryn Bullard of the Roukes group. While initial investigations have concluded that this so-called “anomalous phase noise” is present in the device itself (not the connection lines or control electronics) the ultimate cause remains unknown. Cooling the devices from room temperature to liquid nitrogen temperature (77K), though intended to promote physisorption of analytes, does reduce frequency fluctuations. Further cooling the devices to milliKelvin temperatures may be a method to overcome these unknown sources of frequency instability.

Additionally, the mass resolution of the devices can also be improved through the implementation of new geometries and materials. Since the mass resolution is inversely

proportional to the device mass, smaller devices should allow for better resolution. Shrinking devices, however, can compromise capture cross-section. New device designs, such as thin membranes, for example, would enable a reduction in device mass without sacrificing capture area. Lighter materials such as graphene are also in the process of being implemented as device materials. Peter Hung of the Roukes group is leading the effort to manufacture graphene NEMS devices for mass spectrometry.

Averaging the signal across many devices is a technique to improve resolution in applications such as NEMS-based gas sensing, where the measurements are correlated between devices. In NEMS-MS, however, each device operates independently to measure separate particles; a signal average for resolution enhancement is thus not possible. Improving the mass resolution of NEMS devices while maintaining CMOS and VLSI compatibility is thus an ongoing engineering and fabrication challenge. It appears, however, that there is no fundamental process suggesting that single-Dalton resolution<sup>3</sup> is not attainable with devices similar in size to present designs.

Another area for continued research is the development of dense, interconnected arrays of NEMS devices. High-throughput NEMS-MS will require implementation of arrays of thousands of devices with filling factors more than an order of magnitude above that of our initial, modest arrays of 100 devices (<1%). One route to achieve this is the development of new devices that can maximize capture cross section while limiting device mass (thin membranes, for example). Additionally, the control electronics for thousands of individually addressed devices necessitates the development of on-chip CMOS electronics. To avoid occupying valuable real estate on the

---

<sup>3</sup> Single-Dalton (the mass of a hydrogen atom) resolution is considered a benchmark of what is achievable for NEMS-MS based on present nano-device physics. Some have argued that sub-Dalton resolution is possible using various quantum mechanical schemes of measurement, but we are not yet ready to begin consideration of such.

chip surface, there is an on-going project with our LETI collaborators to development three dimensional CMOS integration for NEMS arrays. In such a design, the CMOS electronics for device control are located beneath the top wafer layer in which the NEMS devices are fabricated. Three dimensional integration of CMOS electronics and NEMS arrays will thus allow thousands of devices to be individually addressed and measured without sacrificing surface area for particle detection.

Increasing the throughput of NEMS-MS system could also be accomplished by altering the particle transportation and deposition scheme. In current setups, particle detection is a hit or miss prospect. Of the particle plume sent to the NEMS chip only a small fraction is detected. The rest are “lost” as they absorb on the non-active surface area or miss the chip entirely. However, one could imagine a scheme where a sample is injected into a system in which the entire inner surface area is functionalized such that absorption is only possible on the active area of the NEMS chip and not elsewhere on the chip or the surrounding volume. In such a system particles will recirculate through the volume until they eventually absorb onto a device; a gas-phase analogue to microfluidic reflow systems. Such a scheme presents a large number of very daunting technical challenges including efficient gas-phase surface functionalization, and miniaturization of vacuum systems. However, the development of such a technique would produce a NEMS-MS system in which the minimum detectable concentration of a particle (such as pathogen, biomarker, or chemical agent) is simply a function of delay time. This development would circumvent limitations on overall system throughput currently imposed by the filling factor of NEMS arrays.

Finally, given the inertial imaging methodology presented in chapter five, new experiments can be done that incorporate mass and shape information for particle analysis. These can include experiments for understanding the structure and assembly of protein complexes using a single measurement device. Presently, investigations of protein structure using mass spectrometry are

accomplished using a tandem combination of ion mobility spectrometry (to extract size and shape from collision cross-section) and conventional  $m/z$  measurement. Additionally, the measurement of mass and shape can also be used as a method of multi-dimension analysis for identification of particles that may have similar masses but different density profiles.

NEMS-based systems for particle sensing is a promising technology for mass spectrometry and biology. Similar to the development of other technologies, many of the application may not yet be imagined. NEMS sensing has shown promising results and looks to be fertile ground for continued scientific exploration and development.

## APPENDIX

*Derivation of moments of arbitrary mass distribution for one-dimensional doubly-clamped beam.*

Not only we can calculate the total mass of an arbitrary mass distribution on the beam, we can calculate any arbitrary moments of the distribution. In this section we will focus on calculating the first three moments. These can be used to give the mean, size, and skew factor from standard statistics. In the following analysis, we again consider a doubly clamped beam. From the initial mass distribution,  $\Delta\rho(x)$ , with total mass,  $M_a$ , we now introduce the normalized distribution,  $v(x)$ , such that:

$$v(x) = \frac{\Delta\rho(x)}{M_a} \quad (30)$$

Then the “position” of the particle is now properly defined as the mean of the normalized distribution,  $\bar{X}$  :

$$\bar{X} = \int_{\Omega} xv(x) dx \quad (31)$$

Analogous to the method of solving for the mass, we now set the fitting function,  $g(\mathbf{r}) = g(x) = x$  and find a set of coefficients,  $\beta_n$ , such that :

$$g(x) = x = \sum_{n=1}^N \beta_n \Phi_n^2(x), \text{ for } x \in [\text{meas. zone}] \quad (32)$$

However, for a doubly clamped beam, because the mode displacements are all symmetric functions about  $x=L/2$ , the superposition poorly fits the criterion for  $x>L/2$ . We can prove that restricting the measurement zone to the first half of the beam doesn't result in loss of generality, so long as the particle's position is interpreted as respect to the beam center. We introduce a set of functions:

$$f_n(x) = \begin{cases} x^n, & x_{min} < x \leq 1/2 \\ (1-x)^n, & 1/2 < x \leq x_{max} \end{cases}$$

Now we replace Eq. (32) with:

$$\sum_{n=1}^N \beta_n \Phi_n^2(x) = f_1(x) \quad (33)$$

We can now solve directly for  $\bar{X}$  (with  $x_{min}=0, x_{max}=1$ , to cover the whole beam):

$$\begin{aligned} \bar{X} &= \int_0^1 x \rho(x) dx = \int_0^{1/2} x \nu(x) dx + \int_{1/2}^1 x \nu(x) dx = \int_0^{1/2} f_1(x) \nu(x) dx + \int_{1/2}^1 (1-f_1(x)) \nu(x) dx \\ &\quad \cdot \\ &\quad \cdot \\ &\quad \cdot \\ &= \int_0^{1/2} f_1(x) \nu(x) dx + \int_0^1 \nu(x) dx - 2 \int_{1/2}^1 f_1(x) \nu(x) dx - \int_0^{1/2} \nu(x) dx \end{aligned}$$

Assuming the particle is small relative to the beam length, there are two cases to consider:

1)  $\nu(x) = 0$ , for  $x > 1/2$ , then :

$$\begin{aligned} \bar{X} &= \int_0^{1/2} f_1(x) \nu(x) dx + \int_0^1 \nu(x) dx - 2 \int_{1/2}^1 f_1(x) \nu(x) dx - \int_0^{1/2} \nu(x) dx \\ &= \int_0^{1/2} f_1(x) \nu(x) dx + \int_{1/2}^1 f_1(x) \nu(x) dx + \int_0^{1/2} \nu(x) dx - \int_{1/2}^1 \nu(x) dx - \int_0^{1/2} \nu(x) dx \\ &= \int_0^{1/2} f_1(x) \nu(x) dx = \sum_{n=1}^N \beta_n \Delta \bar{\omega}_n \end{aligned}$$

2)  $\rho(x) = 0$  for  $x < 1/2$ : Eq. 6 immediately reduces to:

$$\bar{X} = \int_{1/2}^1 (1-f_1(x)) \nu(x) dx = \sum_{n=1}^N \beta_n \Delta \bar{\omega}_n$$

Thus, restricting the measurement zone to one half of the beam, simply restricts the position measurement to a distance from the center. Since the higher order moments are normalized to the mean position, they are unaffected. We can now proceed in a similar fashion as Eq. (32) to calculate the standard deviation,  $\sigma$ , and the skew,  $\eta$ . Without loss of generality, we now assume the particle is wholly located in the range  $[0, 1/2]$  of the beam. We further note that devices with non-symmetric geometries (such as cantilevers) are able to recover particles of any size less than the beam itself.

We introduce a third and fourth set of coefficients,  $\gamma_n, \zeta_n$ , such that:

$$\sum_{n=1}^M \gamma_n \Phi_n^2(x) = f_2(x)$$

$$\sum_{n=1}^M \zeta_n \Phi_n^2(x) = f_3(x)$$

Then:

$$\begin{aligned} \sigma^2 &= \int_0^{1/2} (x - \bar{X})^2 \nu(x) dx = \int_0^{1/2} (x - \bar{X})^2 \nu(x) dx = \int_0^{1/2} f_2(x) \nu(x) dx - \left[ \int_0^{1/2} f_2(x) \nu(x) dx \right]^2 \\ &= \sum_{n=1}^N \gamma_n \Delta \bar{\omega}_n - \left[ \sum_{n=1}^N \beta_n \Delta \bar{\omega}_n \right]^2 \end{aligned} \quad (34)$$

and:

$$\begin{aligned} \eta &= \int_0^{1/2} \left( \frac{x - \bar{X}}{\sigma} \right)^3 \nu(x) dx = \int_0^{1/2} \left( \frac{x - \bar{X}}{\sigma} \right)^3 \nu(x) dx \\ &= \frac{\sum_{n=1}^N \zeta_n \Delta \bar{\omega}_n - 3 \left[ \sum_{n=1}^N \beta_n \Delta \bar{\omega}_n \right] \left[ \sum_{n=1}^N \gamma_n \Delta \bar{\omega}_n \right] + 2 \left[ \sum_{n=1}^N \beta_n \Delta \bar{\omega}_n \right]^3}{\left[ \sum_{n=1}^N \gamma_n \Delta \bar{\omega}_n - \left[ \sum_{n=1}^N \beta_n \Delta \bar{\omega}_n \right]^2 \right]^{3/2}} \end{aligned} \quad (35)$$

The superpositions of the mode shapes using the first four out-of-plane modes of a doubly clamped beam that are used to calculate the first three moments of the particle distribution are shown in Figure 42.